Poznań University of Technology
Faculty of Civil and Transport Engineering

Doctoral dissertation

Michał Szymczyk

Fractional viscoplasticity for metallic materials under dynamic loading

Supervisor: Wojciech Sumelka, Ph.D., D.Sc.
Co-Supervisor: Marcin Nowak, Ph.D.

Reviewers
prof. dr hab. inż. Jacek LESZCZYŃSKI
dr hab. inż. Jerzy BOBIŃSKI, prof. PG

Cover design
prof. Tadeusz PISKORSKI

Typesetting
Michał SZYMCZYK

Proofreading
Donata GUMINIAK

ISBN 978-83-7775-625-6 (printed version)

ISBN 978-83-7775-626-3 (digital version)
https://doi.org/10.21008/b.978-83-7775-626-3

Edition I

Publishing House of Poznan University of Technology
Piotrowo 5, 60-965 Poznań
tel. +48 61 665 35 16
e-mail: office_ed@put.poznan.pl
www.wydawnictwo.put.poznan.pl

Binding and duplication in
Perfekt – Gaul i wspólnicy sp. j.
ul. Skórzewska 63
60-185 Skórzewo
tel. +48 61 666 05 19

Contents

Acknowledgements

Firstly, I would like to express my sincere gratitude to my advisor Prof. Wojciech Sumelka for the continuous support of my Ph.D. study and related research, for his patience, motivation, and immense knowledge. His guidance helped me in all the time of research and writing of this thesis. I could not have imagined having a better advisor and mentor for my Ph.D. study.

Besides my advisor, I would like to thank my co-advisor, Dr Marcin Nowak, for his insightful comments and encouragement, but also for the hard question which incented me to widen my research from various perspectives.

I thank my colleagues from the Division of Computer-Aided Design: Dr Tomasz Gajewski, Dr Krzysztof Szajek, Dr Hasan Al-Rifaie, Dr Tomasz Garbowski, Dr Tomasz Jankowiak, Dr Piotr Sielicki and Bartosz Łuczak, for the stimulating discussions and their indulgence when I was asking questions that challenged their patience rather than knowledge.

I would like to thank Prof. Tomasz Łodygowski for his support and his interest in my research.

During my Ph.D. studies, I was fortunate enough to attend excellent university courses. I would like to thank Prof. Katarzyna Kowalczyk-Gajewska, Prof. Mieczysław Kuczma and Prof. Wojciech Sumelka for the lectures that broaden my knowledge and gave me tools to tackle research problems.

I would also like to express my gratitude towards my colleagues and superiors, Rafał Sadowski and Robert Jędrzejczak, for their support and understanding.

I am indebted to the communities behind the multiple open-source software projects, which were instrumental in my work, such as GNU\Linux, GIMP, Inkscape, Blender, Python, LaTeX, Scilab. I would also like to acknowledge commercial tools that were available to me under research or academic licenses: Abaqus, Intel Fortran Compiler, PyCharm, GitHub. This thesis was created using Overleaf, a cloud-based LaTeX editor.

I would like to thank my family: my parents and my brother for supporting me spiritually throughout writing this thesis and my life in general. Also, I would like to express my gratitude to my parents-in-law for helping us to get through this difficult time.

Last but not the least, I would like to thank my wife, Ewelina. She is my whole world and without her patience, love and kindness, I could not achieve any of the meaningful things I have done in my life. Her beautiful soul helps me to keep my demons at bay. I would also like to thank my sons, Stefan and Jan, for the joy they bring into my life.

The support of the National Science Centre under the grant 2017/27/B/ST8/00351 is kindly acknowledged.

Abstract

Rate-dependent material models are used in civil engineering when a dynamic response of structure has to be examined. These models, used in conjunction with, e.g. software suites for finite element analysis, provide a powerful tool for solving dynamic problems. An effective approach should include material properties such as anisotropy, non-locality and non-normality of the inelastic flow. The goal of this treatise is to develop a comprehensive mathematical model that could be successfully applied for special cases when high-strain-rate deformations in metals, are considered.

The Perzyna viscoplastic model in its extended constitutive form, which accounts for strain-rate hardening, microdamage mechanism, thermo-mechanical coupling and the fracture criterion, was chosen for this research. Fractional derivatives were used for the aforementioned model to introduce the non-local and anisotropic properties. The numerical analyses were conducted at the material point level to evaluate the impact that the fractional parameters have on the dynamic material response. Next, the dynamic tests were carried out for a full three-dimensional dog-bone specimen for various parameters and loading velocities. In this last case, the strain localization was observed and studied. Moreover, the evolution of the state variables in the Perzyna formulation was closely examined.

Results of the numerical analysis have shown that the fractional viscoplastic model exhibits non-locality, as well as, the anisotropy in the level and direction of deformation. Moreover, the directional behaviour was also found in the dissipation of mechanical wave energy. The anisotropy was also observed in the strain localization and deformation modes of the dog-bone specimen. The non-locality and directional dependence had an impact on the evolution of the state variables of the Perzyna model. In conclusion, the results reflect the one obtained in the available experimental studies.

Based on the above, the thesis of this dissertation, which stated that *the fractional formulation of the viscoplastic model improves the description of metals behavior under dynamic loading*, can be assumed to be valid.

Streszczenie

Modele konstytutywne uwzględniające wpływ prędkości deformacji są stosowane w inżynierii lądowej w zagadnieniach analizy dynamicznego zachowania konstrukcji. Ich zastosowanie w programach wykorzystujących np. metodę elementów skończonych dostarcza zaawansowanych narzędzi analizy. Ponadto prawa konstytutywne winny, dla ww. klasy zagadnień, uwzględniać anizotropię materiału, efekty nielokalne oraz niestowarzyszone prawo płynięcia plastycznego. Celem niniejszej pracy jest opracowanie modelu obejmującego wspomniane cechy, w szczególności dla materiałów metalicznych.

Do badań wybrano lepkoplastyczny model Perzyny, który uwzględnia umocnienie zależne od prędkości deformacji oraz mechanizm mikrouszkodzenia z wpływem efektów termicznych (proces adiabatyczny). Zastosowano w nim uogólnienie oparte na pochodnych niecałkowitego rzędu w celu rozbudowania go o właściwości nielokalne oraz anizotropowe. Przeprowadzono analizy numeryczne na poziomie punktu materialnego oraz symulacje testu dynamicznego rozciągania dla trójwymiarowej próbki przy różnych parametrach modelu oraz różnych prędkościach wymuszenia. W ostatnim przypadku dużo uwagi poświęcono badaniom procesu lokalizacji odkształceń. Ponadto dokładnie zbadano ewolucję parametrów wewnętrznych zaproponowanego prawa konstytutywnego.

Wyniki analiz numerycznych potwierdziły, że model lepkoplastyczny wykorzystujący pochodne ułamkowe wykazuje efekty nielokalne, a także anizotropię w intensywności i kierunku deformacji. Zaobserwowano także kierunkową naturę w rozpraszaniu energii fal mechanicznych. Anizotropia została także zauważona w lokalizacji odkształceń plastycznych oraz kształtach, jakie przyjmowała strefa deformacji. Efekty nielokalne i zależne od kierunku zauważono także w ewolucji parametrów wewnętrznych rozważanego prawa konstytutywnego. W konkluzji wyniki odzwierciedlają rezultaty uzyskane w dostępnych w literaturze badaniach eksperymentalnych.

Na podstawie uzyskanych rezultatów można przyjąć, że teza tej rozprawy, w której stwierdzono, iż *sformułowanie modelu lepkoplastycznego wykorzystującego pochodne ułamkowe poprawia opis zachowania metali obciążonych dynamicznie*, jest prawidłowa.

List of symbols and abbreviations

The following notation is used in this dissertation:

- normal-face Greek or Latin letters for scalars,
- bold-face Greek or Latin letters for vectors and second ordered tensors,
- uppercase letters for Lagrangian and lowercase letters for Eulerian variables.

Symbol/Abbreviation	Description	First use
a	left bounds of the proper integral	page 36
$\boldsymbol{a}$	vector form of the left bound of the proper integral	page 42
$\mathbf{a}$	acceleration	page 22
b	right bound of the proper integral	page 36
$\boldsymbol{b}$	vector form of the right bound of the proper integral	page 43
$\tilde{\boldsymbol{b}}$	vector of body forces	page 22
$\mathbf{B}$	shape function derivative matrix	page 31
$\mathcal{B}$	physical body	page 14
$\partial\mathcal{B}$	boundary surface of the body $\mathcal{B}$	page 21
B_P^α	general kernel differential operator of Caputo type	page 36
c_d	dilatational wave speed	page 34
c_p	specific heat	page 61
$\hat{c}$	elastic wave propagation velocity	page 40
$\boldsymbol{c}$	left Cauchy-Green tensors	page 17
$\boldsymbol{C}$	right Cauchy-Green tensors	page 17
$\boldsymbol{d}$	symmetric part of the spatial velocity gradient	page 19
$d\mathbf{a}$	infinitesimal area element in the current configuration	page 17
$d\boldsymbol{f}$	density of forces acting on an infinitesimal surface	page 19
$d\mathrm{v}$	infinitesimal volume element in the current configuration	page 17

Symbol/Abbreviation	Description	First use
$d\boldsymbol{x}$	infinitesimal line element in the current configuration	page 16
$d\mathbf{A}$	infinitesimal area element in the reference configuration	page 17
$d\mathrm{V}$	infinitesimal volume element in the reference configuration	page 17
$d\boldsymbol{X}$	infinitesimal line element in the reference configuration	page 16
D^{α}	Riesz-Caputo fractional derivative of the α order	page 37
${}_{a}^{C}D_{t}^{\alpha}$	left-sided Caputo derivative	page 36
${}_{t}^{C}D_{b}^{\alpha}$	right-sided Caputo derivative	page 37
$\boldsymbol{e}$	Almansi strain tensors	page 17
e_c	thermodynamic state variable	page 24
$\hat{\boldsymbol{e}}_i$	Eulerian base	page 14
E	Young's modulus	page 42
$\boldsymbol{E}$	Green strain tensors	page 17
$\hat{\boldsymbol{E}}_i$	Lagrangian base	page 14
$\mathcal{E}$	internal energy	page 24
$\mathcal{E}^3$	three-dimensional Euclidean point space	page 14
f	yield function	page 38
$f^{(n)}$	classical n-th order derivative	page 38
$\hat{\mathbf{f}}$	specific load matrix	page 32
F	static yield condition	page 38
$\boldsymbol{F}$	deformation gradient	page 16
$\boldsymbol{F}^{-1}$	inverse deformation gradient	page 16
$\dot{\boldsymbol{F}}$	time derivative of the deformation gradient	page 19
F	force vector	page 22
g^*	void growth material function	page 60
G	Lamé's second parameter, shear modulus	page 42
G^{eq}	direct Galerkin expression	page 29
$\hat{G}^{eq}$	finite approximation of direct Galerkin expression	page 30
$\hat{G}_e$	part of Galerkin expression for element of domain Ω	page 30
$\hat{G}_{t_e}$	part of Galerkin expression for element of the boundary segment $\partial\Omega_t$	page 30
$\mathcal{G}$	total production of entropy	page 26
$\boldsymbol{h}$	entropy flux vector field	page 26
h_a	width of the subinterval in the left-sided Caputo derivative	page 37
h_b	width of the subinterval in the right-sided Caputo derivative	page 38
$\boldsymbol{h}^a$	vector form of the subinterval width in the left-sided Caputo derivative	page 43

Symbol/Abbreviation	Description	First use
$\boldsymbol{h}^b$	vector form of the subinterval width in the right-sided Caputo derivative	page 43
${}_aI_t^\alpha$	left Riemann-Liouville fractional integral	page 36
${}_tI_b^\alpha$	right Riemann-Liouville fractional integral	page 36
I_g	stress intensity invariant	page 60
I_2^P	second invariant of an inelastic strain-rate tensor	page 39
J	Jacobian determinant, determinant of $\boldsymbol{F}$	page 16
J_1	first invariant of the stress tensor	page 60
J_2'	second invariant of the stress deviator	page 39
$\dot{J}$	time derivative of the Jacobian determinant	page 19
J	angular momentum vector	page 23
$\dot{\mathsf{J}}$	time derivative of angular momentum	page 23
k_α	kernel function	page 35
K_P^α	K-operator	page 35
$\mathcal{K}$	kinetic energy	page 24
l	length-scale parameter	page 40
$\boldsymbol{l}$	spatial velocity gradient	page 18
$L_{e,min}$	smallest element dimension in the mesh	page 34
$\dot{\mathsf{L}}$	time derivative of a linear momentum	page 22
$\mathcal{L}^e$	stiffness matrix	page 38
m	total mass of a body $\mathcal{B}$	page 21
m	scalar rate-sensitivity parameter	page 40
m_a	number of subintervals in the left-sided Caputo derivative	page 37
m_b	number of subintervals in the right-sided Caputo derivative	page 38
$\dot{m}$	time derivative of mass	page 21
$\boldsymbol{M}$	matrix of the classical first-order partial derivatives	page 45
M	momentum vector	page 23
$\hat{\mathbf{M}}$	mass matrix	page 32
$\boldsymbol{n}$	normal vector perpendicular to $d\mathbf{a}$ surface in the current configuration	page 17
n_p	number of points in the numerical approximation	page 43
$\mathbf{N}$	element shape function	page 31
$\boldsymbol{N}$	normal vector perpendicular to $d\mathbf{A}$ surface in the reference configuration	page 17
p, q	real numbers	page 35
$\boldsymbol{p}$	direction of viscoplastic flow	page 40
p	momentum vector	page 22
$\dot{\mathsf{p}}$	time derivative of momentum	page 22
P	particle of a body $\mathcal{B}$	page 14
$\boldsymbol{P}$	matrix of coefficients for numerical approximations of fractional derivatives	page 44

Symbol/Abbreviation	Description	First use
$\boldsymbol{P}_{PK}$	first Piola-Kirchoff stress tensor	page 20
$\hat{\mathbf{P}}$	stress divergence	page 32
$\mathcal{P}_{int}$	stress power	page 24
$\mathcal{P}_{ext}$	external mechanical power	page 23
$\mathbf{q}$	Cauchy heat flux	page 25
$\mathcal{Q}$	thermal power	page 25
$\tilde{\mathcal{Q}}$	entropy input rate	page 26
q_n	scalar heat flux	page 25
r	internal heat source	page 25
$\tilde{r}$	entropy sources scalar field	page 26
$\mathbf{r}$	position vector	page 23
$\mathbf{R}$	rotation tensor	page 17
$\boldsymbol{s}$	Cauchy stress deviator	page 39
$\boldsymbol{S}_{PK}$	second Piola-Kirchoff stress tensor	page 20
$\mathcal{S}$	total entropy function	page 25
t	time dimension	page 14
$\tilde{\boldsymbol{t}}$	Cauchy (true) traction vector	page 19
T_m	relaxation time	page 40
$\tilde{\boldsymbol{T}}$	first Piola-Kirchoff vector	page 19
$\boldsymbol{u}$	displacement field in the Eulerian description	page 16
$\ddot{\boldsymbol{u}}$	spatial acceleration field in terms of displacement	page 28
$\bar{\boldsymbol{u}}$	nodal displacement	page 31
$\hat{\boldsymbol{u}}$	finite approximation of the displacement field	page 31
$\delta\bar{\boldsymbol{u}}$	virtual nodal displacement	page 31
$\delta\boldsymbol{u}$	virtual displacement field (small strain theory)	page 28
$\delta\hat{\boldsymbol{u}}$	finite approximation of the virtual displacement field	page 31
$\boldsymbol{U}$	displacement field in the Lagrangian description	page 15
$\mathbf{U}$	right stretch tensors	page 17
$\boldsymbol{v}$	spatial velocity field	page 18
$\dot{\boldsymbol{v}}$	spatial acceleration field	page 22
$\boldsymbol{V}$	material velocity field	page 18
$\mathbf{V}$	left stretch tensors	page 17
$\boldsymbol{w}$	skew-symmetric part of the spatial velocity gradient	page 19
$\boldsymbol{x}$	position vector of a particle in the current configuration	page 14
x_i	spatial coordinates of a point P	page 14
$\boldsymbol{X}$	position vector of a particle in the reference configuration	page 14
X_i	material coordinates of a point P	page 14
$\boldsymbol{Z}$	stress-states in the material point neighbourhood	page 45
α	order of the fractional derivative	page 35

Symbol/Abbreviation	Description	First use
$\hat{\alpha}$	proportionality factor	page 40
γ	viscosity-related parameter	page 39
γ_0	material constant	page 39
Γ	Gamma function	page 36
δ	fracture porosity	page 60
Δt	time increment in the Abaqus\Explicit analysis	page 46
$\boldsymbol{\Delta}^L$	left-sided stress-fractional spread	page 42
$\boldsymbol{\Delta}^R$	right-sided stress-fractional spread	page 42
$\boldsymbol{\varepsilon}$	infinitesimal (small) strain tensor	page 18
$\boldsymbol{\varepsilon}^e$	elastic part of the small strain tensor	page 38
$\boldsymbol{\varepsilon}^p$	inelastic part of the small strain tensor	page 38
$\boldsymbol{\varepsilon}^{tr}$	elastic (trail) small strain tensor	page 29
$\boldsymbol{\varepsilon}^{vp}$	viscoplastic part of the small strain tensor	page 38
$\dot{\boldsymbol{\varepsilon}}$	strain-rate tensor	page 38
$\dot{\boldsymbol{\varepsilon}}^e$	elastic part of strain-rate tensor	page 38
$\dot{\boldsymbol{\varepsilon}}^{vp}$	viscoplastic part of strain-rate tensor	page 38
ζ_0	one-to-one mapping between particle P and point $\boldsymbol{X}$	page 14
ζ	one-to-one mapping between particle P and point $\boldsymbol{x}$	page 14
η_c	specific entropy	page 25
θ	absolute temperature	page 26
ϑ	temperature in kelvins (K)	page 59
ϑ_0	reference temperature	page 61
κ	static yield stress in simple shear	page 38
κ_s	saturation stress	page 61
κ_0	initial yield stress in simple shear	page 60
λ	Lamé's first parameter	page 42
Λ	viscoplastic scalar multiplier	page 40
$\boldsymbol{\mu}$	vector of internal state variables	page 59
ν	Poisson's ratio	page 42
ξ	volume fraction porosity	page 59
ξ_F	critical value of volume fraction porosity	page 61
ξ_0	initial volume porosity	page 60
ρ	current density	page 21
ρ_0	referential density	page 21
$\dot{\rho}$	time derivative of density	page 21
$\boldsymbol{\sigma}$	Cauchy stress tensor	page 20
τ_{eq}	stress threshold	page 60
$\boldsymbol{\tau}$	Kirchoff stress tensor	page 21
ϕ	motion of body $\mathcal{B}$	page 14
$\dot{\phi}$	time derivative of the motion function	page 19
Φ	overstress function, material function	page 39

Symbol/Abbreviation	Description	First use
χ^*, χ^{**}	irreversibility coefficients	page 61
ω^h_{max}	highest frequency of the system	page 33
Ω	arbitrary configuration of a body $\mathcal{B}$	page 28
Ω_0	reference (undeformed) configuration of a body $\mathcal{B}$	page 14
Ω_c	current (deformed) configuration of a body $\mathcal{B}$	page 14
Ω_e	subdomains (elements) of Ω	page 14
$\partial\Omega$	surface of the body in the arbitrary configuration	page 29
$\partial\Omega_c$	surface of the body in the current configuration	page 22
$\partial\Omega_{t_e}$	element of boundary $\partial\Omega_t$	page 14
$\partial\Omega_{u_e}$	element of boundary $\partial\Omega_u$	page 14
$\partial\Omega_t$	part of the boundary $\partial\Omega$ where traction was specified	page 29
$\partial\Omega_u$	part of the boundary $\partial\Omega$ where displacements were specified	page 29
$\hat{\Omega}$	approximation of body in configuration Ω	page 30
$\mathbb{1}$	identity matrix	page 17
$\mathbb{B}$	matrix strain operator	page 29
$\in^{vp}$	equivalent viscoplastic deformation	page 59
$\dot{(\cdot)}$	first derivative with respect to time	page 18
$\ddot{(\cdot)}$	second derivative with respect to time	page 28
$(.)_{,j}$	partial derivative with respect to x_i	page 28

Chapter 1

Introduction

1.1. Motivation

During the last decades, the development of new materials does not seem to slow down. It is accompanied by the rise of new design techniques and engineering tools, such as simulation software packages that utilize the finite element method (FEM). This type of software is used in the numerical analysis of both elastic and inelastic response of materials, but it relies heavily on mathematical models that govern their behavior. Reliable material models in conjunction with damage mechanics became an industry standard for assessing the safety of new and existing structures. With the increase in the availability of computers, their portability and computing power, programs using FEM have become a useful tool in civil engineering.

The vast majority of problems in civil engineering revolve around static loading cases. There are, however, some situations where a dynamic response of a whole structure, or its parts, is of particular interest. Two types of use cases for dynamic models can be distinguished. The first case concerns buildings or miscellaneous engineering structures that have a high probability of being exposed to explosion or blast. The other instance concerns the numerical analysis of structures where some subset of their elements had lost the load-bearing capacity due to a dynamic failure – cf. Figs. 1.1 and 1.2. Numerical analyses of both design scenarios require rate-dependent models to reliably predict the dynamic response.

Comprehensive models also have to address the problems of anisotropy and nonlocal properties. The reason that these properties are important is that they occur in most of the materials traditionally used in civil engineering. Also, they can be found in new materials that are being adopted in modern engineering. The development of a formulation that would combine these two complex effects could increase the safety of constructions at the same time lowering the price of the designing process. From

Figure 1.1. Effects of the 2011 Tohoku Japan Earthquake. Fracture of top gusset plate in the 2-story parking garage [165]

the practical point of view, the model should promote simplicity by restraining the number of additional parameters, and simultaneously ensuring that previously obtained parameters would not require determination in an afresh study.

The development of an effective numerical model that can combine complex material properties, dynamic response and rapid growth of computational power is a key step towards tackling the more complicated problems in civil engineering. The reason for an extensive literature outlook, given in the subsequent section, is twofold. It helps to answer the question if such a model already was proposed, and if not, it serves as a foundation for further discussion.

1.2. State of the art

1.2.1. Introduction

In the previous section, the reasons behind this study were presented. This part offers an in-depth overview of research conducted in the fields that are relevant in a search of new numerical models. Metals undergoing dynamic inelastic deformation are of particular interest in this dissertation. As it was mentioned before, anisotropy and non-locality are common properties that exist in natural and man-made materials. The heterogeneity, that stems from these properties, is important in reproducing material behaviour as it contributes to the nucleation and evolution of the shear bands. The quantitative reproduction of strain localization is difficult, especially for dynamic loading, because it requires a model suitable for adiabatic plastic deformation in rate-sensitive materials. Perzyna's theory of viscoplasticity is a well-established approach

Figure 1.2. Structural failure after car crash into column in Placentia, California [142]

for such problems, however, it still could benefit from including non-normality and anisotropy in its scope. The non-local nature of the fractional calculus may offer a solution to these limitations as its usefulness was presented in various applications. The above topics are extensively reviewed in the subsequent sections.

1.2.2. Anisotropy and non-locality

Non-associated flow implies that the inelastic strain tensor is not normal to the yield surface [133]. Depending on the material, this rule will have different physical interpretations. In geomaterials, non-normality is associated with dilatancy that occurs in the soil searing process. In metals, it stems from nucleation of dislocations [30, 161, 222], nucleation and growth of voids under plastic deformation or grains breakup into disoriented, blocky subgrains [82, 100, 181]. The non-homogeneous structures that result from these micromechanical phenomena create or intensify anisotropy in the material. In certain cases, anisotropy can be induced by plastic deformation and develop in metals and geomaterials [6, 34, 56, 89, 118].

Non-associated flow rule is a prerequisite for building reliable material models for materials such as concrete [80, 86, 161], ceramics [21, 162, 163], composites [101] and metals [10, 75, 124, 202]. The separate group that exhibits the non-associated flow are geomaterials, i.e. rocks [110, 114, 212], granular materials [44, 199, 203, 213], clays [89, 107, 214] and reinforced soils [126]. Correct modelling of materials with intrinsic instabilities is important from the engineering point of view and approach that includes it should be preferred. However, this class of mathematical theories has its challenges, such as ill-posedness of the initial and boundary value problems in non-associative

plasticity [30, 211], strain localization [13], return mapping algorithm for non-associated plasticity [22], stress-strain integration problem [31, 146] or the use of non-associated models with quadratic or non-quadratic yield criteria [28, 58, 172, 173, 202]. It should be mentioned that the problems listed above do not concern only constitutive relations with the non-associated flow rule.

Non-locality is a concept observed in heterogeneous materials that pose a challenge when it comes to reliable material modelling. The early ideas for non-local formulations were developed in the 1960s and since then were studied by various authors [3, 12, 29, 35, 48, 54, 123, 127, 206]. Most of these theories establish a parameter that refers to the intrinsic structure of the material by introducing characteristic length or time. It can be obtained experimentally or estimated based on micromechanics [26, 59, 87, 99, 106, 219]. The issue of non-locality was studied in a different formulation, such as non-local theories [49, 178], strain-gradient theories [128, 206], micropolar theories [47, 137], or the theories of material surfaces [71].

The phenomena of anisotropic non-locality in various materials were closely studied. In [182] a general model for predicting crack nucleation and growth was proposed. Strain gradients were used in [97] to account for non-local structure in quasi-brittle materials. A rate-dependent non-local damage model was proposed and validated against experimental results obtained with the Split Hopkinson Bar by Pereira et al. [147]. In [20] a dynamic study of local and non-local formulations in brittle solids was conducted. A non-local theory was used as a regularization technique in [15] as a method for obtaining a mesh-independent solution. A comprehensive overview of the process of quasi-static fracture in plain and reinforced concrete with constitutive models that applied non-local or second-gradient theory was given in [204].

Germain et al. [60], through writing constitutive equations in a non-local framework, achieved implicit gradient formulation to model laminated structures. In [4] modelling of vascular tissues was studied by applying a fully three-dimensional anisotropic model of hyperelastic behaviour. Abu Al-Rub and Voyiadjis [1] presented a non-local gradient-enhanced fully coupled plastic-damage constitutive model of concrete. The rate-sensitive inelastic model with an embedded implicit length-scale parameter was profusely discussed in [155] and used in numerical analyses [66, 194].

The non-local and anisotropic properties of the material may impact the localization of strain. In the next section, the nucleation and the development of the narrow zones of shearing, so-called shear bands, are discussed.

1.2.3. Shear bands

The overview presented here covers a small portion of selected works that are relevant to the subject of this treatise. The first observation of adiabatic shear bands can be attributed to Tresca in [207], where he observed the thermal line, or heat cross, that occurred in the forging process. It was noted by the author that material strength, low thermal conductivity and low heat capacity are contributing factors to

this phenomenon. Observations of the metals forging process yielded many papers which were listed in [91]. However, early observations of shear bands are attributed to Zener and Hollomon [221], who were first to postulate that shear bands are the result of a local material instability powered by thermal softening. The temperature increase is caused by inelastic work and is a signature of change in the deformation conditions from isothermal to adiabatic. The localization of adiabatic shear bands was observed experimentally in various applications such as metal forging and milling, high-velocity punching and ballistic impact. Useful reviews of the subject were given by Rogers [166, 167, 168], Rogers and Shastry [169], Dormeval [37] and Zurek and Meyers [225]. Experimental measurements of the strain, strain rate and temperature at the onset of bands formation were studied by Moss [132], Olson et al. [141], Hartley et al. [72] and Marchand and Duffy [119]. The major effort of blending experimental results with mechanics was made by Erlich, Seaman and Shockey [50] by postulating nucleation and growth mechanism for shear bands. The localization of plastic shearing in the single crystal was studied by Chang and Asaro [19].

An in-depth study of the shear bands localization leads to the rise of two major mechanisms that are used to study this problem. First is associated with quasi-static, isothermal deformations in materials that do not exhibit rate-sensitivity, therefore is out of the scope of this dissertation and will only be mentioned here. An interested reader is referred to references [5, 24, 25, 76, 84, 85, 145, 164, 170, 205].

The second mechanism regards the adiabatic deformation in rate-sensitive materials. In [217] authors assumed material characterized by strain hardening, thermal softening, strain-rate hardening and were able to show that thickness of the shear band depends on the rate-dependent component in the governing equations. Deformation of a large block of material, with small regions of embedded imperfections, subjected to a constant average strain rate was studied by Wu et al. [218]. It was found that the shear bands initiate in the region of the material defect. Pan et al. [144] conducted a study on the effect of the strain-rate sensitivity on the localization of deformation in viscoplastic solids. Two loading conditions, plane strain tension and axisymmetric tension were considered in the numerical inquiries that showed the relation between the material rate-sensitivity and the void nucleation and growth. LeMonds and Needleman [102] built upon the numerical framework given in [144] by adding a thermal dependency, thus obtaining a model that accounted for strain hardening, strain-rate sensitivity, thermal softening and heat conduction.

The assumption of adiabatic deformation results in the increase of heat generation in the regions of high strain rates. Clifton et al. [23] postulated that non-uniform deformation is expected since strain rates tend to increase in the hotter regions and decrease in colder. Critical instabilities were also examined by Culver [27] and Staker [180]; both authors suggested that critical instability strain is determined by the point in stress-strain relation where the curve vanishes. In [108], Litoński considered a temperature-dependent and strain-rate sensitive empirical material model. By subjecting geometrically inhomogeneous tubes to torsion, he was able to confirm, what was previously

suggested by others, that initiation of instability corresponds to the peak value in the torque-twist relation. In [130] and [131] authors were able to find critical conditions, in closed form, for shear localization in thermo-viscoplastic material for models that neglect the heat conductivity, inertia and elasticity. Shawki and Clifton [175] investigated a one-dimensional model for simple shearing deformation of thermal viscoplastic material with a particular focus on shear strain localization under high strain rates. The authors concluded that thermal softening plays a key role in reducing the material stiffness which promotes the localization. Conversely, at small strains, strain hardening often dominates thermal softening and the net interaction between results in the lack of localization. Large plastic strains are required so that the thermal softening overwhelms strain hardening and localization can take place. The dynamics of shear band formation was studied in [215], making use of simplified thermo-viscoplastic flow law. Grady [69] presented a study of adiabatic shear bands, utilizing thermoviscous plasticity and heat transfer laws, in the two-material two-temperature body. In this paper, the author had investigated the shear band dissipation rate and shear band toughness, which was calculated for the number of metals. Meyer et al. [125] investigated changes in microstructure adjacent to previously generated shear bands. They provided evidence that plastic deformation, coupled with temperature rise, leads from a dislocated/twinned/transformed structure to the breakup into small regions separated by geometrically-necessary boundaries. The subject of adiabatic shear localization was also extensively discussed in textbooks devoted to this problem, e.g. [216] and [36].

Several of the previously mentioned studies have attempted to use the viscous models to reproduce the rate-dependent inelastic deformation. In the following section, the topic of the viscoplastic model and its limitations are discussed.

1.2.4. Viscoplasticity

In 1963 Perzyna published a paper [148] where he outlined th e fundamental formulation of the classical (rate-dependent) viscoplasticity. The idea and different aspects of this theory also referred to in the literature as the theory of thermo-viscoplasticity (TTV) [195], were discussed in many works since its inception. The conditions for the existence and uniqueness of the softening problem were studied in [154], while well-posedness of the problem was discussed in [62, 226, 227]. The propagation of mechanical and thermal waves in the viscoplastic medium was examined in [61, 63]. The material parameter that denotes relaxation time for mechanical disturbances was analyzed in [64, 65], additionally, the dispersive character of the model was discussed in [64] and energy dissipation in [65]. The identification of material parameters at elevated temperatures was examined in [93].

The basic model was extended with the damage mechanism was introduced in [67, 155] and developed in [184]. The fracture propagation in processes where high impact velocities were regraded was examined in [41, 43]. The study of the thermo-viscoplastic flow processes under cyclic dynamic loading was conducted in [39, 40].

In [67] the topic of the smooth and non-smooth distributions within damage and failure was raised. The description of the role of covariance, i.e. the invariance with respect to any diffeomorphism, was discussed in [109, 185]. Finally, the numerical scheme for viscoplasticity was presented by Simo and Hughes [177], as well as by de Souza Neto et al. [33].

The problems of non-local and anisotropic material properties can be a severe limitation in modelling dynamic behaviour. Therefore, the formulation of the viscoplasticity enhanced with the fractional operator is discussed in the next section.

1.2.5. Fractional calculus

Useful reviews of the mathematical foundations of fractional calculus and methods for solving fractional differential equations have been given in [45, 68, 140, 160].

Several papers presenting various applications of the fractional operator throughout various scientific fields indicate the potential of this approach to solve problems or generalize existing solutions. Among the areas where fractional calculus was used physics [52, 74], control theory [183, 220], electrical engineering [53], bioengineering [51, 112, 113], finance theory [116, 174], signal processing [7, 122], should be mentioned. A wide variety of mathematical tools and methods, which builds the core of continuum mechanics, present a great opportunity for using fractional calculus to generalize classical field theories. Examples of fractional operators applications in mechanics can be found in [14, 16, 17, 98, 103, 104, 105, 120, 187, 188, 189]. Generalization of continuum models that describe the rate-dependent behavior of solids is a subject of interest in this treatise. Thus, in the two subsequent paragraphs works concerning non-integer order viscoelastic and viscoplastic formulations are discussed.

Fractional calculus was used to write constitutive relations that were found to be equivalent to molecular theories of viscoelasticity [9]. The same group of researchers in [8] applied the fractional operator to stress-strain relation in viscoelastic dampers. It was found that the new model required a few parameters to predict the material response. Creep and relaxation function were generalized, in the framework of non-integer order calculus, which led to the reduction of creep and relaxation data [94]. Comprehensive outlook on fractional calculus, linear viscoelasticity, wave motion and how these can be used in conjunction was given in [115].

The study of the fractional viscoplasticity was first carried out by Sumelka in [186]. It was found that in the new formulation of Perzyna theory, the non-associated flow was obtained without any additional potential assumption. In the subsequent paper, Sumelka and Nowak [190] demonstrated that the fractional operator introduces non-locality in the stress space, although this study was based on the rate-independent model. Numerical investigation revealed that new formulation allows the volume change in the inelastic range, induces plastic anisotropy and non-normality of plastic flow. The problem of non-locality was extensively presented in [195]. In [200] authors investigated the Perzyna-type viscoplastic model in the framework of non-integer order

calculus. It was shown that the new model exhibits features such as rate-dependence, plastic anisotropy, non-normality, directional viscosity, material non-locality and stress-fractional non-locality. Method for overcoming limitations of Riesz-Caputo fractional derivative, by finding an approximate solution for any smooth and coves yield function, was discussed in [191].

The idea of using fractional approach for modelling inealstic behaviour of geomaterials, as mentioned in section 1.2.2, has been already utilized by researchers. Sun and Shen [197] demonstrated that by using non-integer order operator non-associated flow can be achieved without additional assumption. This allows the use of already determined material constants with only one additional parameter – fractional order. In [198] authors proposed and studied fractional flow rule model for granular soils under triaxial loading. Sun et al. [196] showed that current and critical stress states can be used as bounds of the integral in the fractional derivative definition.

1.2.6. Summary

Viscoplasticity proved to be a reliable approach to model the rate-dependent inelastic properties. In addition, the basic form of this theory can be fairly easily extended to include thermal and micro-mechanical phenomena that occur in metals. The applicability of this theory has been significantly expanded through the use of fractional calculus. Materials such as metals, rubbers, geomaterials, concrete and composites that may require a time-dependent formulation accounting for non-normality and anisotropy are suitable research problems for the fractional viscoplasticity.

Although some research has been carried out on fractional inviscid models, there have been few empirical investigations into a rate-dependent description of material behaviour. Moreover, no research has been found that surveyed the problem of the impact of parameters, which originate both from fractional and viscoplastic formulation, on material response. Finally, the dynamic behaviour of the material forges an interesting research question, which has not been thoroughly studied in the framework of fractional calculus, that can deliver practical relevance in the field of structural engineering. The reason for this dissertation is to fill a gap in the existing literature, hoping that the reader will benefit from it in some way.

1.3. Aims and objectives

The aim of this dissertation is to study the dynamic behaviour of the metallic materials in the framework of the fractional viscoplastic model. A numerical parametric study for a case of dynamic loading allows for an in-depth look into a material response. There are two groups of parameters that can be distinguished. The first group results from extending the basic viscoplasticity in the framework of fractional calculus – these are referred to as fractional parameters. The second group has its origin in the original formulation given by Perzyna, but should be studied afresh for the new model. Basic

intuition about the dynamic behaviour can be gathered from analyses conducted at the material point. However, to investigate the aspects of non-locality and non-normality of viscoplastic flow in the fractional framework a full 3-D model has to be examined. It is a subject of another set of numerical simulations conducted for the viscoplastic model extended with additional phenomena, such as adiabatic temperature generation, the evolution of microdamage and isotropic work-hardening/softening.

The different objectives of the treatise to model the inelastic behaviour of metallic materials in the framework of the fractional viscoplasticity were listed below.

- Modification of numerical procedure used in previous studies [191, 200] to include thermal and mechanical effects of deformation in the fractional viscoplastic formulation.
- Development of a finite element model of an infinitesimal material point to study the fundamental behaviour of the fractional procedure.
- Development of a finite element model of a full 3-D specimen to study the anisotropy and localization of deformation.
- Analysis of the relation between the material parameters of the fractional model and the dispersion of the stress waves.
- Analysis of the impact of the parameters, which stem from both the fractional and viscous approaches, on elementary stress-strain relation at the material point.
- Examination of the various deformation modes depending on the fractional parameters in the case of dynamic loading. Additionally, in this case, strain localization and anisotropy of the inelastic deformation is anticipated.
- Analysis of the state variables and their relations, during the dynamic tensile test until the moment of fracture.

Based on the above, a following thesis for this dissertation can be formulated:

The fractional formulation of the viscoplastic model improves the description of metals behaviour under dynamic loading.

The validity of this statement will be verified during the implementation of the objectives of this dissertation.

1.4. Outline

The remaining chapters of this dissertation are structured as follows:

Chapter 2: Foundations of continuum mechanics and finite element method. In this chapter, a tensor analysis is used to describe the motion and the deformation of a continuous matter. Next, the concept of stress in the form of Cauchy, first Piola-Kirchoff and second Piola-Kirchoff stress tensors are formulated. Balance principles are subsequently introduced together with fundamental laws of thermodynamics. The rules that ought to be followed in creating new material models are later discussed. In the last part of this chapter, an overview of the finite element method and the explicit time integration scheme is given.

Chapter 3: Fractional stress-gradient viscoplasticity. This chapter begins with a terse introduction to the fractional calculus with a particular focus on the Riesz-Caputo derivative. This concept is then applied to Perzyna's theory of viscoplasticity, resulting in a new model of fractional viscoplasticity. It is followed by a detailed description of the numerical implementation. Finally, the behaviour of the model is examined in a number of numerical examples that study the influence of the new material parameters and the parameters resulting from classical viscoplasticity. The foregoing examples are the original results that present the dynamic response of the fractional model.

Chapter 4: Fractional Viscoplasticity with extended constitutive structure. The fractional model is further developed in this chapter. The thermo-mechanical coupling, isotropic work-hardening/softening and the microdamage mechanism that governs the fracture criterion are added to the previously presented model. This requires a new implementation scheme to be drafted to include a new constitutive structure. Finally, the second set of original results is presented. Although, this time the deformation of a dog-bone specimen is studied in order to capture the full spatial performance of the new model. The parametric study is focused on the influence of the fractional parameters on the deformation type and the state variables. Also, the damage localization and the failure evolution in the material are closely studied.

Chapter 5: Conclusion and Future Work. All the results of the preceding chapters are summarised and possible directions for further research are outlined.

1.5. Published work

1.5.1. International journals

1. **M. Szymczyk**, M. Nowak, and W. Sumelka. Plastic strain localization in an extreme dynamic tension test of steel sheet in the framework of fractional viscoplasticity. *Thin-Walled Structures*, 2019. DOI: 10.1016/j.tws.2019.106522.

2. **M. Szymczyk**, M. Nowak, and W. Sumelka. Numerical study of dynamic properties of fractional viscoplasticity model. *Symmetry*, 10(7), 2018. DOI: 10.3390/sym10070282.

3. **M. Szymczyk**, W. Sumelka, and T. Łodygowski. Numerical investigation on ballistic resistance of aluminium multi-layered panels impacted by improvised projectiles, *Archive of Applied Mechanics*, 2017. DOI: 10.1007/s00419-017-1247-8.

1.5.2. Conference papers and presentations

1. **M. Szymczyk**, M. Nowak, W. Sumelka, and T. Łodygowski, Strain localization analysis in terms of fractional viscoplasticity, *4th Polish Congress of Mechanics and 23rd International Conference on Computer Methods in Mechanics*, Kraków, September 8–12, 2019.

2. **M. Szymczyk**, W. Sumelka, and M. Nowak, Initial boundary value problem in the framework of fractional viscoplasticity, *The 41st Solid Mechanics Conference (SOLMECH 2018)*, Warszawa, August 27–31, 2018.

3. **M. Szymczyk**, W. Sumelka and M. Nowak, On selected aspects of fractional plasticity, *The 22nd International Conference on Computer Methods in Mechanics*, Lublin, September 13–16 2017.

4. **M. Szymczyk**, W. Sumelka and M. Nowak, Fundamental parameters in the fractional viscoplastic model, *11th Workshop – Dynamic Behaviour of Materials and its Applications in Industrial Processes*, Guimarães, Portugal, August 23–25 2017.

5. **M. Szymczyk**, W. Sumelka, T. Łodygowski, The numerical analysis of perforation of multilayered aluminum panels, *The 10th Workshop – Dynamic Behaviour of Materials and its Applications in Industrial Processes*, Poznań, August 24–26 2016.

6. **M. Szymczyk**, W. Sumelka, T. Łodygowski (Chapter), Designing of multilayered protective panels against improvised debris, *Proceedings of the 13th International Scientific Conference*, Springer International Publishing, 2016, DOI: 10.1007/978-3-319-50938-9.

Chapter 2

Foundations of continuum mechanics and finite element method

2.1. Introduction

Continuum mechanics deals with a macroscopic description of motion and deformation regarding solid bodies, fluids and gases. A physical body, which is composed of molecules distributed in space, can be modeled with an uncountable set of particles that interact with each other. On a continuum body, functions describing its internal state and interactions between particles may be applied. Functions derived from this assumption allow replacing discontinuous medium with tensor field quantities. The material presented in this chapter is well established in literature and notation used here follows nomenclature presented in Truesdell and Noll [209], Holzapfel [79], Kowalczyk and Kleiber [96] and Ostrowska-Maciejewska [143].

In this work a mathematical structures and laws of continnum mechanics are used as foundation for new formulation of inelastic model describing the rate-dependent deformation in metals. This chapter introduces basic concepts that will serve as a prerequisites for further considerations; here were divided into following parts:

- kinematics,
- concept of stress,
- laws of conservation,
- principles of material modelling,
- finite element method.

2.2. Kinematics

A physical body $\mathcal{B}$ that occupies a certain position in Euclidean space $\mathcal{E}^3$ is, in fact, a grouping of particles P, where $P \in \mathcal{B}$. Motion and deformation of $\mathcal{B}$ are observed both in time and space as it moves from one occupied region to another, as shown in Fig. 2.1. Those regions are denoted by $\Omega_0, \ldots, \Omega_c$ and are referred to as the configurations of $\mathcal{B}$ in different time frames t. Typically the region Ω_0 corresponds to an initial time $t = 0$ and is called the reference, or the undeformed, configuration of the body $\mathcal{B}$. Subsequently, as the motion of $\mathcal{B}$ progresses, it will move to a different region in space, denoted by Ω_c and named a current, or deformed configuration. The position vectors $\boldsymbol{X}$ and $\boldsymbol{x}$ serve as labels for points P in the reference and current configuration, respectively. Component (or index) notation of these vectors is as follows:

$$\boldsymbol{X} = X_i \hat{\boldsymbol{E}}_i, \tag{2.1}$$

and

$$\boldsymbol{x} = x_i \hat{\boldsymbol{e}}_i, \tag{2.2}$$

where $\hat{\boldsymbol{E}}_i$ and $\hat{\boldsymbol{e}}_i$ are basis vectors and $i = 1, 2, 3$. In this thesis rectangular Cartesian or simply Cartesian basis system is used, which means that basis vectors are unit and orthogonal (orthonormal). An absolute (or direct) notation of tensors is also used later in this text. The direct notation has the advantage that it accentuates the fact that physical relationships are independent of the choice of the coordinate system [179]. Moreover, Eqs. 2.1 and 2.2 were written according to the summation convention used to concisely write long equations with additive terms.

The components X_i are known as material, or referential, coordinates of point P in Ω_0 configuration, whereas x_i are referred to as spatial, or current, coordinates of P in Ω_c configuration. Uppercase letters denote scalar, vector and tensor quantities that were formulated in reference configuration and lowercase letters are used for quantities in the current configuration. Assuming one and universal frame of reference, used regardless of the present configuration of the body $\mathcal{B}$, both sets of basis vectors, $\hat{\boldsymbol{E}}_i$ and $\hat{\boldsymbol{e}}_i$, become equal.

Mapping of a particle P into point $\boldsymbol{X} \in \Omega_0$ $(t = 0)$ is achieved by one-to-one function ζ_0, such as

$$\boldsymbol{X} = \zeta_0(P, t). \tag{2.3}$$

Similarly, for $t > 0$ a map

$$\boldsymbol{x} = \zeta(P, t), \tag{2.4}$$

that acts on $\mathcal{B}$ to create configuration Ω_c can be defined.

The motion of $\mathcal{B}$ manifests itself in the changes of the configurations Ω of the body and position vectors $\boldsymbol{x}$ associated with particles P. For this a vector function ϕ has to be determined in the following form

$$\boldsymbol{x} = \phi(\boldsymbol{X}, t) = \zeta\left[\zeta_0^{-1}(\boldsymbol{X}, t)\right]. \tag{2.5}$$

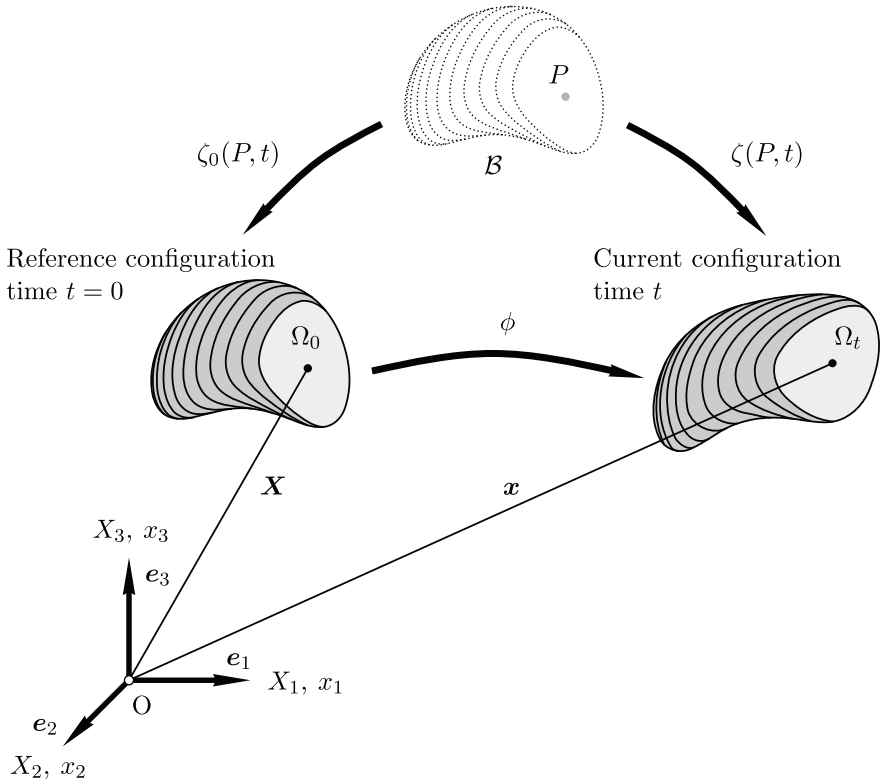

Figure 2.1. Motion of body $\mathcal{B}$ between two configurations

Continuous motion ϕ follows particle P as it successively changes positions thus creating a curve in $\mathcal{E}^3$ known as pathline or trajectory. Motion is categorized as invertible transformation, which is expressed in a statement

$$\boldsymbol{X} = \phi^{-1}(\boldsymbol{x}, t), \tag{2.6}$$

with ϕ^{-1} denoting an inversed mapping of points located in a current configuration Ω_c into reference configuration Ω_0.

Material description of motion is formulated with respect to the material coordinates and also known as Langrangian description. Similarly, the name spatial description is used to describe motion in terms of spatial coordinates or historically as Eulerian description.

Displacement of particle P between reference and the current configuration is given by the formula

$$\boldsymbol{U}(\boldsymbol{X}, t) = \boldsymbol{x}(\boldsymbol{X}, t) - \boldsymbol{X} \tag{2.7}$$

evaluated in terms of Lagrangian description. Similarly, the displacement field can be express in terms of Eulerian description, that is

$$\boldsymbol{u}(\boldsymbol{x},t) = \boldsymbol{x} - \boldsymbol{X}(\boldsymbol{x},t). \tag{2.8}$$

Equation (2.7) evaluates the displacement of a particle at time t in association with its referential position $\boldsymbol{X}$. Field $\boldsymbol{u}(\boldsymbol{x},t)$, postulated in Eq. (2.8), proves that displacement can be expressed in terms of the current position, making both notations equivalent

$$\boldsymbol{u}(\boldsymbol{x},t) = \boldsymbol{U}[\phi^{-1}(\boldsymbol{x},t),t] = \boldsymbol{U}(\boldsymbol{X},t). \tag{2.9}$$

One of the crucial quantities in the field of the nonlinear continuum mechanics is a deformation gradient

$$\boldsymbol{F}(\boldsymbol{X},t) = \frac{\partial \phi(\boldsymbol{X},t)}{\partial \boldsymbol{X}}, \tag{2.10}$$

also expressed in a following manner

$$\boldsymbol{F}(\boldsymbol{X},t) = \mathrm{Grad}[\boldsymbol{x}(\boldsymbol{X},t)] = \nabla \phi(\boldsymbol{X},t), \tag{2.11}$$

where $\nabla(\cdot)$ is a gradient operator. $\boldsymbol{F}$ is a second-order tensor that in general has nine components given by

$$F_{aA} = \frac{\partial \phi_a}{\partial X_A}. \tag{2.12}$$

Treating $\boldsymbol{F}$ as a linear operator acting on an infinitesimal line element in reference configuration $d\boldsymbol{X}$, we obtain

$$d\boldsymbol{x} = \boldsymbol{F}(\boldsymbol{X},t)\, d\boldsymbol{X}, \tag{2.13}$$

where $d\boldsymbol{x}$ denotes an infinitesimal line element in the current (deformed) configuration. The deformation gradient binds undeformed and deformed configurations, but a condition of nonsingularity has to be also fulfilled so it could act as a one-to-one map. This can be assured by the existence of an inverse operator

$$\boldsymbol{F}^{-1}(\boldsymbol{x},t) = \mathrm{grad}[\boldsymbol{X}(\boldsymbol{x},t)] = \frac{\partial \phi^{-1}(\boldsymbol{x},t)}{\partial \boldsymbol{x}}, \tag{2.14}$$

denoted as inverse deformation gradient. Notation Grad[.] and grad[.] indicates that the gradient operator is defined with respect to reference or current configuration. It has the ability to carry spatial line element $d\boldsymbol{x}$ to the material line element $d\boldsymbol{X}$ via the following relationship

$$d\boldsymbol{X} = \boldsymbol{F}^{-1}(\boldsymbol{x},t)\, d\boldsymbol{x}. \tag{2.15}$$

For the existence of $\boldsymbol{F}^{-1}$, the following condition has to be met, namely

$$J(\boldsymbol{X},t) = \det[\boldsymbol{F}(\boldsymbol{X},t)] \neq 0, \tag{2.16}$$

where J is known as the volume ratio or the Jacobian determinant. It is the measure of a volume change produced by a deformation

$$d\mathrm{v} = J(\boldsymbol{X},t)\, d\mathrm{V}, \tag{2.17}$$

where $d\mathrm{V}$ and $d\mathrm{v}$ are infinitesimal volume elements in the reference and current configurations, respectively. The volume of deformed element ($d\mathrm{v}$), must be positive. Therefore, physically admissible deformation must satisfy

$$J(\boldsymbol{X}, t) > 0. \tag{2.18}$$

The assumption that body $\mathcal{B}$ does not move ($\boldsymbol{F} = \mathbb{1}$ and $\boldsymbol{x} = \boldsymbol{X}$) results in $J = 1$. However, for a body in motion, condition $J = 1$ may be true as well. In such case, the deformation has an isochoric or volume-preserving character.

Similarly, a relation between the infinitesimal area element in undeformed ($d\mathbf{A}$) and deformed ($d\mathbf{a}$) configurations follows Nanson's formula

$$d\mathbf{a} = \mathrm{cof}[\boldsymbol{F}]\, d\mathbf{A}, \tag{2.19}$$

with the cofactor $\mathrm{cof}[\boldsymbol{F}] = \det[\boldsymbol{F}]\, \boldsymbol{F}^{-T}$ and vector elements defined as $d\mathbf{a} = \boldsymbol{n}\, d\mathrm{a}$ and $d\mathbf{A} = \boldsymbol{N}\, d\mathrm{A}$. $\boldsymbol{N}$ and $\boldsymbol{n}$ are normal vectors perpendicular to the surface elements $d\mathrm{A}$ (reference configuration) and $d\mathrm{a}$ (actual configuration), respectively.

The polar decomposition requires for it subject to be an invertible (nonsingular) tensor and is as follows

$$\boldsymbol{F} = \mathbf{R}\mathbf{U} = \mathbf{V}\mathbf{R}, \tag{2.20}$$

where $\mathbf{R}$ is a rotation tensor, $\mathbf{U}$ and $\mathbf{V}$ are right and left stretch tensors, respectively.

The operation of squaring infinitesimal line elements $d\boldsymbol{x}$ and $d\boldsymbol{X}$ allows formulating two important deformation tensors

$$\boldsymbol{C} = \boldsymbol{F}^T\boldsymbol{F}, \tag{2.21}$$

and

$$\boldsymbol{c} = \boldsymbol{F}\boldsymbol{F}^T, \tag{2.22}$$

named right and left Cauchy-Green tensors. By stating the symmetry of stretch tensor ($\mathbf{U} = \mathbf{U}^T$) and orthogonality of rotation tensor ($\mathbf{R}^{-1} = \mathbf{R}^T$) the following holds true:

$$\boldsymbol{C} = \boldsymbol{F}^T\boldsymbol{F} = \mathbf{U}^T\mathbf{R}^T\mathbf{R}\mathbf{U} = \mathbf{U}^T\mathbf{U}, \tag{2.23}$$

and

$$\boldsymbol{c} = \boldsymbol{F}\boldsymbol{F}^T = \mathbf{V}\mathbf{R}\mathbf{R}^T\mathbf{V}^T = \mathbf{V}\mathbf{V}^T. \tag{2.24}$$

The definition of a strain tensor can be achieved by subsequent use of $d\boldsymbol{x}$ and $d\boldsymbol{X}$, more precisely by considering the difference of its squares

$$\boldsymbol{E} = \frac{1}{2}\big(\boldsymbol{F}^T\boldsymbol{F} - \mathbb{1}\big), \tag{2.25}$$

and

$$\boldsymbol{e} = \frac{1}{2}\big(\mathbb{1} - \boldsymbol{F}^{-T}\boldsymbol{F}^T\big), \tag{2.26}$$

That leads to two new formulations that are denoted in the literature as Green and Almansi strain tensors. Components of the strain tensors can be expressed in terms of the displacement field

$$\boldsymbol{E} = \frac{1}{2}\big(\mathrm{Grad}^T[\boldsymbol{U}] + \mathrm{Grad}[\boldsymbol{U}]\big) + \frac{1}{2}\mathrm{Grad}^T[\boldsymbol{U}]\,\mathrm{Grad}[\boldsymbol{U}], \tag{2.27}$$

$$\boldsymbol{e} = \frac{1}{2}\big(\mathrm{grad}^T[\boldsymbol{u}] + \mathrm{grad}[\boldsymbol{u}]\big) + \frac{1}{2}\mathrm{grad}^T[\boldsymbol{u}]\,\mathrm{grad}[\boldsymbol{u}], \tag{2.28}$$

in material and spatial description, respectively. In index notation

$$E_{AB} = \frac{1}{2}\left(\frac{\partial U_B}{\partial X_A} + \frac{\partial U_A}{\partial X_B}\right) + \frac{1}{2}\frac{\partial U_C}{\partial X_A}\frac{\partial U_C}{\partial X_B}, \tag{2.29}$$

$$e_{ab} = \frac{1}{2}\left(\frac{\partial u_b}{\partial x_a} + \frac{\partial u_a}{\partial x_b}\right) + \frac{1}{2}\frac{\partial u_c}{\partial x_a}\frac{\partial u_c}{\partial x_b}. \tag{2.30}$$

The nonlinear terms in Eqs. (2.27) and (2.28) can be neglected when displacement gradients are infinitesimally small, i.e. $|\mathrm{Grad}[\boldsymbol{U}]| \ll 1$ (or $|\mathrm{grad}[\boldsymbol{u}]| \ll 1$). Material and spatial descriptions are indistinguishable for infinitesimals strains and therefore Green and Almansi tensor become equal. The infinitesimal strain tensor is therefore given by

$$\boldsymbol{\varepsilon} = \frac{1}{2}\big(\mathrm{grad}^T[\boldsymbol{u}] + \mathrm{grad}[\boldsymbol{u}]\big) = \boldsymbol{E} = \boldsymbol{e}, \tag{2.31}$$

or in index notation as

$$\varepsilon_{ab} = \frac{1}{2}\left(\frac{\partial u_b}{\partial x_a} + \frac{\partial u_a}{\partial x_b}\right). \tag{2.32}$$

Material and spatial time derivatives define velocity in the material description ($\boldsymbol{V}$) and spatial description ($\boldsymbol{v}$) as

$$\boldsymbol{V}(\boldsymbol{X}, t) = \frac{\partial \phi(\boldsymbol{X}, t)}{\partial t} = \dot{\boldsymbol{x}}, \tag{2.33}$$

and

$$\boldsymbol{v}(\boldsymbol{x}, t) = \boldsymbol{V}(\phi^{-1}(\boldsymbol{x}, t), t), \tag{2.34}$$

where $\dot{(\cdot)}$ is a common abbreviated notation of the first derivative with respect to time. Since the velocity depends on the position of particles, the spatial velocity gradient can be introduced with respect to the spatial coordinates

$$\boldsymbol{l}(\boldsymbol{x}, t) = \frac{\partial \boldsymbol{v}(\boldsymbol{x}, t)}{\partial \boldsymbol{x}} = \mathrm{grad}[\boldsymbol{v}(\boldsymbol{x}, t)]. \tag{2.35}$$

Index notation reveals the detailed composition of this tensor, namely

$$l_{ij} = \frac{\partial v_i}{\partial x_j}. \tag{2.36}$$

The velocity gradient can be decomposed into symmetric and skew-symmetric parts, as

$$\boldsymbol{l}(\boldsymbol{x},t) = \boldsymbol{d}(\boldsymbol{x},t) + \boldsymbol{w}(\boldsymbol{x},t), \tag{2.37}$$

where

$$\boldsymbol{d} = \frac{1}{2}(\boldsymbol{l} + \boldsymbol{l}^T) = \frac{1}{2}\Big(\mathrm{grad}[\boldsymbol{v}] - \mathrm{grad}^T[\boldsymbol{v}]\Big) = \boldsymbol{d}^T, \tag{2.38}$$

and

$$\boldsymbol{w} = \frac{1}{2}(\boldsymbol{l} - \boldsymbol{l}^T) = \frac{1}{2}\Big(\mathrm{grad}[\boldsymbol{v}] + \mathrm{grad}^T[\boldsymbol{v}]\Big) = -\boldsymbol{w}^T. \tag{2.39}$$

In the above, $\boldsymbol{d}$ is the rate of deformation tensor (or rate of stretching tensor) and $\boldsymbol{w}$ denotes the spin tensor (or rate of rotation). The time derivative of the deformation gradient can be expressed as

$$\dot{\boldsymbol{F}}(\boldsymbol{X},t) = \frac{\partial}{\partial t}\left(\frac{\partial \phi(\boldsymbol{X},t)}{\partial \boldsymbol{X}}\right) = \frac{\partial}{\partial \boldsymbol{X}}\left(\frac{\partial \phi(\boldsymbol{X},t)}{\partial t}\right) = \frac{\partial \boldsymbol{V}(\boldsymbol{X},t)}{\partial \boldsymbol{X}} = \mathrm{Grad}[\boldsymbol{V}(\boldsymbol{X},t)], \tag{2.40}$$

where $\mathrm{Grad}[\boldsymbol{V}(\boldsymbol{X},t)]$ is a material velocity gradient and is equal to $\dot{\boldsymbol{F}} = D\boldsymbol{F}/Dt$. The spatial velocity gradient relates to the material velocity gradient in the following manner

$$\boldsymbol{l}(\boldsymbol{x},t) = \frac{\partial \boldsymbol{v}(\boldsymbol{x},t)}{\partial \boldsymbol{x}} = \frac{\partial \dot{\phi}(\boldsymbol{X},t)}{\partial \boldsymbol{X}}\frac{\partial \boldsymbol{X}}{\partial \boldsymbol{x}} = \dot{\boldsymbol{F}}\boldsymbol{F}^{-1}. \tag{2.41}$$

The derivative of Jacobian determinant with respect to time yields

$$\dot{J} = \frac{\partial \det[\boldsymbol{F}]}{\partial \boldsymbol{F}} : \frac{\partial \boldsymbol{F}}{\partial t} = J\boldsymbol{F}^{-T} : \dot{\boldsymbol{F}} = J\, tr[\boldsymbol{l}] = J\,\mathrm{div}[\boldsymbol{v}]. \tag{2.42}$$

2.3. The concept of stress

Motion and deformation of the body increase the intensity with which neighbouring particles are acting on each other. A postulate can be raised that it will create an internal interaction pressure between particles $P \in \mathcal{B}$. Cross-section of $\mathcal{B}$ exposes an internal surface where an infinitesimal spatial surface $d\mathrm{a}$ with a normal vector $\boldsymbol{n}$ at a point $\boldsymbol{x}$ can be chosen – Fig. 2.2. Those quantities are evaluated for current configuration but can be mapped to reference and denoted as $d\mathrm{A}$, $\boldsymbol{N}$, $\boldsymbol{X}$. The Cauchy (true) traction vector, denoted as $\tilde{\boldsymbol{t}}$ acts upon $d\mathrm{a}$ and is given by

$$d\boldsymbol{f} = \tilde{\boldsymbol{t}}\, d\mathrm{a} = \tilde{\boldsymbol{T}}\, d\mathrm{A}, \tag{2.43}$$

$$\tilde{\boldsymbol{t}} = \tilde{\boldsymbol{t}}(\boldsymbol{x},\boldsymbol{n}), \qquad \tilde{\boldsymbol{T}} = \tilde{\boldsymbol{T}}(\boldsymbol{X},\boldsymbol{N}), \tag{2.44}$$

where $d\boldsymbol{f}$ is a density of forces acting on an infinitesimal surface. The unit of $\tilde{\boldsymbol{t}}$ is a force per unit surface. $\tilde{\boldsymbol{T}}$ defines the first Piola-Kirchhoff vector, which has the same direction as $\tilde{\boldsymbol{t}}$ but is defined in terms of undeformed configuration. Vectors $\tilde{\boldsymbol{t}}$ and $\tilde{\boldsymbol{T}}$ are also referred to as surface tractions, contact forces, stress vectors or loads.

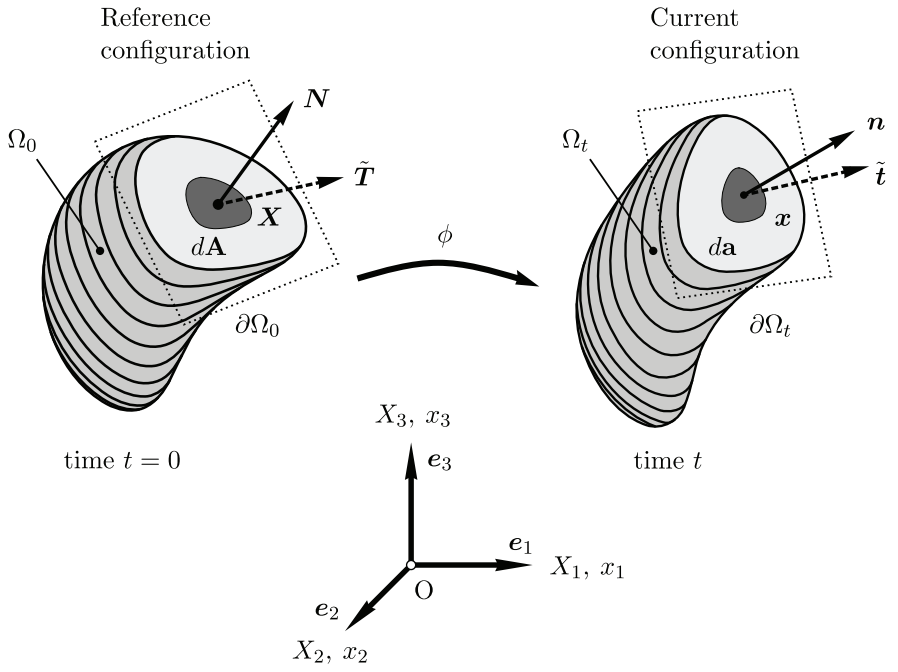

Figure 2.2. Traction vectors exerted on infinitesimal surface elements. The dotted line illustrates the place of cut by the plane surface

Cauchy's stress theorem states that there exist the second-order tensor fields $\boldsymbol{\sigma}(\boldsymbol{x}, t)$ and $\boldsymbol{P}_{PK}(\boldsymbol{x}, t)$ independent of $\boldsymbol{n}$ (or $\boldsymbol{N}$), that

$$\tilde{\boldsymbol{t}}(\boldsymbol{x}, \boldsymbol{n}) = \boldsymbol{\sigma}(\boldsymbol{x}, t)\, \boldsymbol{n}, \tag{2.45}$$

$$\tilde{\boldsymbol{T}}(\boldsymbol{X}, \boldsymbol{N}) = \boldsymbol{P}_{PK}(\boldsymbol{X}, t)\, \boldsymbol{N}, \tag{2.46}$$

where:

$\boldsymbol{\sigma}$ is the Cauchy stress tensor, and
$\boldsymbol{P}_{PK}$ is the first Piola-Kirchhoff stress tensor.

According to the principle of the conservation of angular momentum, $\boldsymbol{\sigma}$ is a symmetric tensor, whereas $\boldsymbol{P}_{PK}$ does not exhibit symmetry. Lack of symmetry stems from the fact that the normal vector ($\boldsymbol{N}$) is attached to the reference configuration and the resulting stress vector refers to the current configuration. To overcome this a pullback mapping can be utilized so that

$$\boldsymbol{S}_{PK} = \boldsymbol{F}^{-1} \boldsymbol{P}_{PK}, \tag{2.47}$$

where $\boldsymbol{S}_{PK}$ is a symmetric second Piola-Kirchhoff stress tensor.

One of the alternative stress measure useful in formal modelling is Kirchhoff stress tensor $\boldsymbol{\tau}$ and is defined via

$$\boldsymbol{\tau} = J\boldsymbol{\sigma}. \tag{2.48}$$

Kirchhoff stress tensor can be also obtained as a result of a pushforward of the second Piola-Kirchhoff tensor to the current configuration

$$\boldsymbol{\tau} = \boldsymbol{F}\boldsymbol{S}_{PK}\boldsymbol{F}^T. \tag{2.49}$$

2.4. Conservation of mass, momenta and energy

Models of physical phenomena are based on fundamental laws of physics that govern and restrict the behaviour of a mechanical system. They can not be derived from other relations and have to be satisfied at all times. The constitutive relation (stress-strain equations) and both initial and boundary conditions also have to be included to obtain stress, deformation or displacement fields.

2.4.1. Conservation of mass

Mass of body $\mathcal{B}$ is a fundamental property of every continuum body. Law of conservation states that for body $\mathcal{B}$, enclosed by the boundary surface $\partial\mathcal{B}$, no mass can enter or leave the boundary during the deformation process. Global formulation of the mass conservation is therefore given via

$$m_{\mathcal{B}} = \int_{\Omega_0} \rho_0(\boldsymbol{X})\, d\mathrm{V} = \int_{\Omega_c} \rho(\boldsymbol{x}, t)\, d\mathrm{v} = \text{const.} \tag{2.50}$$

where ρ_0 and ρ denote referential and current density, respectively. Using Eq. (2.17) a local form (local formulation) of the mass conservation principle is obtained

$$J(\boldsymbol{X}, t) = \frac{\rho_0(\boldsymbol{X})}{\rho(\boldsymbol{x}, t)} = \frac{\rho_0(\boldsymbol{X})}{\rho(\phi(\boldsymbol{X}, t), t)}, \tag{2.51}$$

valid for material (or Lagrangian) description, which is an appropriate description for solid mechanics. For the sake of clarity, explicit notation of arguments is abandoned till the end of this section. The condition that mass of the body remains constant (2.50) implies that time derivative of mass must be zero, i.e.

$$\dot{m}_{\mathcal{B}} = \frac{D}{Dt}\int_{\Omega_c} \rho\, d\mathrm{v} = \frac{D}{Dt}\int_{\Omega_0} \rho\, J\, d\mathrm{V} = \int_{\Omega_0} \left(\dot{\rho}J + \rho\dot{J}\right) d\mathrm{V} = 0, \tag{2.52}$$

where $\dot{\rho}$ denotes time derivative of density. Combining Eq. (2.52) with the time derivative of Jacobian determinant (2.42) leads to alternative local form of the mass conservation

$$\dot{\rho} + \rho\, \mathrm{div}(\boldsymbol{v}) = 0, \tag{2.53}$$

where $\boldsymbol{v}$ is the spatial velocity field $\boldsymbol{v}(\boldsymbol{x}, t)$.

2.4.2. Conservation of linear momentum

Momentum is a measure of the tendency of a body to keep moving one it was set in motion. The rate of change of momentum is equal to all external forces – this is called the principle of linear momentum and can be formulated similarly to Newton's second law

$$\dot{\mathbf{p}} = \frac{d\mathbf{p}}{dt} = m_{\mathcal{B}} \frac{d\boldsymbol{v}}{dt} = m_{\mathcal{B}}\, \mathbf{a} = \mathbf{F}. \tag{2.54}$$

This fundamental law can be generalized in terms of the mechanics of a continuum in the following form

$$\dot{\mathbf{L}}(t) = \frac{D}{Dt} \int_{\Omega_c} \rho(\boldsymbol{x}, t) \boldsymbol{v}(\boldsymbol{x}, t)\, \mathrm{dv} = \frac{D}{Dt} \int_{\Omega_0} \rho_0(\boldsymbol{X}, t) \boldsymbol{V}(\boldsymbol{X}, t)\, \mathrm{dV} = \mathbf{F}(t), \tag{2.55}$$

where $\boldsymbol{V}(\boldsymbol{X}, t)$ and $\boldsymbol{v}(\boldsymbol{x}, t)$ denote the material and spatial velocity fields. The resultant force $\mathbf{F}(t)$ is comprised of the surface traction $\tilde{\boldsymbol{t}}$ acting over surface $\partial\mathcal{B}$ and body forces $\tilde{\boldsymbol{b}}$ that act on the volume element. Hence, the resultant force is given in the additive form

$$\mathbf{F}(t) = \int_{\partial\Omega_c} \tilde{\boldsymbol{t}}(\boldsymbol{x}, t)\, \mathrm{da} + \int_{\Omega_c} \tilde{\boldsymbol{b}}(\boldsymbol{x}, t)\, \mathrm{dv}. \tag{2.56}$$

The balance of the linear momentum combines the external force (2.56) and the principal (2.55) into one statement

$$\frac{D}{Dt} \int_{\Omega_c} \rho(\boldsymbol{x}, t) \boldsymbol{v}(\boldsymbol{x}, t)\, \mathrm{dv} = \int_{\partial\Omega_c} \tilde{\boldsymbol{t}}(\boldsymbol{x}, t)\, \mathrm{da} + \int_{\Omega_c} \tilde{\boldsymbol{b}}(\boldsymbol{x}, t)\, \mathrm{dv}. \tag{2.57}$$

For the sake of clarity in the subsequent equations the arguments of tensors, both first and second-order, are omitted. Utilizing the Cauchy stress theorem and divergence theorem

$$\iint_{\partial\Omega_c} \boldsymbol{\sigma}\boldsymbol{n}\, \mathrm{da} = \int_{\partial\Omega_c} \mathrm{div}(\boldsymbol{\sigma})\, \mathrm{dv} \tag{2.58}$$

the Cauchy's first equation of motion can be postulated as

$$\int_{\Omega_c} \big(\mathrm{div}(\boldsymbol{\sigma}) + \tilde{\boldsymbol{b}} - \rho\dot{\boldsymbol{v}}\big)\, \mathrm{dv} = 0, \tag{2.59}$$

where $\dot{\boldsymbol{v}} = \frac{D}{Dt}\boldsymbol{v}(\boldsymbol{x}, t)$. This relation should be met for any volume $d\mathrm{v}$, hence it can be written in the following local form

$$\mathrm{div}(\boldsymbol{\sigma}) + \tilde{\boldsymbol{b}} = \rho\dot{\boldsymbol{v}}. \tag{2.60}$$

2.4.3. Conservation of angular momentum

Principle of the balance of angular momentum states that rate of change of the total angular momentum is equal to the resultant moment of the forces acting on particles in body $\mathcal{B}$. Angular momentum defines the moment of the linear momentum relative to a fixed point in space, expressed as

$$\mathbf{J}(t) = \int_{\Omega_c} \mathbf{r} \times \big[\rho(\boldsymbol{x},t)\boldsymbol{v}(\boldsymbol{x},t)\big]\, d\mathrm{v} = \int_{\Omega_0} \mathbf{r} \times \big[\rho_0(\boldsymbol{X})\boldsymbol{V}(\boldsymbol{X},t)\big]\, d\mathrm{V}, \tag{2.61}$$

where $\mathbf{r}$ is a position vector. The time derivative of $\mathbf{J}$ defines the balance of the angular momentum as

$$\dot{\mathbf{J}}(t) = \frac{D}{Dt}\int_{\Omega_c} \mathbf{r} \times \big[\rho\, \boldsymbol{v}\big]\, d\mathrm{v} = \frac{D}{Dt}\int_{\Omega_0} \mathbf{r} \times \big[\rho_0\, \boldsymbol{V}\big]\, d\mathrm{V} = \mathbf{M}(t), \tag{2.62}$$

where $\mathbf{M}(t)$ is the resultant moment. Again, to improve the readability the arguments for the tensor objects were omitted. The additive form of $\mathbf{M}(t)$ resembles Eq. (2.56) apart from the cross product of the action $(\tilde{\boldsymbol{b}}, \tilde{\boldsymbol{t}})$ and the relative position of the particle $(\mathbf{r})$, i.e.

$$\mathbf{M}(t) = \int_{\partial\Omega_c} \mathbf{r} \times \tilde{\boldsymbol{t}}\, d\mathrm{a} + \int_{\Omega_c} \mathbf{r} \times \tilde{\boldsymbol{b}}\, d\mathrm{v}. \tag{2.63}$$

Finally, the global form of the balance of the angular momentum in the spatial description is obtained as

$$\frac{D}{Dt}\int_{\Omega_c} \mathbf{r} \times \big[\rho\, \boldsymbol{v}\big]\, d\mathrm{v} = \int_{\partial\Omega_c} \mathbf{r} \times \tilde{\boldsymbol{t}}\, d\mathrm{a} + \int_{\Omega_c} \mathbf{r} \times \tilde{\boldsymbol{b}}\, d\mathrm{v}. \tag{2.64}$$

The most curcial result, that stem from the balance of angular momentum, is the symmetry of the Cauchy stress tensor, i.e.

$$\boldsymbol{\sigma}^T = \boldsymbol{\sigma} \quad \text{or} \quad \sigma_{ab} = \sigma_{ba}. \tag{2.65}$$

2.4.4. Conservation of mechanical energy

The law of the conservation of mechanical energy is not a separate low; it is a reformulation of the equation of motion, which follows the principle of linear momentum.

First, the external mechanical power or the rate of external mechanical work P_{ext} is given by

$$\mathcal{P}_{ext}(t) = \int_{\partial\Omega_c} \tilde{\boldsymbol{t}} \cdot \boldsymbol{v}\, d\mathrm{a} + \int_{\Omega_c} \tilde{\boldsymbol{b}} \cdot \boldsymbol{v}\, d\mathrm{v}, \tag{2.66}$$

where the distinction between volume v and spatial velocity field $\boldsymbol{v}$ should be emphasized. Kinetic energy $\mathcal{K}$ derives from the classical definition of Newtonian kinetic

energy, via

$$\mathcal{K}(t) = \int_{\Omega_c} \frac{1}{2}\rho \boldsymbol{v}^2 d\mathrm{v} = \int_{\Omega_c} \rho \boldsymbol{v} \cdot \boldsymbol{v}\, d\mathrm{v}. \tag{2.67}$$

External forces acting on the body may also yield internal forces that act on internal deformations, thus carrying out work. Therefore, the rate of internal mechanical work or simply stress power and is defined by the scalar

$$\mathcal{P}_{int}(t) = \int_{\Omega_c} \boldsymbol{\sigma} : \boldsymbol{d}\, d\mathrm{v}. \tag{2.68}$$

Taken together, these quantities formulate law stating that power exerted by external forces changes the kinetic energy of the material and the reminder alter its internal energy. Thus, the balance of mechanical energy can be written in the form of

$$\frac{D}{Dt}\mathcal{K}(t) + \mathcal{P}_{int}(t) = \mathcal{P}_{ext}(t) \tag{2.69}$$

or

$$\frac{D}{Dt}\int_{\Omega_c} \frac{1}{2}\rho \boldsymbol{v}^2 d\mathrm{v} + \int_{\Omega_c} \boldsymbol{\sigma} : \boldsymbol{d}\, d\mathrm{v} = \int_{\partial\Omega_c} \tilde{\boldsymbol{t}} \cdot \boldsymbol{v}\, d\mathrm{a} + \int_{\Omega_c} \tilde{\boldsymbol{b}} \cdot \boldsymbol{v}\, d\mathrm{v}. \tag{2.70}$$

Next, the thermodynamic state variable $e_c = e_c(\boldsymbol{x}, t)$, defined in the current configuration, can be introduced. It is used to encompass various forms of energy in the inner volume element. So, the internal energy of body $\mathcal{B}$ can by specified as

$$\mathcal{E}(t) = \int_{\Omega_c} e_c\, d\mathrm{v}. \tag{2.71}$$

The assumption of purely mechanical deformation leads to the conclusion that the rate of work done by internal stresses ($\mathcal{P}_{int}$) is equal to the rate of internal energy, i.e.

$$\mathcal{P}_{int}(t) = \frac{D}{Dt}\mathcal{E}(t). \tag{2.72}$$

Finally, the balance of mechanical energy can be expressed in terms of the internal energy

$$\frac{D}{Dt}\mathcal{K}(t) + \frac{D}{Dt}\mathcal{E}(t) = \mathcal{P}_{ext}(t), \tag{2.73}$$

or, in the explicit notation

$$\frac{D}{Dt}\int_{\Omega_c} \left(\frac{1}{2}\rho \boldsymbol{v}^2 + e_c\right) d\mathrm{v} = \int_{\partial\Omega_c} \tilde{\boldsymbol{t}} \cdot \boldsymbol{v}\, d\mathrm{a} + \int_{\Omega_c} \tilde{\boldsymbol{b}} \cdot \boldsymbol{v}\, d\mathrm{v}. \tag{2.74}$$

2.4.5. First law of thermodynamics

A thermodynamic process is a process that considers thermal and mechanical forms of energy in its course. The first law of thermodynamics can be regarded as a statement of the interconvertibility of heat and work. The thermal power also referred to as the rate of thermal work is given by

$$\mathcal{Q}(t) = \int_{\partial\Omega_c} q_n \, \mathrm{da} + \int_{\Omega_c} r \, \mathrm{dv}, \tag{2.75}$$

where q_n denotes the scalar heat flux function and r denotes the internal heat sources. Both quantities determine heat per unit time and are calculated in terms of unit area and unit volume, respectively. The scalar function q_n is defined by the Stokes' heat flux theorem

$$q_n(\boldsymbol{x}, t, \boldsymbol{n}) = -\mathbf{q}(\boldsymbol{x}, t) \cdot \mathbf{n}, \tag{2.76}$$

where $\mathbf{q} = \mathbf{q}(\boldsymbol{x}, t)$ is a so-called Cauchy heat flux.

Thermal power is necessary to reformulate the rate of internal energy ($\mathcal{E}$) and expand it into the thermodynamic framework. The new form is as follows

$$\mathcal{P}_{int}(t) + \mathcal{Q}(t) = \frac{D}{Dt}\mathcal{E}(t). \tag{2.77}$$

Consequently, the first law of thermodynamics can be written in the form of identity

$$\frac{D}{Dt}\mathcal{K}(t) + \frac{D}{Dt}\mathcal{E}(t) = \mathcal{P}_{ext}(t) + \mathcal{Q}(t). \tag{2.78}$$

Substituting expressions for $\mathcal{K}$, $\mathcal{E}$, $\mathcal{P}_{ext}$ and $\mathcal{Q}$ from Eqs. (2.67), (2.71), (2.75) and (2.66) into the previous equation, a global form can be obtained

$$\frac{D}{Dt}\int_{\Omega_c} \left(\frac{1}{2}\rho \boldsymbol{v}^2 + e_c\right) \mathrm{dv} = \int_{\partial\Omega_c} \left(\tilde{\boldsymbol{t}} \cdot \boldsymbol{v} + q_n\right) \mathrm{da} + \int_{\Omega_c} \left(\tilde{\boldsymbol{b}} \cdot \boldsymbol{v} + r\right) \mathrm{dv}. \tag{2.79}$$

2.4.6. Second law of thermodynamics

The second law of thermodynamics derives from the physical observation that heat is transferred always from warmer to colder regions of material. In material modelling, it serves as an important mathematical restriction on the constitutive equations. For this law a concept of entropy has to be defined as a measure of disorder; physical interpretation of the entropy can be achieved in terms of statistical mechanics. The total entropy $\mathcal{S}(t)$ is a sum of the specific entropy $\eta_c = \eta_c(\boldsymbol{x}, t)$ in the current configuration, i.e.

$$\mathcal{S} = \int_{\Omega_c} \eta_c \, \mathrm{dv}. \tag{2.80}$$

The entropy input rate $\tilde{\mathcal{Q}}(t)$ depends on the vector field $\boldsymbol{h}$, denoting entropy flux defined per unit surface area and the scalar field $\tilde{r}$, denoting entropy sources per unit volume. $\tilde{\mathcal{Q}}(t)$ can be expressed in the following form

$$\tilde{\mathcal{Q}}(t) = \int_{\partial\Omega_c} \boldsymbol{h} \cdot \boldsymbol{n}\, \mathrm{da} + \int_{\Omega_c} \tilde{r}\, \mathrm{dv}. \tag{2.81}$$

The entropy flux is assumed to be positive when it enters the body and the normal vector is usually pointing in the outward direction, so the negative sign is used to designate the correct direction.

The total production of entropy is defined as the difference between the rate of change of the total entropy and the entropy input rate. The second law of thermodynamics postulates that this quantity is never negative, i.e.

$$\mathcal{G}(t) = \frac{D}{Dt} S - \tilde{\mathcal{Q}} \geqslant 0, \tag{2.82}$$

or, in the explicit notation

$$\int_{\Omega_c} \dot{\eta_c}\, \mathrm{dv} + \int_{\partial\Omega_c} \boldsymbol{h} \cdot \boldsymbol{n}\, \mathrm{da} - \int_{\Omega_c} \tilde{r}\, \mathrm{dv} \geqslant 0. \tag{2.83}$$

In classical thermodynamics, it is assumed that the entropy flux $\boldsymbol{h}$ and the entropy sources $\tilde{r}$ are related to the heat flux $\mathbf{q}$ and heat sources r in the following manner

$$\boldsymbol{h} = \frac{\mathbf{q}}{\theta} \quad \text{and} \quad \tilde{r} = \frac{r}{\theta}, \tag{2.84}$$

where θ is a scalar field known as absolute temperature. Therefore, utilizing Eq. (2.84) and the divergence theorem, the Clausius-Duhem inequality is achieved

$$\int_{\Omega_c} \left(\dot{\eta_c} + \operatorname{div}\left(\frac{\mathbf{q}}{\theta}\right) - \frac{r}{\theta} \right) \mathrm{dv} \geqslant 0. \tag{2.85}$$

2.5. Axioms of material modelling

Considering body $\mathcal{B}$ in the reference configuration and evoking a local form of previously stated equations, the following can be written:

balance of mass	(1)	$\dot{\rho} + \rho \operatorname{div}(\boldsymbol{v}) = 0,$	(2.86)
first equation of motion	(3)	$\operatorname{div}(\boldsymbol{\sigma}) + \tilde{\boldsymbol{b}} = \rho \dot{\boldsymbol{v}},$	(2.87)
geometric equations	(6)	$\boldsymbol{e} = \frac{1}{2}\left(\operatorname{grad}^T[\boldsymbol{u}] + \operatorname{grad}[\boldsymbol{u}]\right) + \frac{1}{2} \operatorname{grad}^T[\boldsymbol{u}] \operatorname{grad}[\boldsymbol{u}].$	(2.88)

Numbers in round brackets refer to the number of equations for each formula having regard to the symmetry of the strain tensor. Thus, the system of 10 equations has to be used to solve for 16 unknown basic fields, namely

density	(1)	ρ,
displacement	(3)	$\boldsymbol{u}$,
strain	(6)	$\boldsymbol{\varepsilon}$,
stress	(6)	$\boldsymbol{\sigma}$.

Since no information was given about properties of the material from which $\mathcal{B}$ was made, additional hypotheses have to be introduced to complete this system of equations. Constitutive equations bind the 6 components of stress tensor with 6 elements of the strain tensor, thus complementing the knowledge about the response of the particular material. The process of constructing constitutive relations usually depends to a large extent on the data from experiments that are used for fitting material parameters. Firstly, the general form of constitutive relation is assumed and then limited by referring to certain requirements and physical restrictions that were listed below:

a. **Principle of material indifference**. The constitutive equation must be invariant under changes of frame of reference. In other words, a material response is unequivocal and independent of the observer [209, 210].

b. **Principle of thermodynamically compatible determinism**. This principle states that the history of motion of a selected point in body and temperature field for the material is sufficient to determine the thermo-mechanical quantities for this point [208].

c. **Principle of consistency**. This axiom states that any constitutive model has to be in agreement with the conservation principles listed previously [210].

d. **Principle of equipresence**. This principle advises against the strong decoupling of variables describing different physical phenomena into separate classes. Rather, independent variables occurring in one constitutive equation should be present in all equations [210].

e. **Principle of material symmetry**. The constitutive model has to be consistent with all symmetries that are present in the material [33].

f. **Principle of local action**. State variables of the given material particle depend only on the deformation history of a small neighbourhood of that particle [209].

g. **Principle of fading memory**. Deformation that took place in the distant past should have less influence on the present state of material than those that occurred recently [209].

2.6. Finite element method – explicit scheme

The system of equations given in the previous section describes the general class of thermo-mechanical problems that can be solved by finding the displacement field. Analytical solutions rarely (if ever) exist, so an advanced numerical procedure has to be employed. Easy access to vast computational power encourages the use of approximate methods for obtaining an answer to initial boundary value problems (IBVP). No attempt is here made to provide a comprehensive overview of the subject. For a detailed account of the finite element method (FEM) and variational forms, a curious reader is referred to standard textbooks ([11, 32, 96, 223]). The version of the FEM presented in this treatise concerns the mechanics of elastic-viscoplastic materials and the infinitesimal strain theory.

2.6.1. Variational principle

Equations presented in section 2.4 and the boundary conditions establish a so-called strong from, valid for every point of $\mathcal{B}$. Conversely, a weak formulation enables finding a weaker class of functions, also known as test functions, which provide approximate solution of the previous system. The finite element method, which is based on variational formulation, expands the solution range to a broad spectrum of applications. Since no further assumptions, like existence of a potential, are made, the weak form is applicable to general problems like inelastic materials, friction, non-conservative loading, etc [95].

In this study, infinitesimal deformations are assumed which leads to the geometric linearization of strain tensors – cf. Eq. (2.31). Therefore, the Lagrangian and Eulerian descriptions are approximately the same since there is very little difference between material and spatial coordinates. Having that in mind, a lowercase notation will be used later in the text without reference to a specific frame of reference.

An elegant way to derive weak formulation is to consider the equation of motion in the global form (2.59) for a body $\mathcal{B}$ in configuration Ω. Following the index notation and applying $\dot{\boldsymbol{v}} = \ddot{\boldsymbol{u}}$, it can be expressed as

$$\int_{\Omega} \left(\sigma_{ij,j} + b_i - \rho \ddot{u}_i\right) \mathrm{d}v = 0, \tag{2.89}$$

where $\ddot{(\cdot)}$ is a common abbreviated notation of the second derivative with respect to time and the subscript comma $(.)_{,j}$ denotes the partial derivative with respect to x_j. Next, the foregoing equation is multiplied by a test function $\delta\boldsymbol{u}$ (has to fulfill the kinematic boundary conditions), which can be regarded as the virtual displacement field and integrated over the domain Ω currently occupied by the body:

$$\int_{\Omega} \delta u_i \left(\sigma_{ij,j} + b_i - \rho \ddot{u}_i\right) \mathrm{d}v = 0. \tag{2.90}$$

By applying the chain rule and rearranging the elements, the following is obtained

$$\delta u_i \, \sigma_{ij,j} = (\delta u_i \, \sigma_{ij})_{,j} - \delta u_{i,j} \, \sigma_{ij} \tag{2.91}$$

which leads to a different notation of Eq. (2.90), namely

$$\int_{\Omega} (\delta u_i \, \sigma_{ij})_{,j} \, \mathrm{dv} - \int_{\Omega} \left(\delta u_{i,j} \, \sigma_{ij} - \delta u_i \, b_i + \delta u_i \, \rho \ddot{u}_i \right) \mathrm{dv} = 0. \tag{2.92}$$

Applying the divergence theorem to the first integral and recognizing that the test function δu vanishes on the prescribed displacement boundary gives

$$\int_{\Omega} (\delta u_i \, \sigma_{ij})_{,j} \, \mathrm{dv} = \int_{\partial\Omega} \delta u_i \, \sigma_{ij} n_j \, \mathrm{da} = \int_{\partial\Omega} \delta u_i \, t_i \, \mathrm{da}, \tag{2.93}$$

yielding the following form

$$\int_{\partial\Omega} \delta u_i \, t_i \, \mathrm{da} + \int_{\Omega} \delta u_i \, b_i \, \mathrm{dv} - \int_{\Omega} \delta u_{i,j} \, \sigma_{ij} \, \mathrm{dv} - \int_{\Omega} \delta u_i \, \rho \ddot{u}_i \, \mathrm{dv} = 0. \tag{2.94}$$

Denoting the displacement gradient as $\delta \varepsilon_{ij}^{tr} = \delta u_{i,j}$ and rearranging elements render the virtual work principle as follows

$$\int_{\Omega} \delta \varepsilon_{ij}^{tr} \, \sigma_{ij} \, \mathrm{dv} + \int_{\Omega} \delta u_i \, \rho \ddot{u}_i \, \mathrm{dv} = \int_{\Omega} \delta u_i \, b_i \, \mathrm{dv} + \int_{\partial\Omega} \delta u_i \, t_i \, \mathrm{da}, \tag{2.95}$$

where $\delta \varepsilon^{tr}$ signifies supposition that the deformation was elastic in nature.

The boundary $\partial\Omega$ can be split into two parts where the traction $\partial\Omega_t$ and displacements $\partial\Omega_u$ are specified. By enforcing pointwise displacement boundary conditions and imposing constraint that δu_i vanishes on $\partial\Omega_u$ the final form can be obtained [223]

$$G^{eq} = \int_{\Omega} \delta \varepsilon_{ij}^{tr} \, \sigma_{ij} \, \mathrm{dv} + \int_{\Omega} \delta u_i \, \rho \ddot{u}_i \, \mathrm{dv} - \int_{\Omega} \delta u_i \, b_i \, \mathrm{dv} - \int_{\partial\Omega_t} \delta u_i \, t_i \, \mathrm{da} = 0 \tag{2.96}$$

where G^{eq} is direct Galerkin expression. The virtual work is a form of a Galerkin method which specifies that $G^{eq} = 0$.

This equilibrium can be also represented in the matrix form, which is very useful in carrying out algebraic manipulations or designing numerical procedures. In order to simplify mathematical notation, the second-order symmetric tensors were reduced to six-dimensional vectors according to Voigt's notation

$$\boldsymbol{\sigma} = (\sigma_{11} \quad \sigma_{22} \quad \sigma_{33} \quad \sigma_{23} \quad \sigma_{13} \quad \sigma_{12})^{\mathrm{T}} = (\sigma_1 \quad \sigma_2 \quad \sigma_3 \quad \sigma_4 \quad \sigma_5 \quad \sigma_6)^{\mathrm{T}}. \tag{2.97}$$

Thus, the $[3 \times 3]$ symmetric matrices are reduced to $[6 \times 1]$ vectors. Matrix notation yields the following result

$$G^{eq} = \int_{\Omega} \delta(\mathbb{B}\boldsymbol{u})^T \, \boldsymbol{\sigma} \, \mathrm{dv} + \int_{\Omega} \delta \boldsymbol{u}^T \, \rho \ddot{\boldsymbol{u}} \, \mathrm{dv} = \int_{\Omega} \delta \boldsymbol{u}^T \, \tilde{\boldsymbol{b}} \, \mathrm{dv} + \int_{\partial\Omega_t} \delta \boldsymbol{u}^T \, \tilde{\boldsymbol{t}} \, \mathrm{da}, \tag{2.98}$$

where $\mathbb{B}$ denotes three-dimensional matrix strain operator given by

$$\mathbb{B} = \begin{pmatrix} \frac{\partial}{\partial x_1} & 0 & 0 \\ 0 & \frac{\partial}{\partial x_2} & 0 \\ 0 & 0 & \frac{\partial}{\partial x_3} \\ 0 & \frac{\partial}{\partial x_3} & \frac{\partial}{\partial x_2} \\ \frac{\partial}{\partial x_3} & 0 & \frac{\partial}{\partial x_1} \\ \frac{\partial}{\partial x_2} & \frac{\partial}{\partial x_1} & 0 \end{pmatrix}. \tag{2.99}$$

2.6.2. Finite element approximation

The weak form (2.96) will be used to construct approximate solutions based on the finite element method. This leads to the Galerkin method which was extensively discussed in [57, 83, 224]. The finite approximation of the considered body in configuration Ω is denoted as $\hat{\Omega}$ and achieved by dividing it into elements Ω_e, such that

$$\Omega \approx \hat{\Omega} = \sum_e \Omega_e, \tag{2.100}$$

where the total number of subdomains is indicated by e. The boundary of the body is also subjected to a division

$$\partial\Omega \approx \partial\hat{\Omega} = \sum_e \partial\Omega_e = \sum_{et} \partial\Omega_{t_e} + \sum_{eu} \partial\Omega_{u_e}, \tag{2.101}$$

where $\partial\Omega_{t_e}$ denotes parts of boundary on which traction was applied and $\partial\Omega_{u_e}$ denotes segments on which displacements were applied. Now, the weak form of the motion equation can be written as a sum over the element domain. Therefore, the discretized version of Eq. (2.98) reads

$$\begin{aligned} G^{eq} \approx \hat{G}^{eq} = &\sum_e \left[\int_{\Omega_e} \delta(\mathbb{B}\boldsymbol{u})^T \boldsymbol{\sigma} \, \mathrm{dv} + \int_{\Omega_e} \delta\boldsymbol{u}^T \rho\ddot{\boldsymbol{u}} \, \mathrm{dv} - \int_{\Omega_e} \delta\boldsymbol{u}^T \tilde{\boldsymbol{b}} \, \mathrm{dv} \right] \\ &- \sum_{et} \left[\int_{\partial\Omega_{t_e}} \delta\boldsymbol{u}^T \tilde{\boldsymbol{t}} \, \mathrm{da} \right] = 0. \end{aligned} \tag{2.102}$$

The above can be further simplified to the following form

$$G^{eq} \approx \hat{G}^{eq} = \sum_e \hat{G}_e + \sum_{et} \hat{G}_{t_e}, \tag{2.103}$$

where $\hat{G}_e$ and $\hat{G}_{t_e}$ are specified for each element in their respective domains. For a Galerkin method, a solution is obtained by using approximations to the dependent

variables. Therefore, in regards to Eq. (2.102) approximations for $\boldsymbol{u}$ and the virtual form $\delta\boldsymbol{u}$ have to be found.

It should be noted that the additive split in Eq. (2.102) is possible when the highest derivatives in this equation are at least piecewise continuous [223]. These requirements ensure that all the integrals exist and no contributions across interelement boundaries are present. Solid mechanics problems generally contain only first derivatives, so approximation can be obtained with C^0 functions, i.e. functions that are continuous but do not necessarily have continuous first derivatives.

The time-dependent vector function for displacement approximation can be written as follows

$$\boldsymbol{u}(\boldsymbol{x},t) \approx \hat{\boldsymbol{u}}(\boldsymbol{x},t) = \sum_n \mathrm{N}_n(\boldsymbol{x})\bar{\boldsymbol{u}}_n(t) = \mathbf{N}(\boldsymbol{x})\bar{\boldsymbol{u}}(t), \tag{2.104}$$

where $\mathrm{N}_n(\boldsymbol{x})$ denotes the element shape functions, $\bar{\boldsymbol{u}}_n(t)$ time-dependent nodal displacements and sum index iterates over all n nodes associated with an element. The approximation of the virtual displacement field acquires the following form

$$\delta\boldsymbol{u}(\boldsymbol{x}) \approx \delta\hat{\boldsymbol{u}}(\boldsymbol{x}) = \sum_n \mathrm{N}_n(\boldsymbol{x})\delta\bar{\boldsymbol{u}}_n = \mathbf{N}(\boldsymbol{x})\delta\bar{\boldsymbol{u}}(t). \tag{2.105}$$

The above can be utilized to write the approximation for strains given by

$$\boldsymbol{\varepsilon} = \mathbb{B}\boldsymbol{u} \approx \sum_n (\mathbb{B}\mathrm{N}_n)\bar{\boldsymbol{u}}_n = \sum_n \mathbf{B}_n\bar{\boldsymbol{u}}_n = \mathbf{B}\bar{\boldsymbol{u}}, \tag{2.106}$$

where $\mathbf{B}_n$ is a three-dimensional shape function derivative matrix postulated at each node of an element and defined as

$$\mathbf{B}_n = \begin{pmatrix} \mathrm{N}_{n,x1} & 0 & 0 \\ 0 & \mathrm{N}_{n,x2} & 0 \\ 0 & 0 & \mathrm{N}_{n,x3} \\ 0 & \mathrm{N}_{n,x3} & \mathrm{N}_{n,x2} \\ \mathrm{N}_{n,x3} & 0 & \mathrm{N}_{n,x1} \\ \mathrm{N}_{n,x2} & \mathrm{N}_{n,x1} & 0 \end{pmatrix}. \tag{2.107}$$

The foregoing relations lead to weak formulation of the Eq. (2.102) postulated for an individual element

$$\begin{aligned} \hat{G_e^{eq}} = \delta\bar{\boldsymbol{u}}^T \Big[&\int_{\Omega_e} \mathbf{N}^T\rho\mathbf{N}\,\mathrm{dv}\,\ddot{\bar{\boldsymbol{u}}} + \int_{\Omega_e} \mathbf{B}^T\boldsymbol{\sigma}\,\mathrm{dv} - \int_{\Omega_e} \mathbf{N}^T\tilde{\boldsymbol{b}}\,\mathrm{dv} \\ &- \int_{\partial\Omega_{t_e}} \mathbf{N}^T\tilde{\boldsymbol{t}}\,\mathrm{da}\Big]. \end{aligned} \tag{2.108}$$

The components of the above equation can be specified as element arrays, such as

$$\begin{aligned}\hat{\mathbf{M}}_e &= \int_{\Omega_e} \mathbf{N}^T \rho \mathbf{N}\, d\mathrm{v},\\ \hat{\mathbf{P}}_e &= \int_{\Omega_e} \mathbf{B}^T \boldsymbol{\sigma}\, d\mathrm{v},\\ \hat{\mathbf{f}}_e &= \int_{\Omega_e} \mathbf{N}^T \tilde{\boldsymbol{b}}\, d\mathrm{v} + \int_{\partial\Omega_{t_e}} \mathbf{N}^T \tilde{\boldsymbol{t}}\, d\mathrm{a},\end{aligned} \tag{2.109}$$

which subsequently allows formulating general sums over all elements

$$\hat{\mathbf{M}} = \sum_e \hat{\mathbf{M}}_e, \quad \hat{\mathbf{P}} = \sum_e \hat{\mathbf{P}}_e \quad \text{and} \quad \hat{\mathbf{f}} = \sum_e \hat{\mathbf{f}}_e. \tag{2.110}$$

In the above, $\hat{\mathbf{M}}$ is called the mass matrix, $\hat{\mathbf{P}}$ is the stress divergence and $\hat{\mathbf{f}}$ denotes the specific load matrix.

Finally, a semi-discrete (only spatial discretization was conducted) problem given by the set of ordinary differential equations can be concisely defined in one equation, namely

$$\hat{\mathbf{M}}\ddot{\boldsymbol{u}} + \hat{\mathbf{P}} = \hat{\mathbf{f}}. \tag{2.111}$$

In general, integrals presented in this section can not be solved analytically and methods for obtaining a numerical approximation are required. Arguably, the most widely used is Gauss procedure which replaces the integral with the sum over the domain of the integrand evaluated at specific quadrature points multiplied by weighting factors [224].

2.6.3. Nonlinear transient problem – explicit scheme

An equilibrium given in Eq. (2.111) requires a discrete approximation in time of the displacement field to find its value at discrete time t_{n+1}. The aforementioned equation be can restated in a residual form as

$$\boldsymbol{\Psi}_{n+1} = \hat{\mathbf{f}}_{n+1} - \hat{\mathbf{M}}\ddot{\boldsymbol{u}}_{n+1} - \hat{\mathbf{P}}_{n+1} = 0, \tag{2.112}$$

where $\hat{\mathbf{P}}$ can be expressed only in terms of displacement, namely

$$\hat{\mathbf{P}}_{n+1} \equiv \int_{\Omega_e} \mathbf{B}^T \boldsymbol{\sigma}_{n+1}\, d\mathrm{v} = \hat{\mathbf{P}}(\boldsymbol{u}_{n+1}). \tag{2.113}$$

In principle, the solution of the transient problem can be found with any numerical integration scheme. However, for large tasks (a significant number of degrees of freedom) it requires numerical techniques that perform calculations efficiently. The Newmark

procedure [136] for solving the second-order ordinary differential equations is applied here. In its essence, the Newmark approach relates the discrete displacements, velocities and accelerations at t_{n+1} to those at t_n by the formulas

$$\begin{aligned}\boldsymbol{u}_{n+1} &= \boldsymbol{u}_n + \Delta t\, \boldsymbol{v}_n^{(u)} + \left(\frac{1}{2} - \beta'\right)\Delta t^2\, \boldsymbol{a}_n^{(u)} + \beta' \Delta t^2\, \boldsymbol{a}_{n+1}^{(u)} \\ &= \breve{\boldsymbol{u}}_{n+1} + \beta' \Delta t^2\, \boldsymbol{a}_{n+1}^{(u)},\end{aligned} \tag{2.114}$$

and

$$\begin{aligned}\boldsymbol{v}_{n+1}^{(u)} &= \boldsymbol{v}_n^{(u)} + (1-\gamma')\Delta t\, \boldsymbol{a}_n^{(u)} + \gamma' \Delta t\, \boldsymbol{a}_{n+1}^{(u)} \\ &= \breve{\boldsymbol{v}}_{n+1}^{(u)} + \gamma' \Delta t\, \boldsymbol{a}_{n+1}^{(u)},\end{aligned} \tag{2.115}$$

where $\Delta t = t_{n+1} - t_n$ and the approximation to the solution variables are as follows

$$\bar{\boldsymbol{u}}(t_{n+1}) \approx \boldsymbol{u}_{n+1},\ \dot{\bar{\boldsymbol{u}}}(t_{n+1}) \approx \boldsymbol{v}_{n+1}^{(u)},\ \text{and}\ \ddot{\bar{\boldsymbol{u}}}(t_{n+1}) \approx \boldsymbol{a}_{n+1}^{(u)}. \tag{2.116}$$

The values depending only on the solution at t_n are denoted as $\breve{\boldsymbol{u}}_{n+1}$, $\breve{\boldsymbol{v}}_{n+1}^{(u)}$. The stability and accuracy of the numerical scheme are controlled by two parameters γ' and β'. The result for the transient problem can be now obtained for each time t_{n+1} by solving the set of equations (2.112) and the pair of linear equations (2.116).

By setting $\beta' = 0$ and $\gamma' = 1/2$, the explicit Newmark method is obtained for solving the problem with respect to the $\boldsymbol{a}_{n+1}^{(u)}$ variable. The reduction of equation components makes the Newmark algorithm equivalent to the central difference method. It can be noticed that in Eq. (2.114) only the part dependent on the current state (t_n) remains, namely

$$\boldsymbol{u}_{n+1} = \breve{\boldsymbol{u}}_{n+1}. \tag{2.117}$$

Subsequently, the equations set can be written as

$$\hat{\mathbf{M}}\, \boldsymbol{a}_{n+1}^{(u)} = \hat{\mathbf{f}}_{n+1} - \hat{\mathbf{P}}(\breve{\boldsymbol{u}}). \tag{2.118}$$

In the above, the explicit nature of this scheme is evident since linear equations are solved. For a diagonal mass matrix $\hat{\mathbf{M}}$ problem becomes trivial since this matrix can be inverted, such that

$$\hat{\mathbf{M}}^{-1} = \begin{pmatrix} 1/M_{11} & & \\ & \ddots & \\ & & 1/M_{mm} \end{pmatrix}, \tag{2.119}$$

where m denotes the number of equations in the problem. The explicit method sacrifices unconditional stability for the reduction of numerical effort. Each step becomes less computationally intense, however, a significantly larger number of steps is required. The time step limitations are given by the following condition

$$\Delta t \leq \frac{2}{\omega_{max}^h}, \tag{2.120}$$

where ω^h_{max} denotes the highest frequency of the system. To avoid solving the eigenvalue problem for every time step the Courant–Friedrichs–Lewy stability condition can be adopted, such that

$$\Delta t \leq \frac{L_{e,min}}{c_d}, \tag{2.121}$$

where $L_{e,min}$ is the smallest element dimension in the mesh and c_d is the dilatational wave speed.

This method is valid for dynamic, high-strain-rate problems where the small-time increments and fine mesh allow to accurately capture the wave propagation in the material and ensure the stability of the solution. It is implemented in the Abaqus suite for finite element analysis under the name Abaqus\Explicit and was used in this treatise.

Chapter 3

Fractional stress-gradient thermo-viscoplasticity

3.1. Fractional calculus

In recent years fractional calculus has found use in various fields of science and engineering – some applications were presented in 1.2.5. This is due to the fact that fractional derivatives open a new dimension in the mathematical modelling, a fact which was extensively used in continuum mechanics. The non-locality introduced by this new approach changes the geometric and physical interpretation of the derivative as a local property. Therefore, extending models, in which it was used and making the original formulation a special case. The differential operator of non-integer order has two distinctive features: (a) can be defined in many ways and, (b) each formulation is defined on the interval or the half-axis [104]. The single point derivative is discarded in favour of a more general approach that utilizes n-fold integration or n-fold derivative. Among different approaches, the Caputo fractional derivative has been frequently implemented in solid mechanics because it provides easily interpretable initial conditions [160]. Moreover, the Caputo derivative of the constant function is zero, which is not a common property of all formulations [104].

As mentioned previously, the differential operator can be formulated in many different ways. In this work, the method with the generalized fractional operator K_P^α based on the kernel function was chosen. Following terse notation presented in [2] and [139], the operator K_P^α can be introduced in the following form

$$\left(K_P^\alpha f\right)(t) = p \int_a^t k_\alpha(t,\tau) f(\tau) d\tau + q \int_t^b k_\alpha(\tau,t) f(\tau) d\tau, \tag{3.1}$$

where $t \in \left[a, b\right]$ and $a < t < b$, p, q are real numbers, and $k_\alpha(t, \tau)$ is a kernel that depends on the order of the derivative α. Assuming that $k_\alpha(t, \tau)$ is a difference kernel

$$k_\alpha(t, \tau) = k_\alpha(t - \tau), \tag{3.2}$$

and

$$k_\alpha \in L_1\left([0, b - a]\right). \tag{3.3}$$

Then, K_P^α is defined as bounded and linear operator, i.e. $K_P^\alpha : L_1\left([a, b]\right) \to L_1\left([a, b]\right)$. Choosing the proper kernel, i.e.

$$k_\alpha(t - \tau) = \frac{1}{\Gamma(\alpha)}\left(t - \tau\right)^{\alpha - 1}, \tag{3.4}$$

where $\alpha > 0$, leads to the following integral formulas:

- for $P = \left\langle a, t, b, 1, 0\right\rangle$

$$\left(K_P^\alpha f\right)(t) = \frac{1}{\Gamma(\alpha)} \int_a^t (t - \tau)^{\alpha + 1} f(\tau) d\tau = \left({}_a I_t^\alpha f\right)(t), \tag{3.5}$$

- and for $P = \left\langle a, t, b, 0, 1\right\rangle$

$$\left(K_P^\alpha f\right)(t) = \frac{1}{\Gamma(\alpha)} \int_t^b (\tau - t)^{\alpha + 1} f(\tau) d\tau = \left({}_t I_b^\alpha f\right)(t), \tag{3.6}$$

where $\left({}_a I_t^\alpha f\right)(t)$ and $\left({}_t I_b^\alpha f\right)(t)$ denotes the left and right Riemann-Liouville fractional integrals, respectively and $\Gamma(\alpha)$ is the Gamma function.

Next, the general kernel differential operator of Caputo type B_P^α [117] can be defined as a composition of Riemann-Liouville fractional integral and classical n-th order ($n \in \mathbb{N}$) derivative with respect to time

$$B_P^\alpha = K_P^{n - \alpha} \circ \frac{d^n}{dt^n}, \tag{3.7}$$

where α is the order of the derivative, $n = \lfloor \alpha \rfloor + 1$ and $\lfloor \cdot \rfloor$ denotes the floor function. The B-operator is valid for functions $f \in AC^n([a, b])$, where $AC^n([a, b])$ denote a space of functions which are absolutely continuous on $[a, b]$ interval [92]. The left-sided and the right-sided Caputo derivatives are then defined as:

$$\left(B_P^\alpha f\right)(t) = \frac{1}{\Gamma(n - \alpha)} \int_a^t \frac{f^n(\tau)}{(t - \tau)^{\alpha - n - 1}} d\tau = {}_a^C D_t^\alpha f(t), \tag{3.8}$$

where $t > a$, and

$$-\left(B_P^{\alpha} f\right)(t) = -\frac{(-1)^n}{\Gamma(n-\alpha)} \int_t^b \frac{f^n(\tau)}{(\tau - t)^{\alpha - n - 1}} d\tau = {}^{C}_{t}D_b^{\alpha} f(t), \tag{3.9}$$

where $t < b$.

As pointed out in [160], the complete theory of fractional differential equations can be developed only with the use of the both left and right derivatives. In order to obtain an operator defined on a closed interval $[a, b]$, the Riesz symmetrized Caputo fractional derivative is used. The Riesz-Caputo (RC) fractional derivative is a two-sided fractional operator, defined as a linear combination of left-sided and right-sided Caputo derivatives in the following manner [55]:

$$D^{\alpha} f(t) = {}^{RC}_{a}D_b^{\alpha} f(t) = \frac{1}{2}\Big[{}^{C}_{a}D_t^{\alpha} f(t) + (-1)^n \, {}^{C}_{t}D_b^{\alpha} f(t)\Big]. \tag{3.10}$$

The RC fractional derivative is utilized in the next chapters of this treatise.

Finally, it should be noted that for α of integer order n ($n \in \mathbb{N}$), the classical derivative of order n is obtained.

Given the integral form of the fractional operator, it has to be accepted that only for a finite set of functions the closed-form solution of the indefinite integrals exists. Therefore, the numerical procedure for obtaining an approximate solution has to be introduced. The discrete approximation for Caputo derivative, based on [138, 191], reads:

- left-sided derivative

$$\begin{aligned} &a = t_0 < t_1 < \cdots < t_k < \cdots < t_{m_a} = t, \\ &h_a = \frac{t_{m_a - t_0}}{m_a} = \frac{t - a}{m_a}, \quad m_a \geq 2, \end{aligned} \tag{3.11}$$

$$\begin{aligned} {}^{C}_{a}D_t^{\alpha} f(t)|_{t=t_{m_a}} \cong \quad & \frac{h_a^{n-\alpha}}{\Gamma(n-\alpha+2)} \Big\{ \big[(m_a - 1)^{n-\alpha+1} \\ & - (m_a - n + \alpha - 1) m_a^{n-\alpha}\big] f^{(n)}(t_0) + f^{(n)}(t_{m_a}) \\ & + \sum_{k=1}^{m_a - 1} \big[(m_a - k + 1)^{n-\alpha+1} - 2(m_a - k)^{n-\alpha+1} \\ & + (m_a - k - 1)^{n-\alpha+1}\big] f^{(n)}(t_k) \Big\}, \end{aligned} \tag{3.12}$$

- right-sided derivative

$$\begin{aligned} &t = t_0 < t_1 < \cdots < t_k < \cdots < t_{m_a} = b \\ &h_b = \frac{t_{m_b - t_0}}{m_b} = \frac{b - t}{m_b}, \quad m_b \geq 2, \end{aligned} \tag{3.13}$$

$$
\begin{aligned}
{}^{C}_{t}D^{\alpha}_{b} f(t)|_{t=t_0} \cong \quad & \frac{(-1)^n\, h_b^{n-\alpha}}{\Gamma(n-\alpha+2)} \Big\{ \big[(m_a-1)^{n-\alpha+1} \\
& - (m_b - n + \alpha - 1) m_b^{n-\alpha} \big] f^{(n)}(t_{m_b}) + f^{(n)}(t_0) \\
& + \sum_{k=1}^{m_b-1} \big[(k+1)^{n-\alpha+1} - 2k^{n-\alpha+1} \\
& + (k-1)^{n-\alpha+1} \big] f^{(n)}(t_k) \Big\},
\end{aligned}
\tag{3.14}
$$

where $f^{(n)}(t_k)$ denotes the classical n-th order derivative at point $t = t_k$.
A detailed explanation and implementation of this approach was given in section 3.2.3.

3.2. Fractional viscoplastic flow rule

3.2.1. Perzyna's theory of viscoplasticity

Rate-dependent material models stem from experimental results suggesting that the velocity of deformation plays a significant role in describing the material response. In continuum mechanics, a theory that describes a rate-dependent inelastic behaviour of solid materials is known as viscoplasticity. Foundations of viscoplasticity were laid by Hohenemser and Prager in [78]. Further development and in-depth study was done by Perzyna in works [148], [149], [150] and [155].

In classical Perzyna's approach for small strain theory, an additive decomposition of total strain tensor ($\boldsymbol{\varepsilon}$) into the sum of elastic ($\boldsymbol{\varepsilon}^e$) and inelastic ($\boldsymbol{\varepsilon}^p$) components is one of the main assumptions [111]. Because of the rate-dependence in Perzyna's theory, inelastic components are refered to as the viscoplastic strain tensor and represented by ($\boldsymbol{\varepsilon}^{vp}$). Hence the decomposition has the following form

$$
\boldsymbol{\varepsilon} = \boldsymbol{\varepsilon}^e + \boldsymbol{\varepsilon}^{vp}, \tag{3.15}
$$

and the corresponding rate form reads

$$
\dot{\boldsymbol{\varepsilon}} = \dot{\boldsymbol{\varepsilon}}^e + \dot{\boldsymbol{\varepsilon}}^{vp}. \tag{3.16}
$$

Moreover, the stress is assumed to be related to the elastic strain by means of standard linear constitutive relation

$$
\boldsymbol{\sigma} = \mathcal{L}^e : \boldsymbol{\varepsilon}^e, \tag{3.17}
$$

where $\mathcal{L}^e$ denotes the 4th order tensor of elastic constants and ':' indicates double contraction of tensors. Static yield condition is no different than the initial yield condition in the inviscid plasticity and is given by

$$
F(\boldsymbol{\sigma}) = \frac{f(\boldsymbol{\sigma})}{\kappa} - 1, \tag{3.18}
$$

where $f(\boldsymbol{\sigma})$ is a shear yield function and κ denotes static yield stress in simple shear. It must be pointed out that in general, function f may also depend on the state variables, e.g. viscoplastic strain or temperature. Yield stress κ also may be a function of state variables but in Eq. (3.18) it is assumed to be constant.

The assertion that plastic flow may occur only when $F = 0$ translates into a surface in six-dimensional stress space that is assumed to be regular and convex. Therefore, a plastic flow rule can be proposed as [148]

$$\dot{\boldsymbol{\varepsilon}}^{vp} = \gamma_0 \big\langle \Phi\big(F\big) \big\rangle \frac{\partial F}{\partial \boldsymbol{\sigma}}, \tag{3.19}$$

or in different form

$$\dot{\boldsymbol{\varepsilon}}^{vp} = \gamma \big\langle \Phi\big(F\big) \big\rangle \frac{\partial f}{\partial \boldsymbol{\sigma}}, \tag{3.20}$$

where $\gamma = \gamma_0/\kappa$ is a viscosity-related parameter, $\Phi\big(F\big)$ denotes the function that reflects dynamic behaviour of metal under consideration and $\partial/\partial\boldsymbol{\sigma}$ notation represents classical partial derivative with respect to stress. Symbol $\langle . \rangle$ is used to represent Macaulay brackets

$$\big\langle \Phi\big(F\big) \big\rangle = \begin{cases} 0 & \Phi\big(F\big) \leq 0 \\ \Phi\big(F\big) & \Phi\big(F\big) > 0 \end{cases}. \tag{3.21}$$

Regardless of the form, the plastic flow rule reveals the supposition that the rate of increase of inelastic part of strain tensor depends on the excess stress over the static yield condition [149].

Among various yield criteria that have been suggested for metals, the Huber-Mises-Hencky [73, 81, 129] fits experimental data closely than others [77]. Therefore, the yield function is equal to

$$f(\boldsymbol{\sigma}) = (J_2')^{1/2}, \tag{3.22}$$

where $J_2' = (\boldsymbol{s} : \boldsymbol{s})/2$ represents the second invariant of the stress deviator $\boldsymbol{s}$. Plastic flow rule in terms of the deviatoric stress then has the form

$$\dot{\boldsymbol{\varepsilon}}^{vp} = \gamma \left\langle \Phi\left(\frac{\sqrt{J_2'}}{\kappa} - 1 \right) \right\rangle \frac{\boldsymbol{s}}{\sqrt{J_2'}}. \tag{3.23}$$

By squaring Eq. (3.20) and introducing the second invariant of an inelastic strain-rate tensor as $I_2^P = (\dot{\boldsymbol{\varepsilon}}^{vp} : \dot{\boldsymbol{\varepsilon}}^{vp})/2$ the following formula can be obtained

$$\sqrt{I_2^P} = \gamma\, \Phi\left(\frac{\sqrt{J_2'}}{\kappa} - 1 \right). \tag{3.24}$$

The above relation, when expressed in terms of I_2^P, assumes the form

$$\sqrt{J_2'} = \kappa \left[1 + \Phi^{-1}\left(\frac{\sqrt{I_2^P}}{\gamma} \right) \right]. \tag{3.25}$$

This is referred to as the dynamic yield condition for viscoplastic materials and implicitly provides a yield criterion that depends on the strain rate.

The above mentioned evolution equation (proposed by Naghdi and Murch in [134] and later developed by Perzyna [158]) can be written in a compact form

$$\dot{\boldsymbol{\varepsilon}}^{vp} = \Lambda\, \boldsymbol{p}, \tag{3.26}$$

where scalar multiplier Λ represents the intensity of viscoplastic flow and $\boldsymbol{p}$ is a normalized second-order tensor denoting the direction of the flow. The direction of viscoplastic flow considering static yield condition as in Eq. (3.18) and HMH criterion, is then given via

$$\boldsymbol{p} = \frac{\partial F}{\partial \boldsymbol{\sigma}} \left(\left\| \frac{\partial F}{\partial \boldsymbol{\sigma}} \right\| \right)^{-1} = \frac{\boldsymbol{s}}{\sqrt{J_2'}}. \tag{3.27}$$

Thus, in classical viscoplasticity is it assumed that $\boldsymbol{p}$ is perpendicular (normal) to the pressure-independent yield surface. This implies that viscoplastic strain increment has the same direction as $\boldsymbol{p}$; this is called associated flow rule and the assumption of co-directionality is called the normality condition.

The intensity of viscoplastic flow is governed by Λ and can be written as

$$\Lambda = \gamma \langle \Phi(F) \rangle. \tag{3.28}$$

Among different possibilities, the exponential form of the overstress function Φ was considered in [148] and [43] as

$$\Phi(F) = F^m = \left(\frac{\sqrt{J_2'}}{\kappa} - 1 \right)^m, \tag{3.29}$$

where m denotes the scalar parameter used to scale the rate-sensitivity of the model. Moreover, viscous properties can be expressed by the means of time relaxation of mechanical disturbances $T_m = 1/\gamma$. Finally, the application of (3.28) and (3.29) to (3.26) yields the expression

$$\Lambda = \frac{1}{T_m} \left\langle \frac{\sqrt{J_2'}}{\kappa} - 1 \right\rangle^m. \tag{3.30}$$

It is worth pointing out that relaxation time T_m is a contributing factor in the model sensitivity since it is included in the length-scale parameter l, via

$$l = \hat{\alpha}\, \hat{c}\, T_m, \tag{3.31}$$

where $\hat{c}$ denotes elastic wave propagation velocity and $\hat{\alpha}$ denotes a proportionality factor. Therefore, T_m interpretation is twofold: (i) as a microstructural parameter determined experimentally or (ii) as a mathematical regularization parameter [157, 186].

3.2.2. Fractional viscoplasticity – basic approach

The direction of viscoplastic flow (3.27) is obtained by calculating the first-order partial derivative with respect to stress components. By applying the fractional derivative instead of classical a general approach is introduced, where the order of the operator (α) can be changed. This formulation has also an important feature mentioned in chapter 3.1, namely that for $\alpha = 1$ the well-known Perzyna-type viscoplasticity (presented in 3.2.1) is obtained. The direction of viscoplastic flow is given by

$$\boldsymbol{p} = D^{\alpha} F \left\| D^{\alpha} F \right\|^{-1}, \tag{3.32}$$

where D^{α} stands for the Riesz-Caputo fractional operator – see Eq. (3.10). Thus, the rate of increase of inelastic (viscoplastic) part of strain tensor has the following form

$$\dot{\varepsilon}^{vp} = \Lambda \frac{D^{\alpha} F}{\left\| D^{\alpha} F \right\|} = \frac{1}{T_m} \left\langle \frac{\sqrt{J_2'}}{\kappa} - 1 \right\rangle^{m} \frac{D^{\alpha} F}{\left\| D^{\alpha} F \right\|}. \tag{3.33}$$

The viscoplastic flow direction (3.27) is expressed solely in terms of the stress deviator, which leads to the conclusion that a volume change can happen only in the elastic range. Previous studies [192, 200] have reported that volume increase can be controlled by inelastic material models that utilize fractional calculus. To achieve the foregoing result in classical plasticity theories a different potential has to be assumed in Eq. (3.27), which requires additional material parameters that have to be specified. Moreover, the change of the operator also results in a non-associate flow which is desirable, e.g. when granular or porous materials are regarded [186]. This section has reviewed these two features that enhance classical theory and transform it into a more flexible tool for modelling viscoplastic materials.

3.2.3. Implementation – VUMAT subroutine

In this chapter, the formulation and numerical implementation of a three-dimensional elastic-viscoplastic isotropic model generalized in the framework of fractional calculus is presented. The following approach is based on the explicit FEM analysis that is recommended for solving dynamic nonlinear problems. It follows the conventions imposed by Abaqus\Explicit interface for VUMAT user subroutines used to implement new material models.

By restating the strain tensor according to the Voigt's notation as

$$\boldsymbol{\varepsilon} = \begin{pmatrix} \varepsilon_{11} & \varepsilon_{22} & \varepsilon_{33} & \varepsilon_{23} & \varepsilon_{13} & \varepsilon_{12} \end{pmatrix}^{\mathrm{T}} = \begin{pmatrix} \varepsilon_1 & \varepsilon_2 & \varepsilon_3 & \varepsilon_4 & \varepsilon_5 & \varepsilon_6 \end{pmatrix}^{\mathrm{T}} \tag{3.34}$$

and recalling the form of stress tensor (2.97), Hooke's law (3.17) can be written as

$$\begin{Bmatrix} \sigma_1 \\ \sigma_2 \\ \sigma_3 \\ \sigma_4 \\ \sigma_5 \\ \sigma_5 \end{Bmatrix} = \begin{pmatrix} 2G+\lambda & \lambda & \lambda & 0 & 0 & 0 \\ \lambda & 2G+\lambda & \lambda & 0 & 0 & 0 \\ \lambda & \lambda & 2G+\lambda & 0 & 0 & 0 \\ 0 & 0 & 0 & G & 0 & 0 \\ 0 & 0 & 0 & 0 & G & 0 \\ 0 & 0 & 0 & 0 & 0 & G \end{pmatrix} \begin{Bmatrix} \varepsilon_1 \\ \varepsilon_2 \\ \varepsilon_3 \\ \varepsilon_4 \\ \varepsilon_5 \\ \varepsilon_6 \end{Bmatrix}, \tag{3.35}$$

where $G = E/2(1+\nu)$ and $\lambda = E\nu/(1+\nu)(1-2\nu)$ are elastic constants and E and ν denotes Young's modulus and Poisson's ratio, respectively. Elements in the strain tensor can be classified either as normal $(\varepsilon_{11}, \varepsilon_{22}, \varepsilon_{33})$ or shear $(\varepsilon_{23}, \varepsilon_{13}, \varepsilon_{12})$ strains. The viscoplastic flow rule (3.33) can be postulated in the incremental form

$$\Delta\boldsymbol{\varepsilon}^{vp} = \Delta\Lambda\, \boldsymbol{p}, \tag{3.36}$$

where $\boldsymbol{p}$ is expressed in the six-dimensional space

$$\boldsymbol{p} = (p_1 \quad p_2 \quad p_3 \quad p_4 \quad p_5 \quad p_6)^{\mathrm{T}}. \tag{3.37}$$

Having in mind the requirement bestowed by the fractional derivative in Eqs. (3.12) and (3.14), lower and upper bounds has to be set to fulfill the condition [190]

$$a_i < \sigma_i < b_i. \tag{3.38}$$

The aforementioned bounds can be expressed in terms of distance from a certain point in the stress space σ_i, which can be written in the form

$$a_i = \sigma_i - \Delta_i^L, \quad b_i = \sigma_i + \Delta_i^R, \tag{3.39}$$

where

$$\boldsymbol{\Delta}^L = \left(\Delta_1^L \quad \Delta_2^L \quad \Delta_3^L \quad \Delta_4^L \quad \Delta_5^L \quad \Delta_6^L\right)^T, \tag{3.40}$$

and

$$\boldsymbol{\Delta}^R = \left(\Delta_1^R \quad \Delta_2^R \quad \Delta_3^R \quad \Delta_4^R \quad \Delta_5^R \quad \Delta_6^R\right)^T \tag{3.41}$$

$\boldsymbol{\Delta}^L$ and $\boldsymbol{\Delta}^R$ are regarded as material parameters that introduce non-locality in the stress space. Therefore the existence of a virtual surrounding is assumed – cf. Fig 3.1. The superscripts $(\cdot)^L$ and $(\cdot)^R$ refer to the left and right Caputo derivatives, respectively. The local neighbourhood of a material point can be interpreted as a (homogenized) phenomenological measure of some instability [200]. With regards to metals, the foregoing may result from nucleation of dislocations [30, 161, 222], nucleation of voids [121] or grains breakup mechanism [82, 100, 181] (cf. review paper [124]).

In order to calculate the direction of viscoplastic flow, the bounds of the virtual surrounding $\boldsymbol{a}$ and $\boldsymbol{b}$ have to be established. By analogy with $\boldsymbol{p}$, the following can be written

$$\boldsymbol{a} = (a_1 \quad a_2 \quad a_3 \quad a_4 \quad a_5 \quad a_6)^{\mathrm{T}}, \tag{3.42}$$

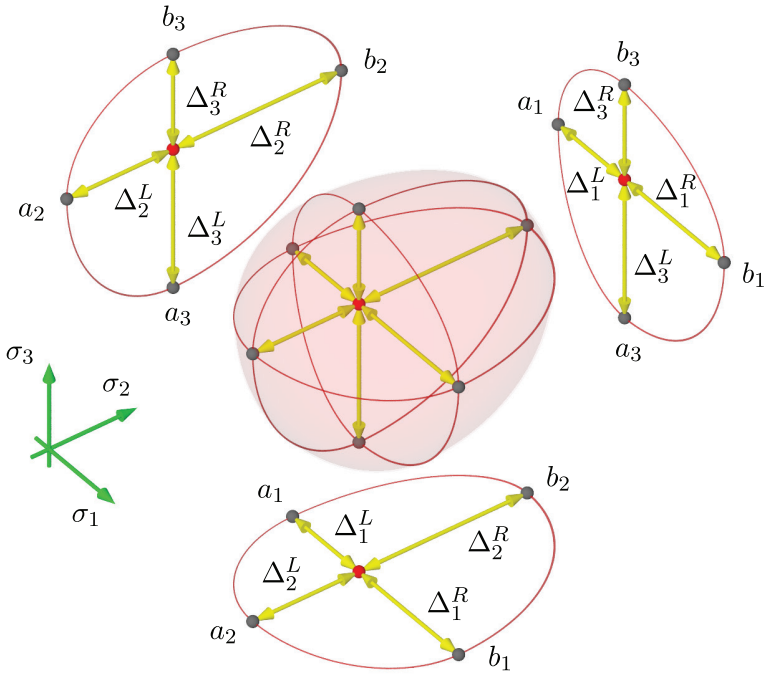

Figure 3.1. Virtual surrounding of a material point [191]

and

$$\boldsymbol{b} = (b_1 \quad b_2 \quad b_3 \quad b_4 \quad b_5 \quad b_6)^{\mathrm{T}}. \tag{3.43}$$

Each component of $\boldsymbol{\Delta}^L$ and $\boldsymbol{\Delta}^R$ is then subdivided into m_a and m_b discrete intervals with length

$$\boldsymbol{h}^a = \frac{1}{m_a}\boldsymbol{\Delta}^L = (h_1^a \quad h_2^a \quad h_3^a \quad h_4^a \quad h_5^a \quad h_6^a)^{\mathrm{T}}, \tag{3.44}$$

and

$$\boldsymbol{h}^b = \frac{1}{m_b}\boldsymbol{\Delta}^R = \left(h_1^b \quad h_2^b \quad h_3^b \quad h_4^b \quad h_5^b \quad h_6^b\right)^{\mathrm{T}}, \tag{3.45}$$

where $\boldsymbol{h}^a$ and $\boldsymbol{h}^a$ denote the spacing between points in the discretized stress space, and m_a and m_b denote the number of subintervals – cf. Fig. 3.2. In general, the distance between points and the number of subintervals is different for each component of $\boldsymbol{\Delta}^L$ and $\boldsymbol{\Delta}^R$. The total number of points in the numerical approximation is given by formula

$$n_p = (m_a - 1) + (m_b - 1) + 3. \tag{3.46}$$

In this treatise, it was assumed that $m_a = m_b = 2$.

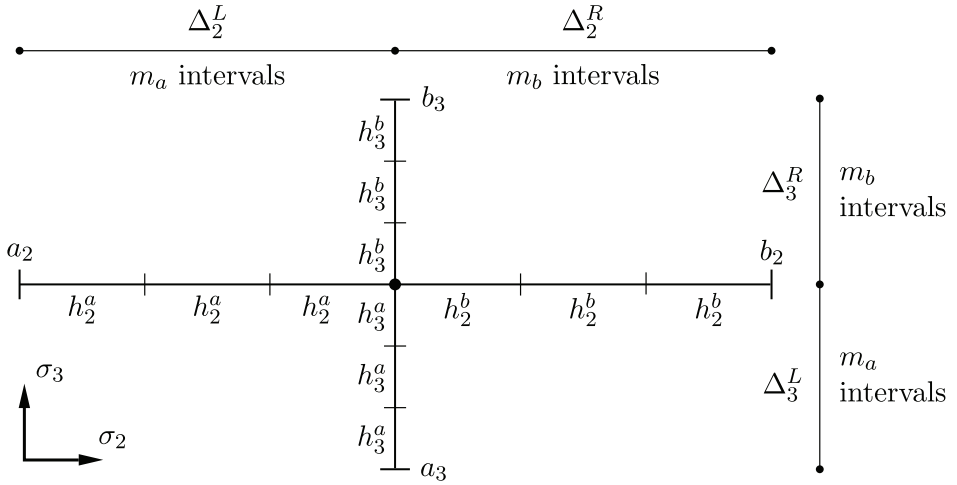

Figure 3.2. Discrete approximation of a non-local neighbourhood of a material point presented in a two-dimensional plane

The next step is to construct a $\boldsymbol{P}$ matrix containing coefficients from Eqs. (3.12) and (3.14), which has n_p rows and 6 columns. Matrix elements depend on the order of derivative α and the number of intervals, i.e. m_a and m_b. Thus, the elements of $\boldsymbol{P}$ can be obtained at the beginning of calculations without a need to be reevaluated further in the process, by following this definitions:

- for $i = 1$

$$P_{ij} = \frac{1}{2}\Gamma_j^a \left[(m_a - 1)^{n-\alpha+1} - (m_a - n + \alpha - 1)\, m_a^{n-\alpha}\right], \tag{3.47}$$

- for $i = (2, 3, \ldots, m_a)$

$$P_{ij} = \frac{1}{2}\Gamma_j^a \left[(m_a - j + 1)^{n-\alpha+1} - 2(m_a - j)^{n-\alpha+1} - (m_a - j - 1)^{n-\alpha+1}\right], \tag{3.48}$$

- for $i = m_a + 1$

$$P_{ij} = \frac{1}{2}\left(\Gamma_j^a + (-1)^n \Gamma_j^b\right), \tag{3.49}$$

- for $i = (m_a + 2, m_a + 3, \ldots, n_p - 1)$

$$P_{ij} = \frac{(-1)^n}{2}\Gamma_j^b \left[(j + 1)^{n-\alpha+1} - 2j^{n-\alpha+1} - (j - 1)^{n-\alpha+1}\right], \tag{3.50}$$

- for $i = n_p$

$$P_{ij} = \frac{(-1)^n}{2}\Gamma_j^b \left[(m_b - 1)^{n-\alpha+1} - (m_b - n + \alpha - 1)(m_b)^{n-\alpha}\right], \tag{3.51}$$

where

$$\Gamma_j^a = \frac{1}{\Gamma\left(n-\alpha+2\right)}\left(h_j^a\right)^{n-\alpha}, \tag{3.52}$$

$$\Gamma_j^b = \frac{1}{\Gamma\left(n-\alpha+2\right)}\left(h_j^b\right)^{n-\alpha}. \tag{3.53}$$

The second element necessary to determine the direction $\boldsymbol{p}$ is a matrix $\boldsymbol{Z}$ comprised of stress states in the neighbourhood of the material point. It has the same size as matrix $\boldsymbol{P}$, i.e. n_p rows and 6 columns. The definition of $\boldsymbol{Z}$ is given in the following form:

- for $i = 1$

$$Z_{ij} = \sigma_j - a_j, \tag{3.54}$$

- for $i = (2, 3, \ldots, m_a)$

$$Z_{ij} = \sigma_j - a_j + ih_j^a, \tag{3.55}$$

- for $i = m_a + 1$

$$Z_{ij} = \sigma_j, \tag{3.56}$$

- for $i = (m_a + 2, m_a + 3, \ldots, n_p - 1)$

$$Z_{ij} = \sigma_j + ih_j^b, \tag{3.57}$$

- for $i = n_p$

$$Z_{ij} = \sigma_j + b_j. \tag{3.58}$$

The final formula for the direction of viscoplastic flow is given by

$$p_i = P_{ij}M_{ij}, \tag{3.59}$$

where

$$M_{ij} = \frac{\partial F}{\partial \sigma_j}\Big|_{\sigma_j = Z_{ij}}, \tag{3.60}$$

for $i = (1, 2, \ldots, n_p)$, $j = (1, 2, \ldots, 6)$. The components of the matrix $\boldsymbol{M}$ are first-order partial derivatives of the static yield condition evaluated at subsequent values of $\boldsymbol{Z}$. It is worth noting that the accuracy of the solution can be improved by increasing the number of points of the approximation. However, large values of m_a and m_b will result in longer computations, so should be chosen reasonably. The sensitivity of the solution as a function of these parameters was studied in [191].

As mentioned before, based on the numerical formulation of fractional viscoplasticity, the VUMAT subroutine was created. The corresponding numerical algorithm was summarized in Fig. 3.3, highlighting the essential steps involved in the actual numerical implementation. Given the strain-space formulation [177], the VUMAT procedure aims at calculating and updating values of the Cauchy stress and internal variables, at

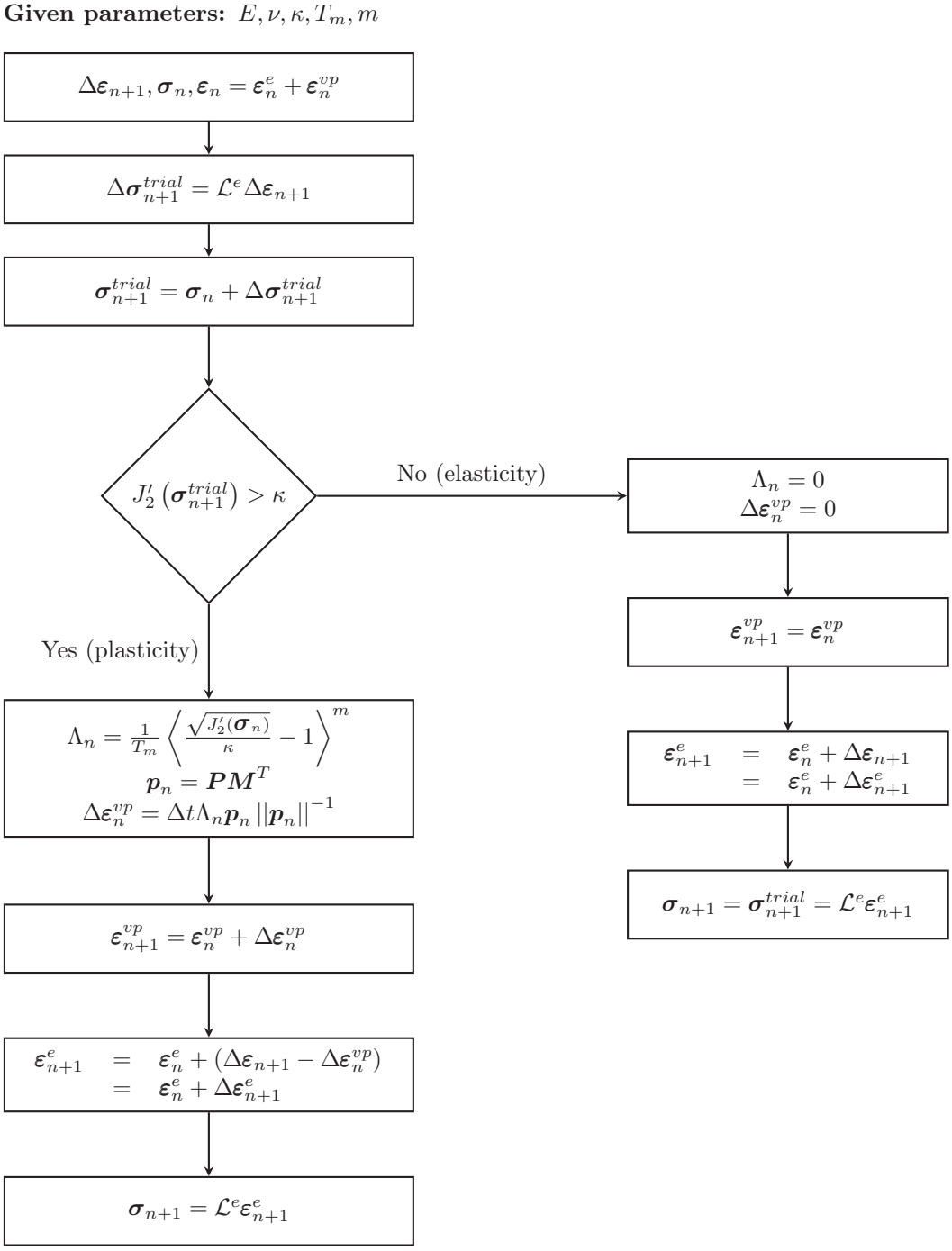

Figure 3.3. VUMAT subroutine flowchart for the fractional viscoplastic rule

time step t_{n+1}, based on the values from the previous time frame t_n and total strain increment $\Delta\boldsymbol{\varepsilon}_{n+1}$. The following notation is adopted

$$\Delta(\cdot) \equiv (\cdot)_{n+1} - (\cdot)_n, \tag{3.61}$$

where $(\cdot)_n$ and $(\cdot)_{n+1}$ denote the value of $(\cdot)$ respectively at t_n and t_{n+1} [33]. Moreover, notations $\boldsymbol{\varepsilon}(t_{n+1})$ and $\boldsymbol{\varepsilon}_{n+1}$, are equivalent, i.e. $\boldsymbol{\varepsilon}(t_{n+1}) = \boldsymbol{\varepsilon}_{n+1}$. At the onset, the trial stress tensor is obtained and used to check the yield condition. If the condition is fulfilled, the value of the plastic multiplier Λ and the direction $\boldsymbol{p}$ are calculated; otherwise, the elastic part of the procedure is executed. A similar flowchart was presented in [200], except that it was based on analytical solution for the Riesz-Caputo derivative.

3.3. Benchmark tests – the cube-shaped volume element under tension load

The aim of this section is to conduct a parametric investigation of the fractional viscoplastic model at the material point level. Therefore, the unit cube (1 mm × 1 mm × 1 mm) was modeled and discretized by a single finite element C3D8R (linear, eight-node brick with reduced integration). The conditions of a uniaxial tension test were obtained by applying boundary conditions as in Fig. 3.4. Material parameters were selected to represent a generic metallic material, thus $E = 205$ GPa, $\nu = 0.27$ and $\kappa = 605$ MPa. In what follows, the attention is focused on parameters that come from the fractional approach as well as the viscoplastic formulation, namely:

- α – order of the derivative,
- $\boldsymbol{\Delta}^L$ – left-sided stress-fractional spread,
- $\boldsymbol{\Delta}^R$ – right-sided stress-fractional spread,
- T_m – relaxation time,
- m – rate-sensitivity parameter.

To explicitly indicate the direction to which $\boldsymbol{\Delta}$ parameter is referring, the notation of the second rank tensor with two indices is more useful than a notation that uses one. So the following can be written

$$\boldsymbol{\Delta}^L = \begin{pmatrix} \Delta_1^L & \Delta_2^L & \Delta_3^L & \Delta_4^L & \Delta_5^L & \Delta_6^L \end{pmatrix}^T \equiv \begin{pmatrix} \Delta_{11}^L & \Delta_{22}^L & \Delta_{33}^L & \Delta_{23}^L & \Delta_{13}^L & \Delta_{12}^L \end{pmatrix}^T, \tag{3.62}$$

and

$$\boldsymbol{\Delta}^R = \begin{pmatrix} \Delta_1^R & \Delta_2^R & \Delta_3^R & \Delta_4^R & \Delta_5^R & \Delta_6^R \end{pmatrix}^T \equiv \begin{pmatrix} \Delta_{11}^R & \Delta_{22}^R & \Delta_{33}^R & \Delta_{23}^R & \Delta_{13}^R & \Delta_{12}^R \end{pmatrix}^T. \tag{3.63}$$

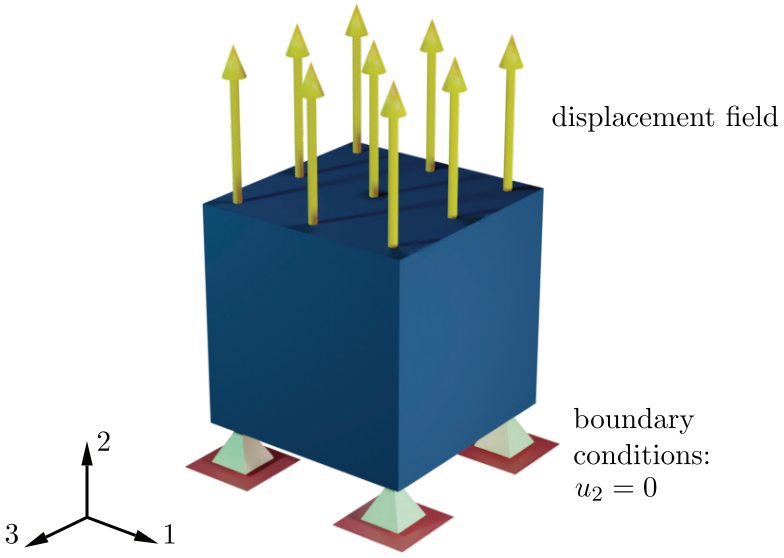

Figure 3.4. Model of a cube restricted to uniaxial tension

In this treatise, it was assumed that the values of the left-sided and right-sided $\boldsymbol{\Delta}$ vectors are equal, i.e. $\boldsymbol{\Delta}^L = \boldsymbol{\Delta}^R$. Therefore, the superscripts $(\cdot)^L$ and $(\cdot)^R$ are omitted further in the text.

In order to properly isolate and examine the influence of the aforementioned parameters, the numerical analysis were separated into two groups. The first one is concerned only with parameters that come from the fractional operator, i.e. the order of the derivative (α) and the $\boldsymbol{\Delta}$ parameter. The second group is concerned with the study of quantities that govern the viscoplastic flow – relaxation time (T_m) and rate-sensitivity parameter (m). The results presented in this chapter have been published in [200].

3.3.1. Study of the influence of the fractional parameters

Two types of plots were used to study the influence of $\boldsymbol{\Delta}$ and α on the dynamic response of the fractional viscoplastic model. The material anisotropy manifests itself in the directionally dependent evolution of deformation and can be observed on the charts that highlight the relation between normal strains $\varepsilon_{11}, \varepsilon_{22}, \varepsilon_{33}$. The dynamic behaviour is best depicted on a stress-strain relation, in this particular case the tension direction (2) was selected for in-depth study. Numerical analyses were conducted for two displacement velocities $v = 1$ and $v = 25$ m/s, and the set $\alpha \in \{0.1, 0.25, 0.5, 0.75, 0.99, 1.0\}$. The material parameters $T_m = 2.5\text{e}{-6}$ s and $m = 1$ were assumed after [184].

Based on the previous studies [190] the anisotropic behaviour of the fractional model was to be expected. The foregoing effect can be observed when one of the

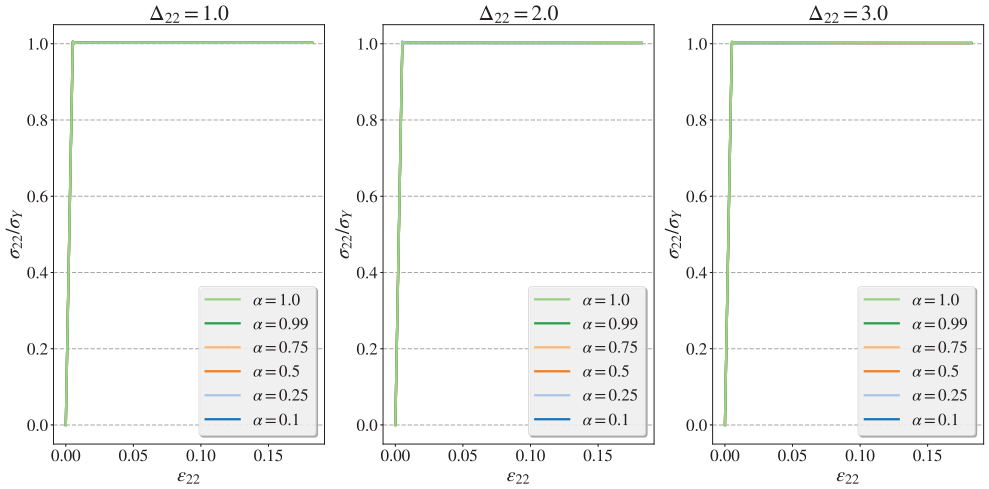

Figure 3.5. Influence of the order α and the value of material parameter Δ_{22} on the stress-strain relation, constant parameters: $v = 1$ m/s, $T_m = 2.5\text{e}{-6}$ s, $m = 1$ [200]

components of the vector $\boldsymbol{\Delta}$ is different than others. Hence, the two cases were chosen to study: for the direction of applied tension, $\Delta_{22} = 0.005\kappa \approx 3.0$ MPa and the direction perpendicular to the tension, $\Delta_{11} = 0.005\kappa \approx 3.0$ MPa. The intermediate value $\Delta = 0.0033\kappa \approx 2.0$ MPa was also analyzed to capture the development of the anisotropy in the material. The other values remained equal to $0.0017\kappa \approx 1.0$ MPa.

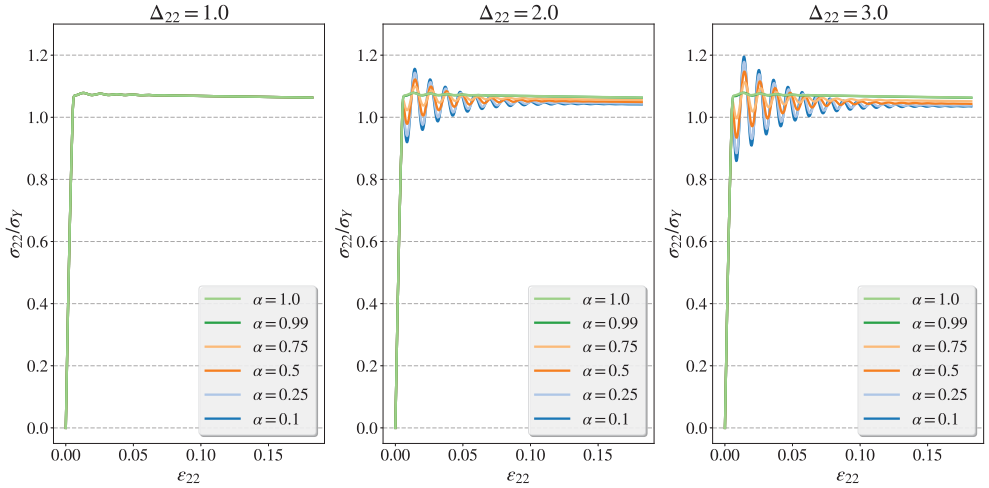

Figure 3.6. Influence of the order α and the value of material parameter Δ_{22} on the stress-strain relation, constant parameters: $v = 25$ m/s, $T_m = 2.5\text{e}{-6}$ s, $m = 1$ [200]

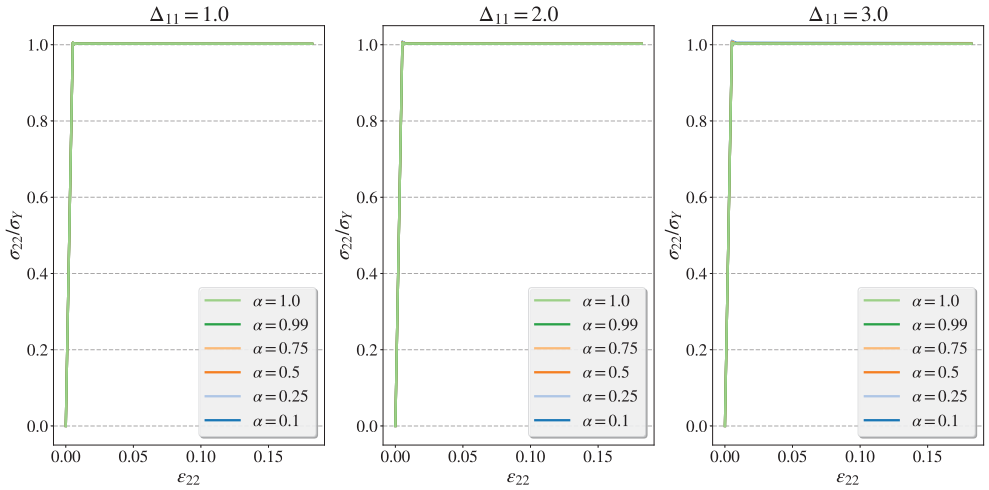

Figure 3.7. Influence of the order α and the value of material parameter Δ_{11} on the stress-strain relation, constant parameters: $v = 1$ m/s, $T_m = 2.5\text{e}{-6}$ s, $m = 1$ [200]

Fractional parameters in the (2) direction

Fig. 3.5 presents material behaviour under various values of α for the velocity $v = 1$ m/s. In general, changing α and $\boldsymbol{\Delta}$ modifies the dynamic properties, but the velocity applied in this case was insufficient to reveal it. For $v = 25$ m/s, depicted in Fig. 3.6, a waveform is forming already for $\Delta_{22} = 1.0$, and for larger values, it gets more pronounced. The amplitude of the stress wave increases with the increasing value of $\boldsymbol{\Delta}$. Conversely, it also grows when the value of α is decreasing. Is also should be pointed out that a slope can be observed in Fig. 3.6, particularly visible for $\Delta_{22} = 1.0$. Since this is a perfectly viscoplastic model ($\kappa = const$), this effect is not caused by the softening of the material, rather it is due to lateral stresses induced by the inertia effects.

Fractional parameters in the (1) direction

The sole difference between the parameters set examined in this section and the one studied in the previous section lays in the direction of the $\boldsymbol{\Delta}$. Here, the effects of the different values of Δ_{11} were investigated – it is a direction perpendicular to the applied load. Similarly to the preceding case, the velocity $v = 1$ m/s was too small for the Δ and α to have any effect on the stress-strain relation – Fig. 3.7. However, the relation between normal strains depicted in Fig. 3.8, strongly depends on the values of Δ and α. Since the value of Δ_{11} increases in the direction (1), which is perpendicular to the direction of applied load, it is expected that it will affect the corresponding strain,

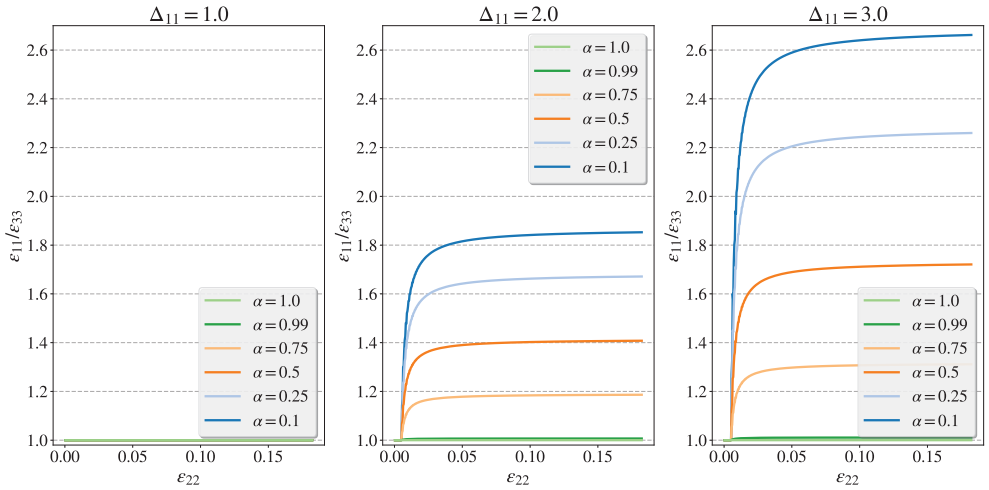

Figure 3.8. Influence of the order α and the value of material parameter Δ_{11} on the relation between three normal strains, constant parameters: $v = 1$ m/s, $T_m = 2.5\text{e}{-6}$ s, $m = 1$ [200]

namely ε_{11}. It can be concluded that material deform more easily in the (1) direction, thus $\varepsilon_{11}/\varepsilon_{33}$ ratio is greater than 1. This effect grows proportionally to the value of Δ and inversely to the value of α.

Next, the case for $v = 25$ m/s was considered. Fig. 3.9 shows that, besides the already discussed impact of $\boldsymbol{\Delta}$ and α on the stress wave, material hardening dependent on the order of the fractional operator can be observed. Also, the amplitude oscillations become more pronounced as the α diminishes to zero. The effects observed in Fig. 3.10 are very similar to those in Fig. 3.8, with the difference that a wave pattern is visible as a result of increased velocity.

3.3.2. Study of the material parameters of the viscoplastic models

This section aims to investigate the influence of the relaxation time T_m and the rate-sensitivity parameter m on the dynamic response of the fractional model. Similarly to section 3.3.1, two types of charts were used. Two directions, parallel and perpendicular to the applied load, were here also analyzed although only for one value of $\boldsymbol{\Delta}$. In order to compare classical viscoplasticity to its fractional counterpart each set of parameters was examined for $\alpha = 1$, indicated by the star symbol $(*)$ on charts. Also, to illustrate the full range of dynamic behaviours three velocities were used, namely $v = 1$, 25 and 50 m/s.

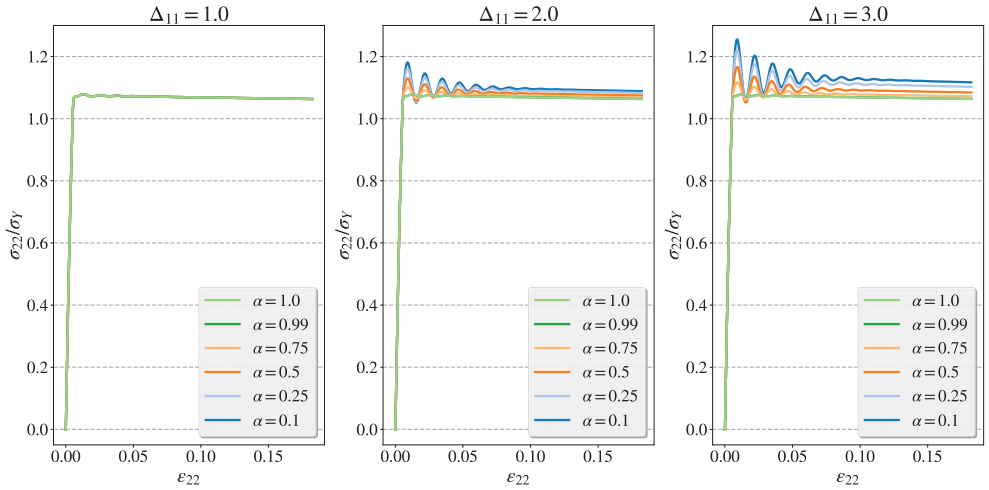

Figure 3.9. Influence of the order α and the value of material parameter Δ_{11} on the stress-strain relation, constant parameters: $v = 25$ m/s, $T_m = 2.5\text{e}{-6}$ s, $m = 1$ [200]

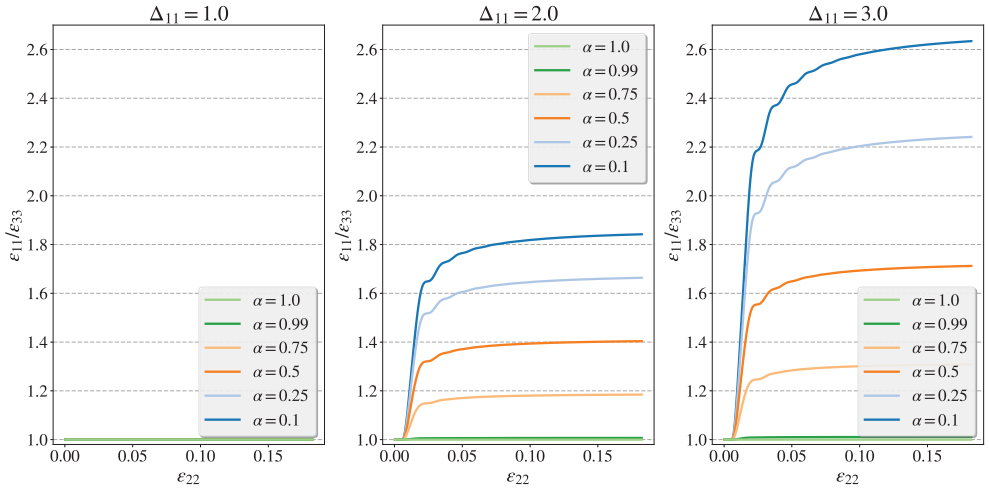

Figure 3.10. Influence of the order α and the value of material parameter Δ_{11} on the relation between three normal strains, constant parameters: $v = 25$ m/s, $T_m = 2.5\text{e}{-6}$ s, $m = 1$ [200]

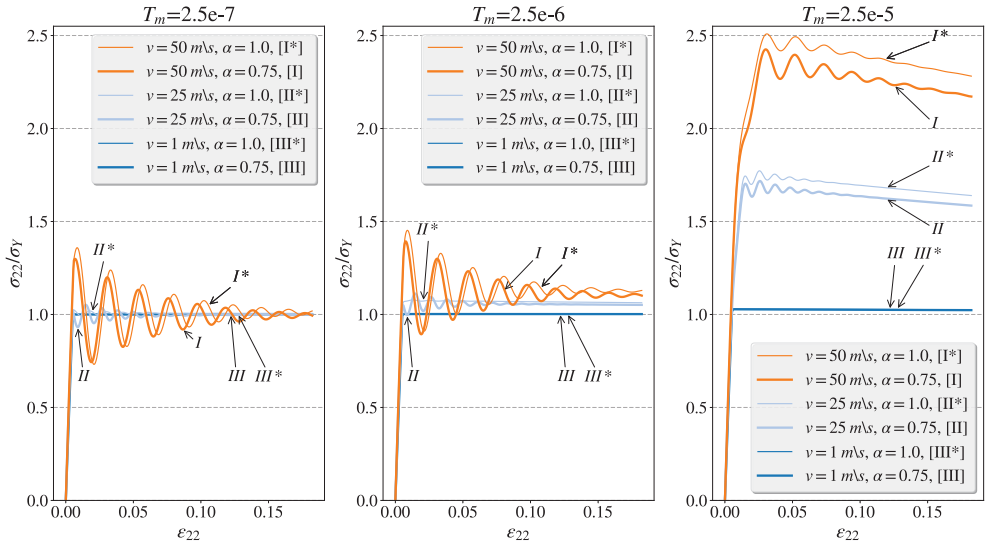

Figure 3.11. Influence of the relaxation parameter T_m and the value of applied velocity field v on the stress-strain relation, constant parameters: $\alpha = 0.75$, $m = 1$, $\Delta_{22} = 3.0$ [200]

Fractional parameters in the (2) direction

Here, the viscoplastic flow is induced in the direction of applied load by $\Delta_{22} = 3.0$ MPa. In Fig. 3.11 the effects of different relaxation times were captured. Material hardening can be observed with the increase of T_m, as well as the decrease in the amplitude of oscillations. For $T_m = 2.5\text{e}{-5}$ s, the separation between classical and fractional models is also significantly greater, than for other values.

Fig. 3.12 shows the consequences of the different values of m. It can be noticed that the grow of m is correlated with a decrease of oscillations and an increase in the stress levels. The strain-rate hardening, observed in Fig. 3.11 and 3.12, derive from the viscoplastic formulation. Also, on both charts, the stress-strain relations for $\alpha = 0.75$ produces lower stress levels when compared to the classical solution.

Fractional parameters in the (1) direction

In this section, the intensified viscoplastic flow was induced in the direction perpendicular to the displacement field ($\Delta_{11} = 3.0$ MPa). Fig. 3.13 presents the effect of the various values of T_m similar to what could be observed in the previous section, namely the increase of the relaxation time is reflected in the hardening of the material. The $\varepsilon_{11}/\varepsilon_{33}$ ratio in Fig. 3.14 reveals the anisotropic character of deformation for $\alpha = 0.75$, whereas for $\alpha = 1$ material exhibits isotropic behavior. The rate-sensitivity parameter m holds true to its name, as shown in Fig. 3.15, since its change has a direct effect

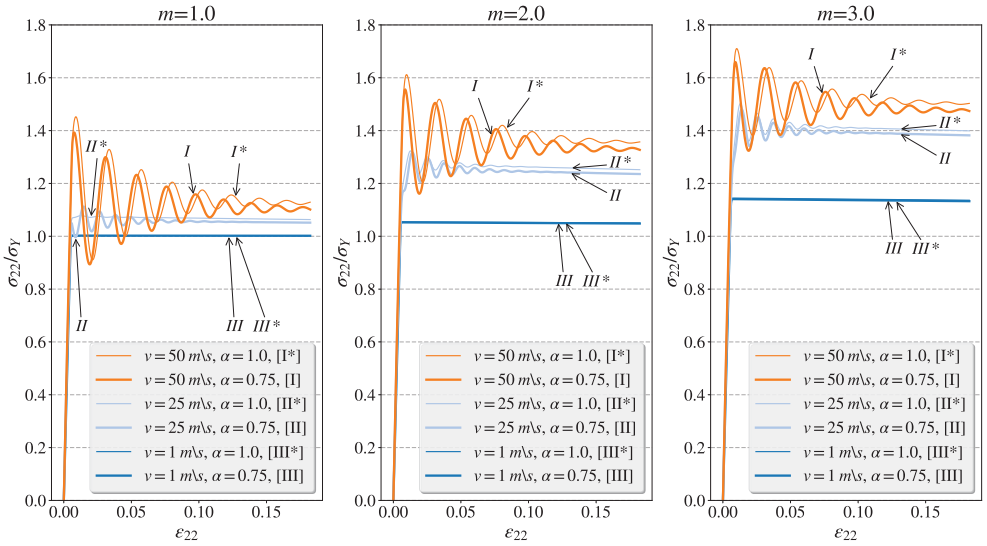

Figure 3.12. Influence of the material parameter m and the value of applied velocity field v on the stress-strain relation, constant parameters: $\alpha = 0.75$, $T_m = 2.5\text{e}{-6}$ s, $\Delta_{22} = 3.0$ [200]

on the stress level, without any apparent change to the frequency of oscillations. By increasing the value of m in Fig. 3.16, the wave pattern becomes more pronounced, especially for lower velocities. Moreover, the stress levels, depicted in Fig. 3.13 and 3.15, are generally greater for $\alpha = 0.75$ then for standard viscoplasticity ($\alpha = 1.0$). This result is distinctly different from what could be observed for the case where parameters were chosen to ensure the viscoplastic flow along the load direction, i.e. (2) direction – cf. Fig. 3.11 and 3.12. Thus, it suggests that the fractional approach also describes a degree of anisotropy observed in the inelastic dispersion of the stress wave.

3.3.3. Study of the dispersive nature of the fractional viscoplastic model

As was shown in the previous section, the introduction of fractional parameters induces directional dependence in the energy dispersion of the stress wave. The aim of this section is to verify if this type of anisotropy occurs when the frequency of a wave is considered. The measure of the regularity was obtained by calculating the average distance between peaks, which yields a period of oscillation later translated into wave frequency. In Tab. 3.1 results for two values of material parameter $\boldsymbol{\Delta}$ were shown; these results were depicted in the middle graphs of Figs. 3.11 and 3.13. The foregoing corresponds to cases where the viscoplastic flow is induced in the direction parallel (2) and perpendicular (1) to the applied velocity. As predicted, for $\alpha = 1$ classical

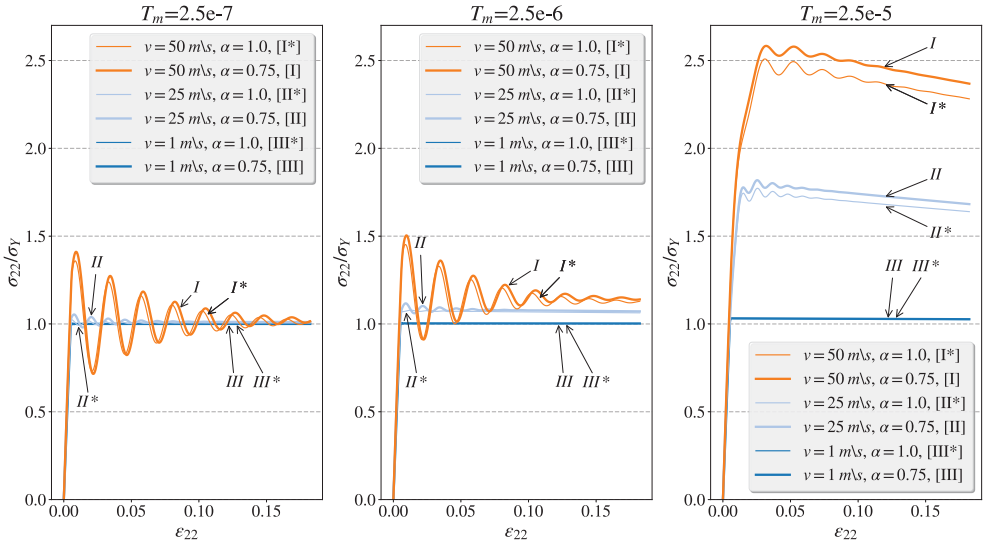

Figure 3.13. Influence of the relaxation parameter T_m and the value of applied velocity field v on the stress-strain relation, constant parameters: $\alpha = 0.75$, $m = 1$, $\Delta_{11} = 3.0$ [200]

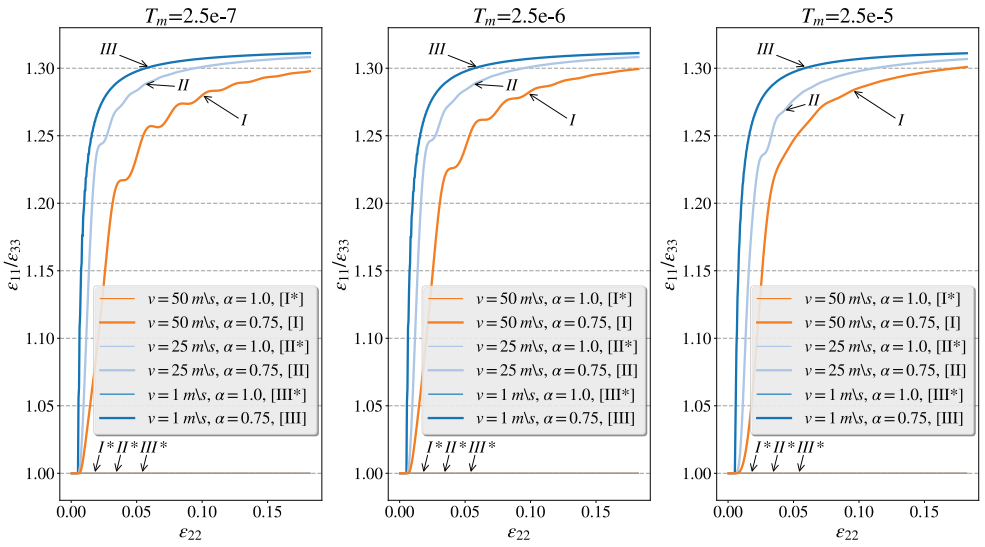

Figure 3.14. Influence of the relaxation parameter T_m and the value of applied velocity field v on the relation between three normal strains, constant parameters: $\alpha = 0.75$, $m = 1$, $\Delta_{11} = 3.0$ [200]

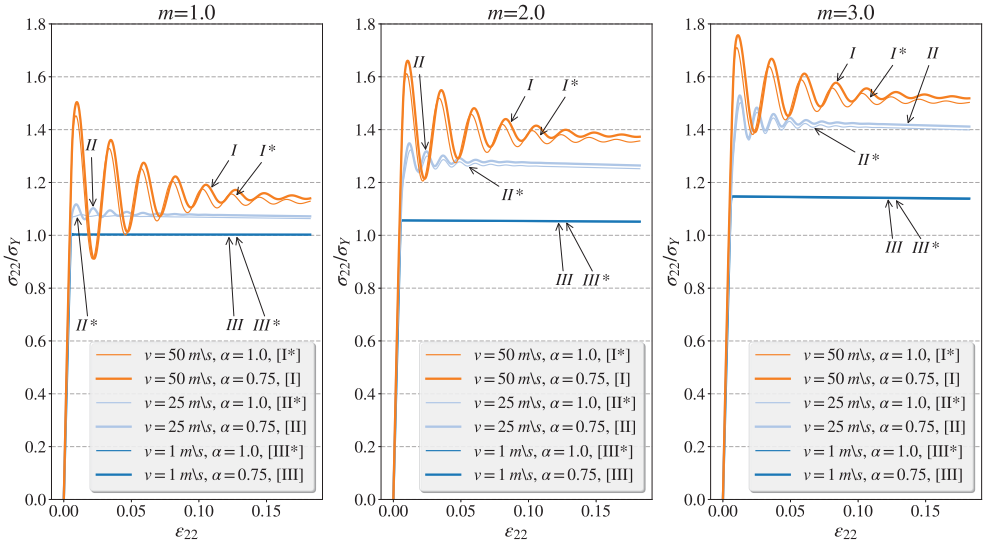

Figure 3.15. Influence of the material parameter m and the value of applied velocity field v on the stress-strain relation, constant parameters: $\alpha = 0.75$, $T_m = 2.5\text{e}{-6}$ s, $\Delta_{11} = 3.0$ [200]

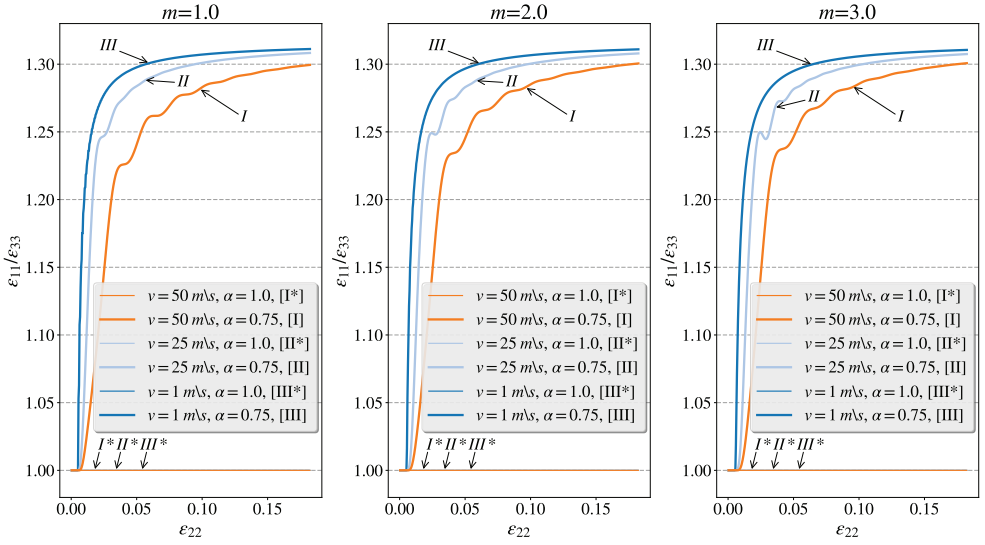

Figure 3.16. Influence of the material parameter m and the value of applied velocity field v on the relation between three normal strains, constant parameters: $\alpha = 0.75$, $T_m = 2.5\text{e}{-6}$ s, $\Delta_{11} = 3.0$ [200]

Table 3.1. Frequency (in MHz) of the stress waves for material parameters T_m = 2.5e−6 s, $m = 1$ [200]

		$\Delta_{22} = 3.0$ [MPa]	$\Delta_{11} = 3.0$ [MPa]
$v = 25$ m/s	$\alpha = 1$	2.085	2.085
	$\alpha = 0.75$	2.108	1.996
$v = 50$ m/s	$\alpha = 1$	2.073	2.073
	$\alpha = 0.75$	2.157	2.028

Table 3.2. Frequency (in MHz) of the stress waves $\Delta_{22} = 3.0$ MPa, $v = 50$ m/s, $\alpha = 0.75$ [200]

		T_m [s]		
		T_m = 2.5e−7 s	T_m = 2.5e−6 s	T_m = 2.5e−5 s
$m = 1$	$\alpha = 1$	2.073	2.073	2.274
	$\alpha = 0.75$	2.157	2.157	2.288
$m = 2$	$\alpha = 1$	2.073	2.085	2.182
	$\alpha = 0.75$	2.157	2.157	2.207
$m = 3$	$\alpha = 1$	2.073	2.085	2.169
	$\alpha = 0.75$	2.157	2.157	2.182

viscoplasticity is obtained, therefore $\mathbf{\Delta}$ parameters do not influence of the frequency. However, for $\alpha = 0.75$ the frequency depends on the inelastic anisotropy introduced by the material parameter $\mathbf{\Delta}$; this is observed for two different velocities.

Tab. 3.2 collects the data from the study conducted in section 3.3.2, regarding the effects of various values of T_m and m. The smallest impact was found for the m parameter since the only changed was recorded for T_m = 2.5e−5 s. For this set of parameters, both for $\alpha = 1$ and $\alpha = 0.75$, the increase of the rate-sensitivity parameter causes the reduction of the frequency. For every value of α and m, the change in frequency is negligibly small for two first columns, i.e. T_m = 2.5e−7 s and T_m = 2.5e−6 s. However, considering the increase in value from T_m = 2.5e−6 s to T_m = 2.5e−5 s, a significant increment of the frequency can be observed.

3.3.4. Conclusions

In this chapter, a generalization of the elastic-viscoplastic material model in the framework of the fractional calculus was presented. Firstly, a concept of a non-integer order derivative was introduced along with a numerical approach for obtaining an approximate solution. Subsequently, the Perzyna-type viscoplasticity was outlined and then modified by replacing an integer-order differential operator with the fractional. This new approach requires numerical implementation, which was discussed in detail and depicted on the flowchart for the clarity's sake. Finally, the effects of parameters that derive from both rate-dependent (viscous) and non-local (fractional) formulation of the model were studied in a series of analyses. The uniaxial tension was achieved by applying the displacement field on the elementary unit cube. By observing deformation in the principle directions and stress-strain relation for various sets of parameters, the following conclusions were drawn:

- fractional viscoplasticity adds two new material parameters, i.e. the order of the viscoplastic flow α and stress-fractional spread $\mathbf{\Delta}$,
- fractional parameters (α and $\mathbf{\Delta}$) change the dynamic properties of the material model, particularly: the rate-dependent hardening, the character of the stress waves and induce inelastic anisotropy,
- relaxation time T_m and the rate-sensitivity parameter m, which originate from the Perzyna model of viscoplasticity, modify the stress wave propagation and strain-rate hardening,
- viscoplastic anisotropy manifests itself in the directionally dependent change of dimensions and stress level in the stress-strain curve,
- stress wave energy dissipation exhibits anisotropy which is observed as the directional change of the wave frequency.

Chapter 4

Fractional viscoplasticity with extended constitutive structure

4.1. General remarks

The fractional viscoplasticity presented in the previous chapter comprises the Perzyna-type viscoplasticity and the stress-fractional framework in which the former was embedded. However, the theory that accounts only for the strain-rate hardening may be considered insufficient to model certain substances, such as porous metals and granular materials. Many effects, including microdamage mechanism, thermo-mechanical coupling and fracture criterion, reflect important physical phenomena that were observed in experiments. The aim of this chapter is twofold. First, the constitutive structure that incorporates the aforementioned effects with the fractional viscoplasticity is going to be proposed. Second, through a series of numerical experiments the localization and development of shear bands in the dynamical tensile tests will be examined.

4.2. Thermo-mechanical response and damage criterion in the framework of the fractional viscoplasticity

The constitutive framework that accounts for material degradation on the microscopic level and thermal softening requires a vector of internal state variables, the following form can be assumed

$$\boldsymbol{\mu} = (\in^{vp}, \xi, \vartheta), \tag{4.1}$$

where ϑ denotes the temperature and $\in^{vp}$ is the equivalent viscoplastic deformation (strain), given by

$$\in^{vp}= \int_0^t \left(\frac{2}{3} \dot{\boldsymbol{\varepsilon}}^{vp} : \dot{\boldsymbol{\varepsilon}}^{vp} \right)^{1/2} dt \tag{4.2}$$

and ξ is a microdamage quantitative parameter which in metals may be interpreted as a volume fraction porosity. The evolution of viscoplastic strain has the form presented previously (3.33) and the isotropic work-hardening/softening function is given as

$$\kappa = \overline{\kappa}\big(\xi, \vartheta, \in^{vp}\big). \tag{4.3}$$

The intrinsic microdamage parameter ξ was presented and thoroughly discussed in papers [46, 152, 153] with particular attention focused on the time-dependent effects. In general, it consists of two parts: first is responsible for the voids nucleation process and, second governs the growth mechanism [41, 156, 157]. The computational effort resulting from the nucleation can be reduced by assuming the initial volume porosity – ξ_0 [39, 159]. Therefore, the evolution of voids can be postulated as [40, 90, 159]

$$\dot{\xi} = \frac{1}{T_m} \frac{g^*(\xi, \vartheta)}{\kappa_0} \Big[I_g - \tau_{eq}(\xi, \vartheta, \in^{vp}) \Big], \tag{4.4}$$

where κ_0 denotes the initial yield stress in simple shear, $T_m \kappa_0$ defines the dynamic viscosity of the material, $g^*(\xi, \vartheta)$ denotes the void growth material function and $\tau_{eq}\,(\xi, \vartheta, \in^{vp})$ represents the stress threshold. The stress intensity invariant is defined as

$$I_g = b_1 J_1 + b_2 \sqrt{J_2'}, \tag{4.5}$$

where b_1 and b_2 are material constants and J_1 denotes the first invariant of the stress tensor. The Eq. (4.4) has to be supplemented with the definitions:

$$g^*(\xi, \vartheta) = c_1(\vartheta) \frac{\xi}{1-\xi}, \tag{4.6}$$

and

$$\tau_{eq}\big(\xi, \vartheta, \in^{vp}\big) = c_2(\vartheta)(1-\xi) \ln \frac{1}{\xi} \Big\{ 2\kappa_s(\vartheta) - \Big[\kappa_s(\vartheta) - \kappa_0(\vartheta) \Big] F(\xi_0, \xi, \vartheta) \Big\}, \tag{4.7}$$

where

$$F(\xi_0, \xi, \vartheta) = \left(\frac{\xi_0}{1-\xi_0} \frac{1-\xi}{\xi} \right)^{(2/3)\delta(\vartheta)} + \left(\frac{1-\xi}{1-\xi_0} \right)^{(2/3)\delta(\vartheta)}, \tag{4.8}$$

$\delta(\vartheta)$ is a material function that models the level of non-linearity in the material hardening, c_1 and c_2 are experimentally determined constants (cf. [18, 38]).

The isotropic work-hardening/softening function κ can be postulated as [135, 153]

$$\kappa = \overline{\kappa}\big(\xi, \vartheta, \in^{vp}\big) = \Big\{ \kappa_s(\vartheta) - [\kappa_s(\vartheta) - \kappa_0(\vartheta)] \exp\left[-\delta\left(\vartheta\right) \in^{vp} \right] \Big\} \left[1 - \left(\frac{\xi}{\xi_F} \right)^{\beta(\vartheta)} \right], \tag{4.9}$$

where

$$\begin{aligned}\kappa_s(\vartheta) &= \kappa_s^* - \kappa_s^{**}\overline{\vartheta},\\ \kappa_0(\vartheta) &= \kappa_0^* - \kappa_0^{**}\overline{\vartheta},\\ \beta(\vartheta) &= \beta^* - \beta^{**}\overline{\vartheta},\\ \overline{\vartheta} &= \frac{\vartheta - \vartheta_0}{\vartheta_0},\\ \delta(\vartheta) &= \delta^* - \delta^{**}\overline{\vartheta},\end{aligned} \tag{4.10}$$

$\kappa_s^*, \kappa_s^{**}, \kappa_0^*, \kappa_0^{**}, \beta^*, \beta^{**}, \vartheta_0, \delta^*, \delta^{**}$ are material constants and ϑ_0 indicates the reference temperature, assumed to be 293 K. Components $\kappa_0(\vartheta)$ and $\kappa_s(\vartheta)$ denote the yield and saturation stress, both temperature-dependent and considered to simple shear, respectively. The second part of the Eq. (4.9) takes into account the nucleation and growth of the voids in the material. The temperature-dependent function $\beta(\vartheta)$ models the relation between the growth of porosity and the material softening.

The critical value of porosity ξ_F marks the level of damage that leads to the loss of carrying capacity. This means that for $\xi = \xi_F$, the following is true

$$\kappa = \overline{\kappa}\big(\xi, \vartheta, \in^{vp}\big)|_{\xi=\xi_F} = 0, \tag{4.11}$$

and is referred to as a fracture criterion.

As the main subject of this treatise is a study of dynamic loading processes, the temperature evolution can be postulated as

$$\dot{\vartheta} = \frac{\chi^*}{\rho c_p}\boldsymbol{\sigma} : \dot{\boldsymbol{\varepsilon}}^{vp} + \frac{\chi^{**}}{\rho c_p}\dot{\xi}_{grow}, \tag{4.12}$$

where χ^* and χ^{**} denote the irreversibility coefficients and c_p is specific heat. By postulating that the progressive degradation of material does not contribute to temperature growth, which was suggested in [42], $\chi^{**} = 0$ can be assumed. The foregoing means that the temperature rise is controlled only by the rate of the inelastic work.

The previously stated yield function (3.22) is in accord with the classical plasticity theory that assumes volume constancy during inelastic deformation; this holds for non-porous materials. However, in the deformation process of porous metals, or the porous materials in general, the volume can change. In order to address this issue, new theories have been developed that suggest the yield criterion based on the first invariant of the stress, $J_1 = \sigma_{11} + \sigma_{22} + \sigma_{33}$, and the second invariant of deviatoric stress J_2' [70, 151, 176]. Therefore, the plastic potential function can be assumed in the form [42]

$$f = \sqrt{J_2' + J_1^2 \cdot \Big[n_1(\vartheta) + n_2(\vartheta)\xi\Big]}, \tag{4.13}$$

where $n_1(\vartheta) = 0$ and $n_2(\vartheta) = n_2 = \text{const}$ are material parameters.

4.3. Implementation – VUMAT subroutine

Implementation of the numerical solution of the viscoplastic flow, based on the fractional derivative, was discussed in section 3.2.3 and the same formulation will be adopted here. The content of that section was consistent with the parametric study conducted later (section 3.3). Here, however, attention will be focused on presenting in detail the procedure that governs the calculations in the elastic-viscoplastic constitutive structure valid for the thermo-mechanically coupled process with damage criterion. The complete procedure was depicted in the flowchart in Fig. 4.1. It should be pointed out that notation $(\cdot)_{,n}$ (e.g. $I_{g,n}$) used in this flowchart indicates n-th time increment rather than a partial differentiation with respect to a spatial variable.

In general, within the space of a single time increment, from t_n to t_{n+1}, the procedure yields the stresses $\boldsymbol{\sigma}_{n+1}$ and updates the internal variables $\boldsymbol{\mu}_{n+1}$. Prerequisites for every step are the strain increment $\boldsymbol{\varepsilon}_{n+1}$, supplied by the Abaqus\Explicit solver, and the $\boldsymbol{\mu}_n$ vector of previously obtained internal variables. The calculations start with obtaining the increment of the trial stress via the isotropic Hooke's law

$$\Delta\boldsymbol{\sigma}_{n+1}^{trial} = \mathcal{L}^e \Delta\boldsymbol{\varepsilon}_{n+1}, \tag{4.14}$$

which is subsequently added to the stresses from previous stage

$$\boldsymbol{\sigma}_{n+1}^{trial} = \boldsymbol{\sigma}_n + \Delta\boldsymbol{\sigma}_{n+1}^{trial}. \tag{4.15}$$

This is sufficient for verifying the yield condition

$$f = \{J_2'\left(\boldsymbol{\sigma}_{n+1}^{trial}\right) + n_2 \xi J_1^2\left(\boldsymbol{\sigma}_{n+1}^{trial}\right)\}^{1/2} > \kappa_n. \tag{4.16}$$

If the condition is not met, it means that the elastic trial step lies within the elastic domain or on the yield surface. Therefore, the following holds

$$\begin{aligned} \Delta\boldsymbol{\varepsilon}_{n+1} &= \Delta\boldsymbol{\varepsilon}_{n+1}^{e}, \\ \boldsymbol{\mu}_{n+1} &= \boldsymbol{\mu}_n. \end{aligned} \tag{4.17}$$

Conversely, if the yield condition is fulfilled, then multiplier Λ_n and the direction of viscoplastic flow $\boldsymbol{p}_n$ ought to be calculated. Next, assuming the explicit forward Euler difference scheme, the viscoplastic strain tensor can be obtained via

$$\begin{aligned} \Delta\boldsymbol{\varepsilon}_n^{vp} &= \Delta t \Lambda_n \mathbf{p}_n \left|\left|\mathbf{p}_n\right|\right|^{-1}, \\ \boldsymbol{\varepsilon}_{n+1}^{vp} &= \boldsymbol{\varepsilon}_n^{vp} + \Delta\boldsymbol{\varepsilon}_n^{vp}, \end{aligned} \tag{4.18}$$

where Δt is a time increment. The vector of internal variables $\boldsymbol{\mu}_{n+1}$ is updated similarly; details were presented in Fig. 4.1. Finally, the elastic part of the strain tensor is determined through

$$\boldsymbol{\varepsilon}_{n+1}^{e} = \boldsymbol{\varepsilon}_n^{e} + (\Delta\boldsymbol{\varepsilon}_{n+1} - \Delta\boldsymbol{\varepsilon}_n^{vp}) = \boldsymbol{\varepsilon}_n^{e} + \Delta\boldsymbol{\varepsilon}_{n+1}^{e}. \tag{4.19}$$

The last result is then used, along with the Hooke's law, to retrieve the current stress state

$$\boldsymbol{\sigma}_{n+1} = \mathcal{L}^e \boldsymbol{\varepsilon}^e_{n+1}. \tag{4.20}$$

4.4. Numerical study

4.4.1. Experimental results

Tensile testing is a fundamental tool used in engineering for determining material behaviour and mechanical properties. Two types of tensile specimens are most common: first, has a round cross-section and second is a flat specimen with a section of reduced size in the middle. This last type is sometimes referred to as the dog-bone specimen. In the literature, many results of experiments conducted on flat test samples can be found. Here, a small subset of this research focused on the strain-rate sensitivity, localized deformation and shear banding was chosen.

In experiments conducted by Chakrabarti and Spretnak [18] flat sheet specimens of different width to thickness ratio were subjected to quasi-static tensile loading. In Fig. 4.2 an initiation and evolution of the shear bands were shown. The first picture on the left presented the onset of the localization of plastic deformation. In the subsequent frames, the instability bands are formed and the majority of the deformation is confined in one band. It becomes an active instability zone where the failure occurs by shearing through the material.

The quasi-static uniaxial tensile and compression tests for various strain rates were performed in [88]. Test specimens were made out of ultrafine-grained titanium. In this study different mode of deformation was observed, namely the inelastic strains were localized to a necking area – cf. Fig. 4.3. Moreover, authors concluded that for testes carried out with different strain rates increase in material strength was observed. This strain-rate hardening could help to overcome softening caused by material flaws.

The foregoing results present only a subset of deformation modes that can occur during tensile testing. Detailed analysis of material behaviour may require including effects such as thermal softening and microdamage mechanism, which favours strain localization, and strain-rate sensitivity and work hardening, which oppose shear localization. Therefore, the final behaviour of the material is a composition of these competing phenomena.

4.4.2. Description of numerical tension test

In order to verify the dynamic response of the model and influence of various parameters on the formation and localization of the shear band, a series of numerical analysis was conducted. Dimensions of the dog-bone specimen used in these tests were illustrated in Fig. 4.4. Both dimensions and thickness ($h_t = 0.8$ mm) were based on works [171, 193]. The experimental setup was also depicted in Fig. 4.4, with one end pinned, i.e.

Given parameters:
$E, \nu, \rho, \kappa_0^*, \kappa_0^{**}, \kappa_s^*, \kappa_s^{**}, \delta^*, \delta^{**}, \beta^*, \beta^{**}, \chi^*, c_p, \xi_F, \vartheta_0, \xi_0, \xi_F, T_m, m, c_1, c_2, b_1, b_2, n_2, \boldsymbol{\Delta}, \alpha$

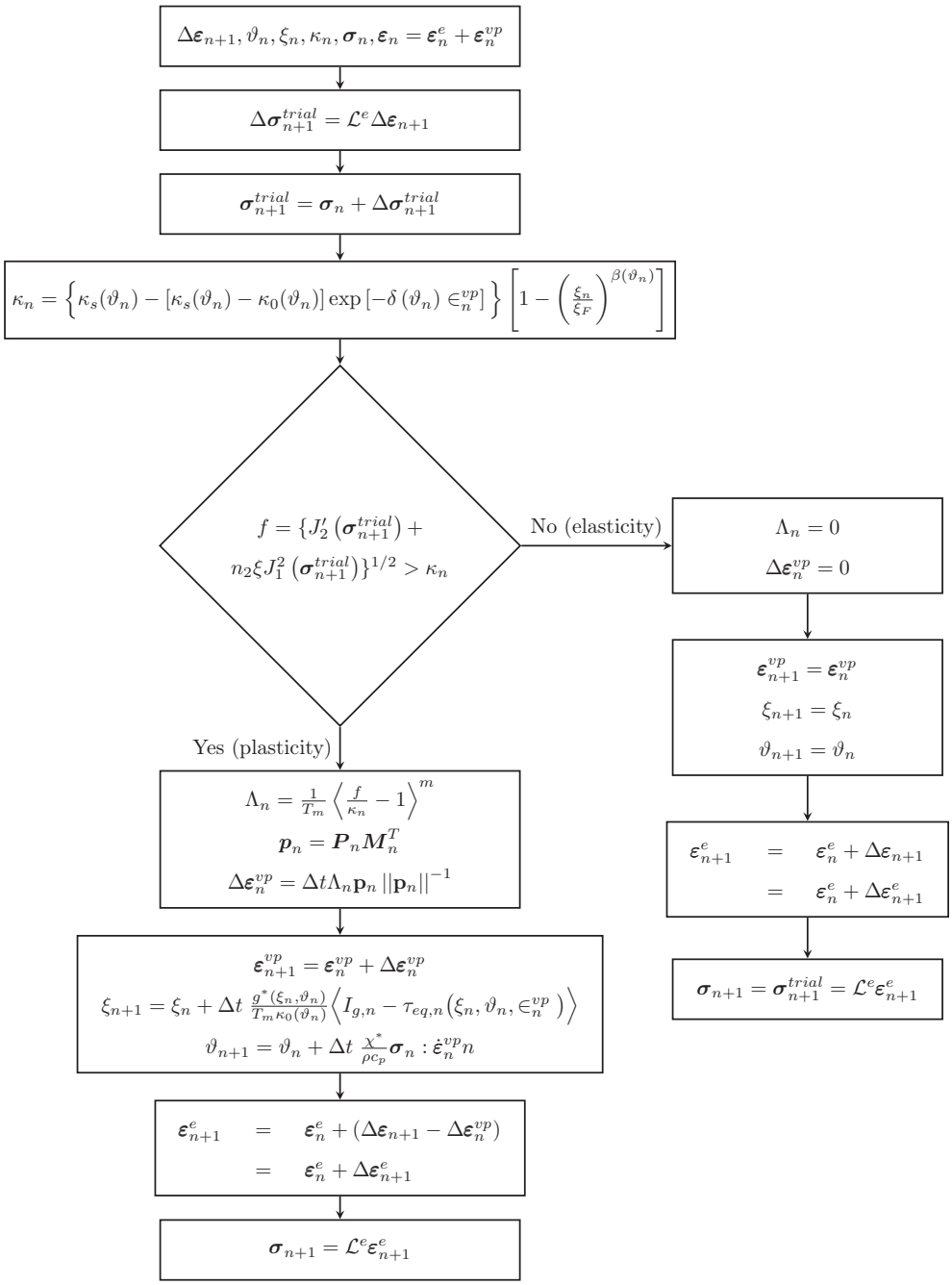

Figure 4.1. VUMAT subroutine flowchart for the fractional viscoplastic rule

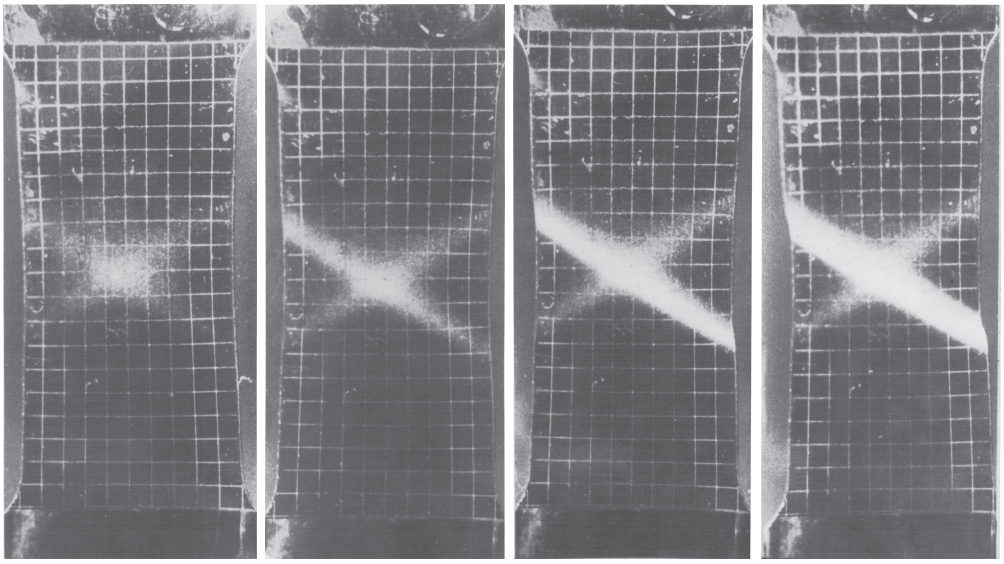

Figure 4.2. Initiation and gradual development of instability bands in 0.099 cm thick specimen [18]

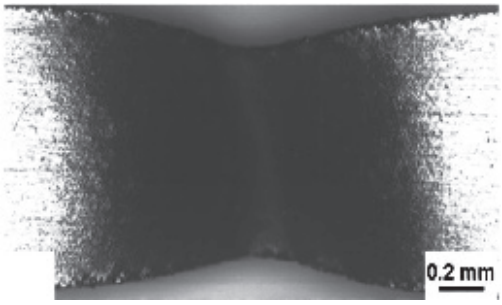

Figure 4.3. Optical micrograph showing necking in the annealed ultrafine-grained titanium (UFG-Ti) [88]

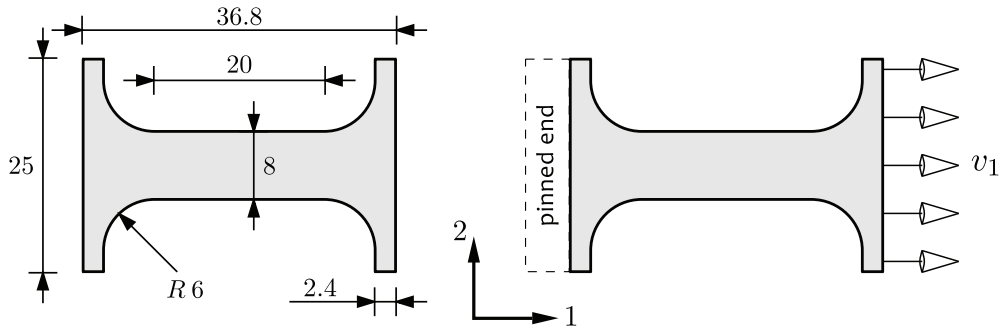

Figure 4.4. Dimensions and boundary conditions of the dog-bone specimen in an uniaxial tensile test

displacements $u_1 = u_2 = u_3 = 0$. The other side was subjected to the displacement field v that applies tension in the (1) direction. The numerical study was conducted for various velocities $v \in \{10, 25, 50, 100\}$ m/s, therefore inducing corresponding average strain rates 500, 1250, 2500, 5000 s^{-1}, in the gauge region. The results presented in this chapter have been published in [201].

4.4.3. FEM model and material parameters

The geometry of the dog-bone was modelled in Abaqus with C3D8R elements (8-node linear brick, reduced integration element). Multiple sections were created to ensure a generation of symmetric mesh, which was presented in Fig. 4.5. Model partition ensures a smooth transition between curved and straight parts and follows the specimen outline. Eight solid elements were used through the thickness to capture the first symptoms of necking during loading and properly execute the element deletion method, based on the previously mentioned damage criterion. The model accuracy comes with its cost since it has 1125k degrees of freedom. Numbers in Fig. 4.5 refer to points for which the internal state variables were determined; these results are discussed later in text (cf. Figs. 4.10–4.13). It is worth noting that no discontinuities nor inhomogeneities in the mesh geometry were used to stimulate the onset of damage nucleation.

The material parameters (summarized in Tab. 4.1) used in this numerical study were based on the work of Dornowski and Perzyna [42]. These are required by the elastic-viscoplastic part of the material model and were chosen through a curve fitting against experimental results obtained by Chakrabarti and Spretnak [18]. Finally, assuming that $\mathbf{\Delta}^L = \mathbf{\Delta}^R$, the number of parameters is equal to 31.

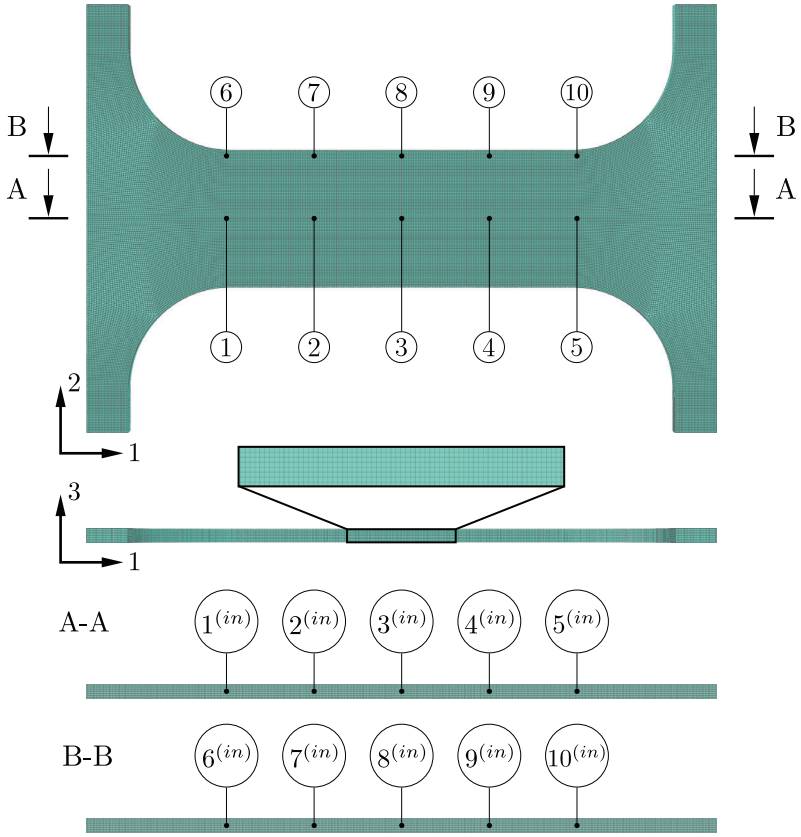

Figure 4.5. Finite element model of a dog-bone specimen. Numbers refer to points where the state variables were examined; those results are discussed later

Table 4.1. Material parameters based on work [42] by Perzyna and Dornowski

$\kappa_s^* = 808$ MPa	$\kappa_s^{**} = 230$ MPa	$\kappa_0^* = 635$ MPa	$\kappa_0^{**} = 181$ MPa
$\beta^* = 2.2$	$\beta^{**} = 0.63$	$\vartheta_0 = 293$ K	$\rho_{ref} = 7850$ kg/m^3
$E = 205$ GPa	$\nu = 0.27$	$T_m = 0.01$ μs	$m = 1$
$c_1 = 0.202$	$c_1 = 0.067$	$b_1 = 1.0$	$b_2 = 1.3$
$\xi_0 = 6 \cdot 10^{-4}$	$\xi_F = 0.2$	$\delta^* = 28$	$\delta^{**} = 8$
$n_1 = 0$	$n_2 = 0.25$	$\chi^* = 0.9$	$c_p = 455$ J/kg K

4.5. Numerical examples

4.5.1. General remarks

In this section, the behavior of the fractional viscoplastic model is examined in a dynamic tension test. First, the internal fields, namely equivalent viscoplastic strain $\in^{vp}$, temperature ϑ, porosity ξ, and work-hardening/softening strength parameter κ were captured during loading and after material failure. Next, the values of these variables were measured in 20 different points and plotted against time. Finally, the evolution of the intrinsic microdamage parameter was examined. Numerical analyses, conducted in this part of the study, were all carried out for velocity $v = 50$ m/s, and fractional parameters $\alpha = 0.5$ and $\Delta_{22} = 3.0$ MPa.

In the second part, a parametric study was conducted where the deformation process was observed as a function of α and $\mathbf{\Delta}$ and the load velocity. The three-dimensional numerical model of the tensile test allows for close observation of the shear bands formation and the necking process. Also, the localization of the maximum strain region as a function of the α, $\mathbf{\Delta}$ and velocity is here discussed. In the second part, mainly the distribution of $\in^{vp}$ will be presented on the contour plots, with two additional charts for ϑ and κ. However, this should not diminish its scientific value since there is a strong coupling between the state variables, which will be demonstrated.

4.5.2. State variables evolution

In Figs. 4.6 and 4.7 the specimen after over 0.1 ms of loading is presented. It can be observed that the region where the viscoplastic strain occurs is limited to the necking area, while the rest of it is in the elastic state – cf. Fig. 4.6a. The zone, where strain is significantly greater than the surrounding regions, is not evenly distributed, rather it is confined to a small area within the narrow section. Temperature distribution, as presented in Fig. 4.6b is similar to the inelastic strain above. This is to be expected since, according to Eq. (4.12) and the value of coefficient χ^*, 90 percent of the viscoplastic work dissipates into heat. Damage understood as an increase of porosity is presented in Fig. 4.7a. A slight increase in value can be observed in the area that corresponds to the maximum value of $\in^{vp}$. Yield strength, denoted by κ, shows the greatest volatility amid all internal state variables. The red contours mark the hardening of the material, i.e. the value of κ increased over its initial value of κ_0, while the blue area indicates the material softening. The latter is coupled with the areas of increased strain and temperature.

The computational case, where the deformation progress to a point of material failure, was depicted in Figs. 4.8 and 4.9. In can be seen that the damage occurred in the place where values of $\in^{vp}$, ϑ, ξ were growing. Development of the field ξ is particularly crucial as the element deletion method executes when it reaches a critical value - ξ_F. These numerical examples show that state variables are strongly coupled

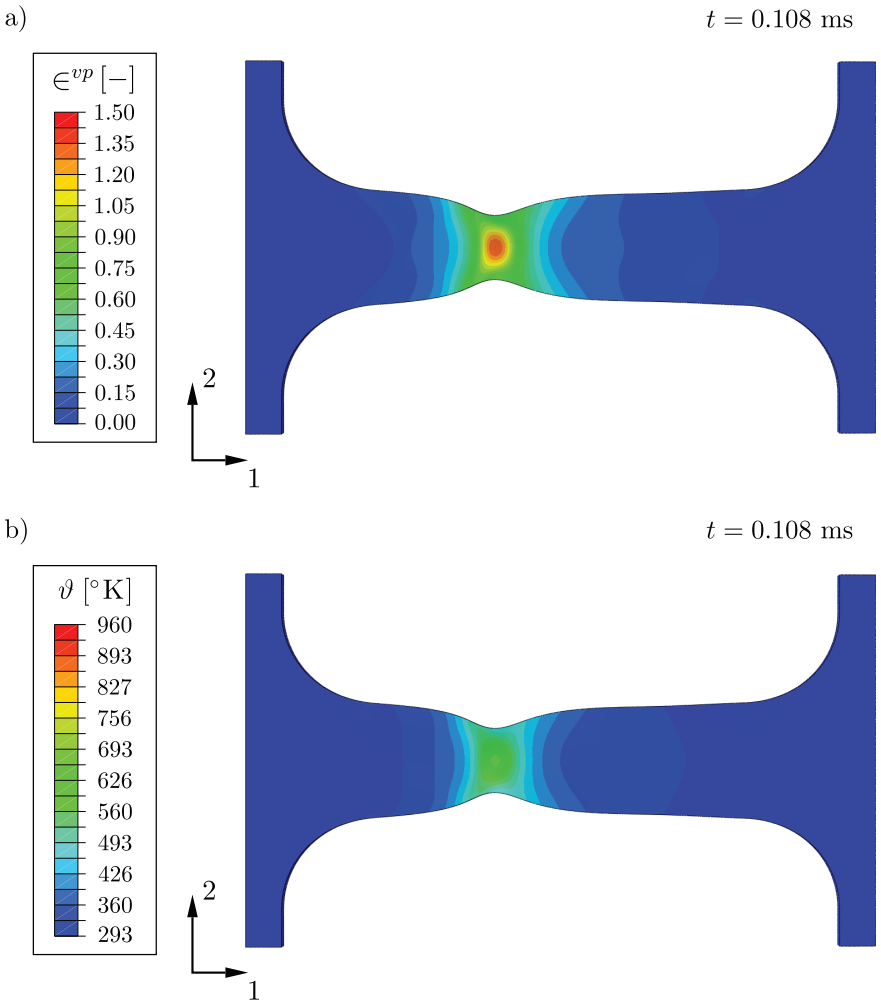

Figure 4.6. Contour plot of: a) equivalent viscoplastic strain and b) temperature during deformation [201]

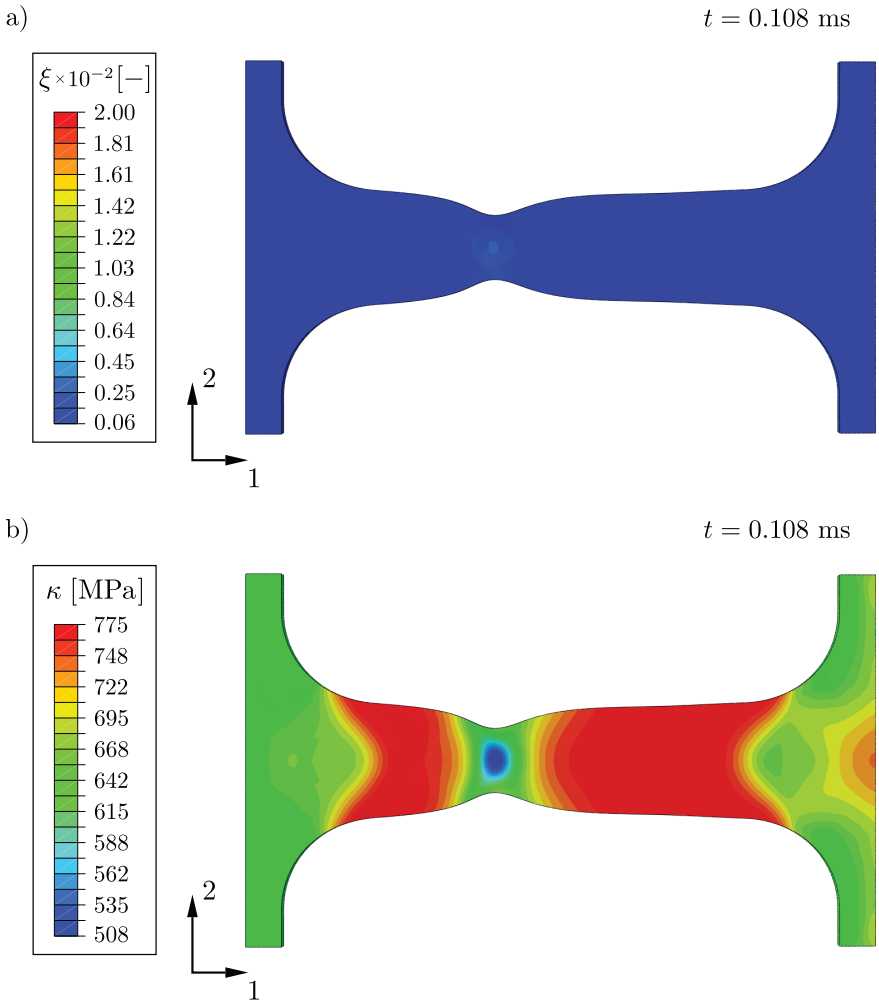

Figure 4.7. Contour plot of: a) porosity and b) work-hardening/softening function [201]

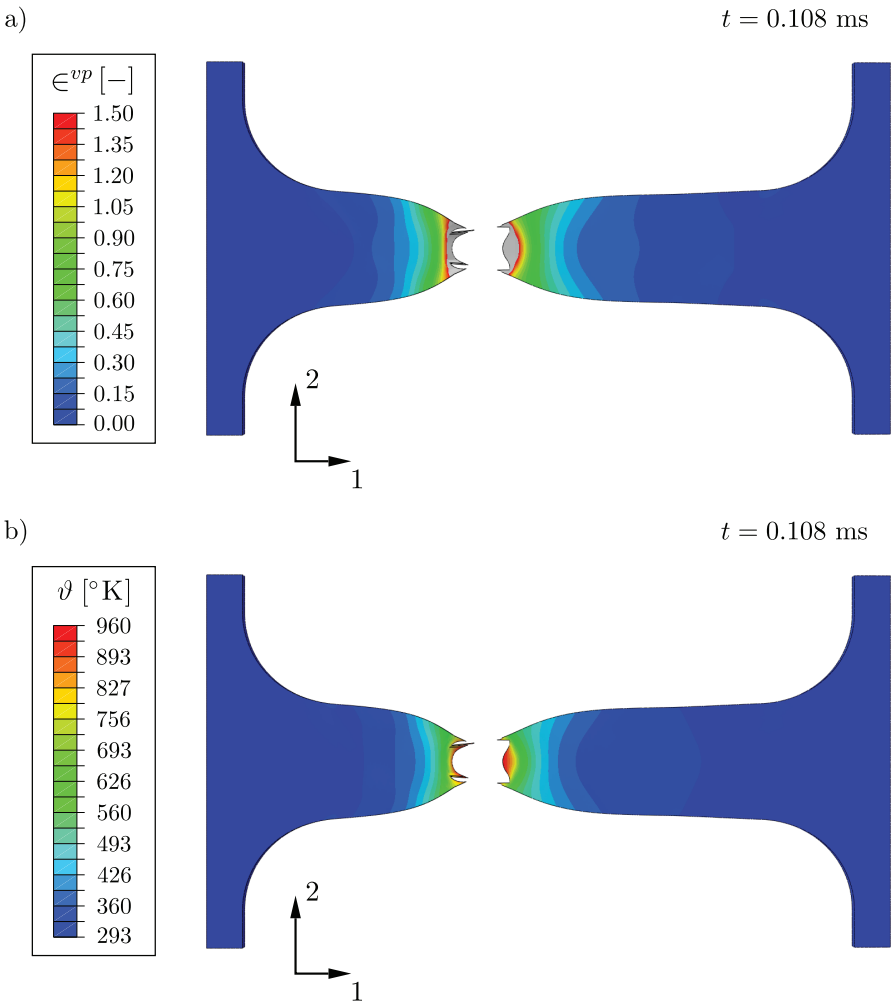

Figure 4.8. Contour plot of: a) equivalent viscoplastic strain and b) temperature during deformation after material damage [201]

and are not uniformly distributed. In the subsequent section (4.5.5), the main focus will be on the evolution of $\in^{vp}$, but it should be remembered that in each case all internal state variables change as deformation progresses.

4.5.3. State variables evolution at selected integration points

The foregoing results were snapshots of the deformation progress and clearly show that the values of internal fields are non-uniformly distributed. In order to analyze the evolution of the state variables their values were sampled in 20 different points (cf.

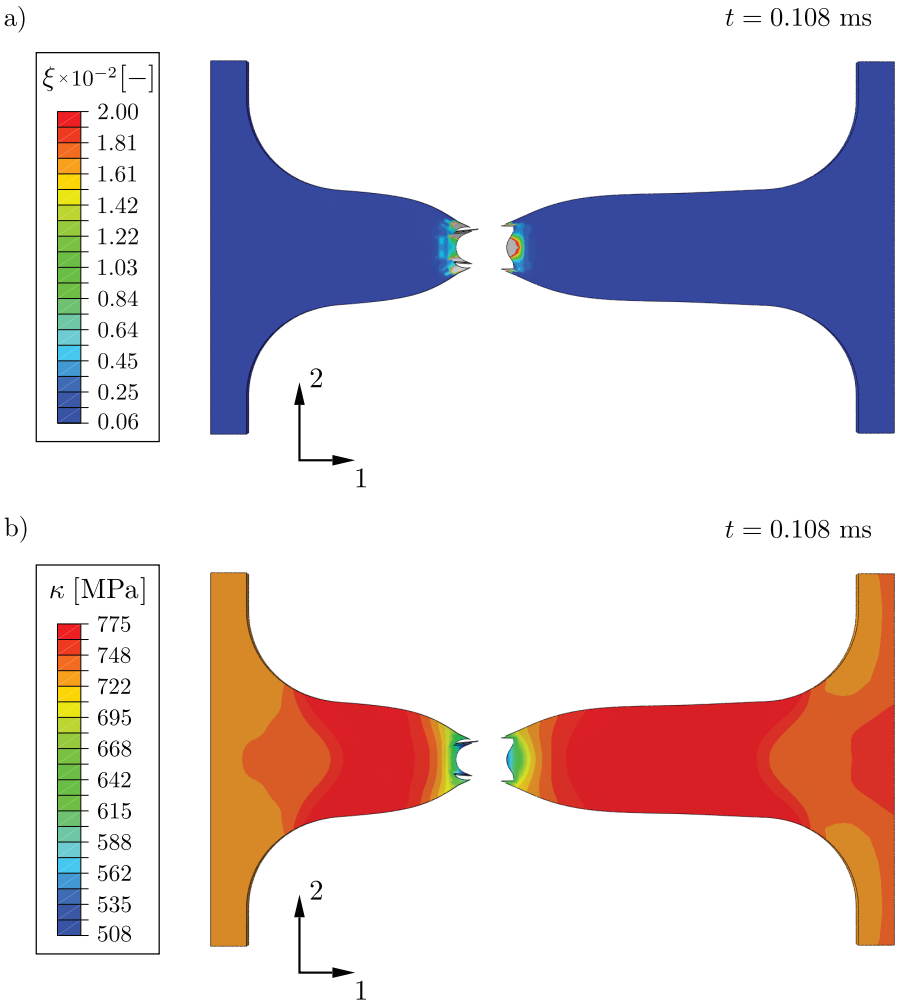

Figure 4.9. Contour plot of: a) porosity and b) work-hardening/softening function after material damage [201]

Fig. 4.5) and plotted against the time in Figs. 4.10–4.13. The location of these points was illustrated in Fig. 4.5. The superscript (in), was used to denote the points that are a projection of points on the dog-bone specimen surface, with the same indexes.

As was mentioned before, the element deletion method is controlled by the value of intrinsic microdamage ξ and is triggered when it reaches the critical value, i.e. $\xi_F = 0.2$. However, sometimes the growth of ξ is progressing slowly and the ξ_F threshold is never exceeded, resulting in excessive distortion of elements. This can be largely avoided by using an additional coefficient (0.9) which lowers the threshold. Hence, the value of ξ in the charts never exceeds 0.18.

In the first group, points 1 to 5 in Fig. 4.10, the biggest changes can be observed in point 2 which is located close to the strain localization. The rise and fall of current yield shear strength (κ) illustrate two phases of deformation which end when the material degradation depletes its load-carrying capacity. This is correlated with the evolution of voids (ξ), inelastic strain ($\in^{vp}$) and temperature increase (ϑ). The next group comprises of points $1^{(in)}$–$5^{(in)}$, which correspond to points 1–5 but are located inside the material. The main difference observed here are lower levels of ϑ and $\in^{vp}$, cf. Fig. 4.11.

The second group is formed by points 6 to 10, selected to illustrate state variables evolution at the edge of the specimen. These points were chosen so that their placement on the horizontal axis was consistent with points 1–5. Fig. 4.12 illustrates the deformation process on the surface of the dog-bone model in these points. Both the hardening and softening of the material can be observed in Fig. 4.12a however, conversely to previous examples, its strength is not completely depleted due to the deformation. This can be explained by a zero value of the microdamage tensor ξ and lower values of $\in^{vp}$ and ϑ. In other words, material softening on the surface is driven only by the thermal effects.

Fig. 4.13 illustrates state variables inside the specimen located close to its edge. Here, the current yield shear strength degradation is similar to what was observed for points 1–5, as it falls to zero. Also, it can be noted how rapidly material load-carrying capacity deteriorated once the value of ξ started to rise.

4.5.4. Fracture criterion based on the evolution of the microdamage

In the fractional viscoplasticity, the depreciation of load-carrying capacity is caused by the thermal softening and internal damage, however only the latter determines the material degradation leading to material fracture. The microdamage-based criterion is used to trigger the element deletion procedure in Abaqus\Explicit when ξ exceeds the limit of ξ_F. Stress value at the material point decreases exponentially, according to the isotropic hardening-softening material function κ proposed in Eq. (4.9), potentially going to zero if the fracture occurs. This behaviour is consistent with experimental observations [155]. In the following figure, the damage progression during the dynamic loading and evolution of ξ in various points is analyzed.

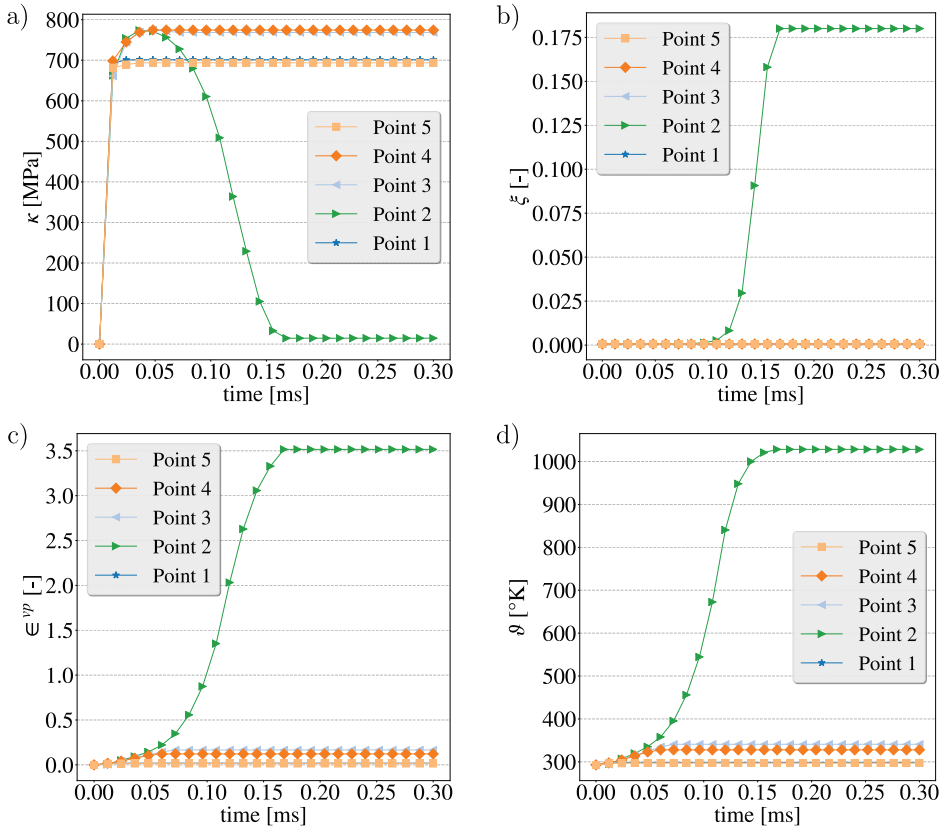

Figure 4.10. State variables on the surface of the dog-bone model for points 1–5 (cf. Fig. 4.5) [201]

Fig. 4.14 illustrates the location and number of elements, denoted in the black rectangular, where the critical value ξ_F was reached. For the sake of clarity, the position of damaged elements is presented on the undeformed model. The progress of the damage was captured for 6 different time steps. It can be observed that the material failure begins inside and propagates towards edges. A detailed evolution of ξ in 5 different points is depicted in Fig. 4.15. This is in line with the previous observation, i.e. the further from the center of the specimen the later the fraction begins. Also, the maximum value of the damage parameter ξ equals 0.18, due to the reasons mentioned earlier (section 4.5.3).

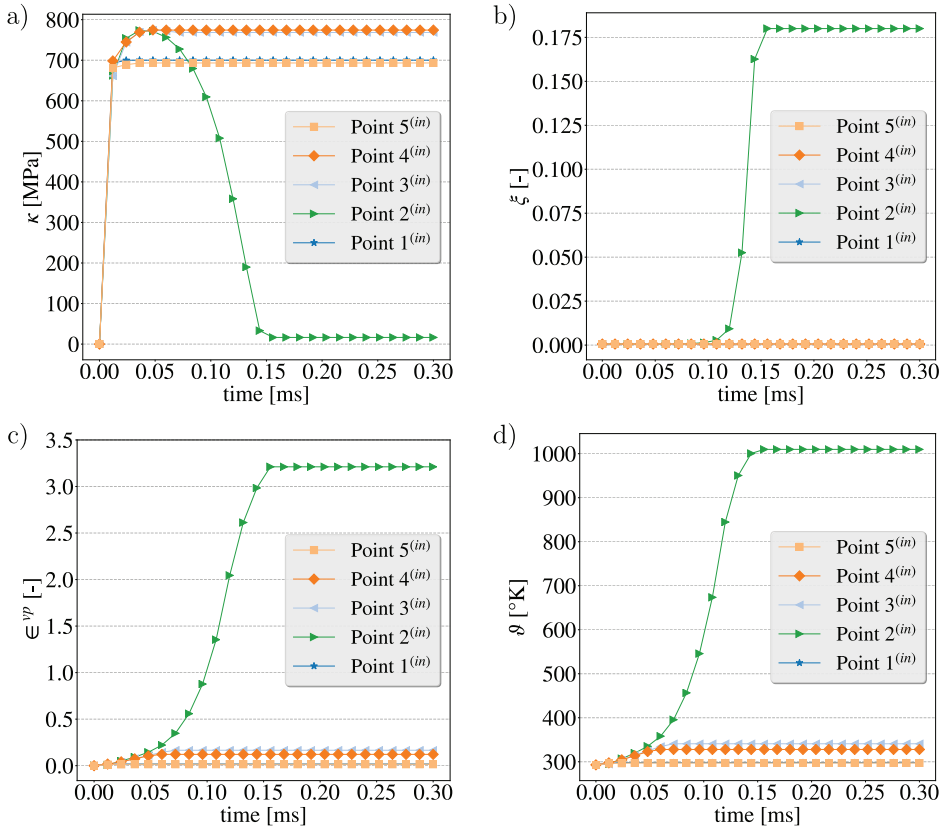

Figure 4.11. State variables inside the dog-bone model for points $1^{(in)}$–$5^{(in)}$ (cf. Fig. 4.5)

4.5.5. Parametric study

Numerical investigations presented in this section were designed to examine the rate-dependent behaviour of the fractional model. Without the loss of generality, results were collected for two values of $\alpha \in \{1, 0.5\}$ and three $\boldsymbol{\Delta}$ parameters. When the stress-fractional spread is set to be dominant in one direction, for instance $\Delta_{11} = 3.0$, then the remaining parameters are equal to one, i.e. $\Delta_{22} = 1.0$ and $\Delta_{33} = 1.0$. Each column presents results for different velocities and different moments in time, $t \in \{0.0003, 0.000176, 0.0001, 0.00005\}$ s, selected to present similar deformation progress. Symbol x_k is used to denote the distance between the loaded end (top) and the place where $\in^{vp}$ is maximum. Also, under each strain map, there is a cross-section (A–A) of the zone where the deformation reaches the peak value. The maximum value of

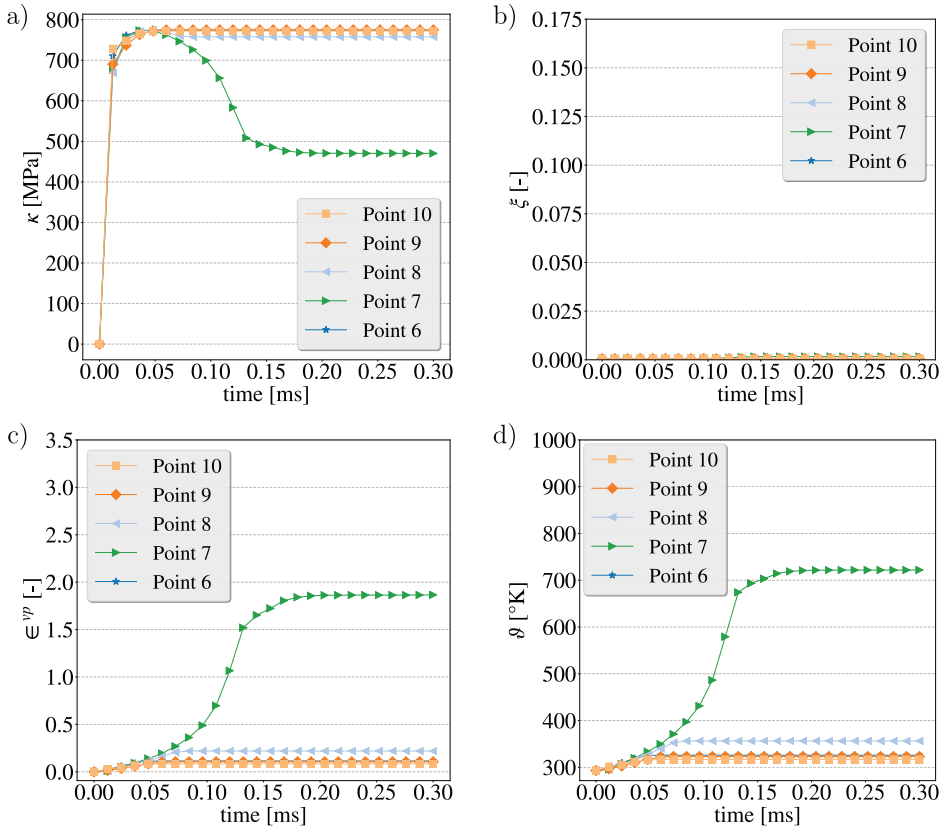

Figure 4.12. State variables on the surface of the dog-bone model for points 6–10 (cf. Fig. 4.5)

equivalent viscoplastic strain presented on these figures is 1.5. Zones that exceed this value are marked by grey colour.

In Fig. 4.16 the Perzyna-type viscoplasticity is obtained for $\alpha = 1$ and the case where the viscoplastic flow is induced in the (1) direction ($\Delta_{11} = 3.0$). The necking localization depends on the velocity however, it does not change considerably between the classical and fractional material model; cf. the first and second row of Fig. 4.16. For $\alpha = 1$, the lateral deformation depicted on the cross-section is greater than for the fractional case in the same figure. This is a result of inducing inelastic flow in the (1) direction, which increases the energy dissipation along one axis, thus reducing deformation in other directions.

The foregoing phenomenon can be also observed in Fig. 4.17 where the intensified viscoplastic flow is produced in the (2) and (3) direction. Again, the inelastic deforma-

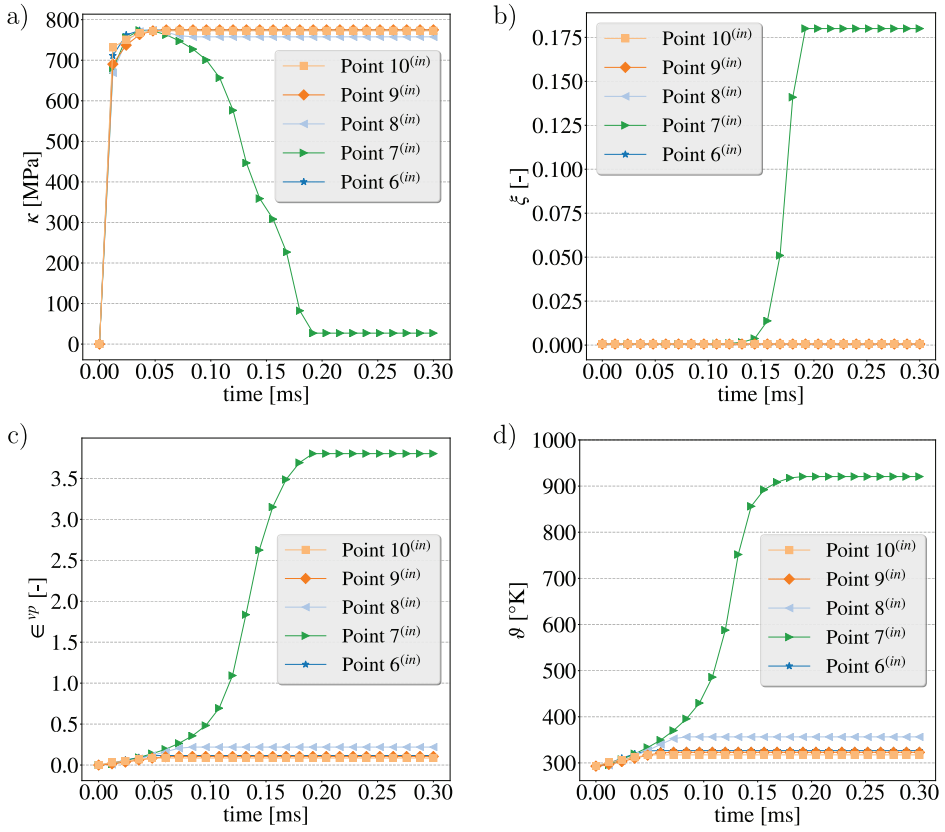

Figure 4.13. State variables inside the dog-bone model for points $6^{(in)}$–$10^{(in)}$ (cf. Fig. 4.5)

tion, as seen in the A–A cross-section, is the greatest along the axis that corresponds to the direction of $\mathbf{\Delta}$. In the top row reduction of the dimensions is the largest in the direction (2), and, respectively, the largest change of size is observed in the direction (3) in the bottom row. Moreover, the shape of the shear bands is also different in these two cases, which is discussed later. The last relevant conclusion can be drawn from observing the level of viscoplastic strain in different columns. As the velocity increases the intensity of $\in^{vp}$ decreases, which is most probably the result of rate-dependent hardening.

Figs. 4.18 and 4.19 present a detailed view of the zone where the viscoplastic deformation is concentrated. In addition, two parameters, h_t and w_t, which denote the dimensions of the deformation zone, were given. It can be seen that induced anisotropy in the direction (1), bottom row in Fig. 4.18, prevents the formation of any distinct

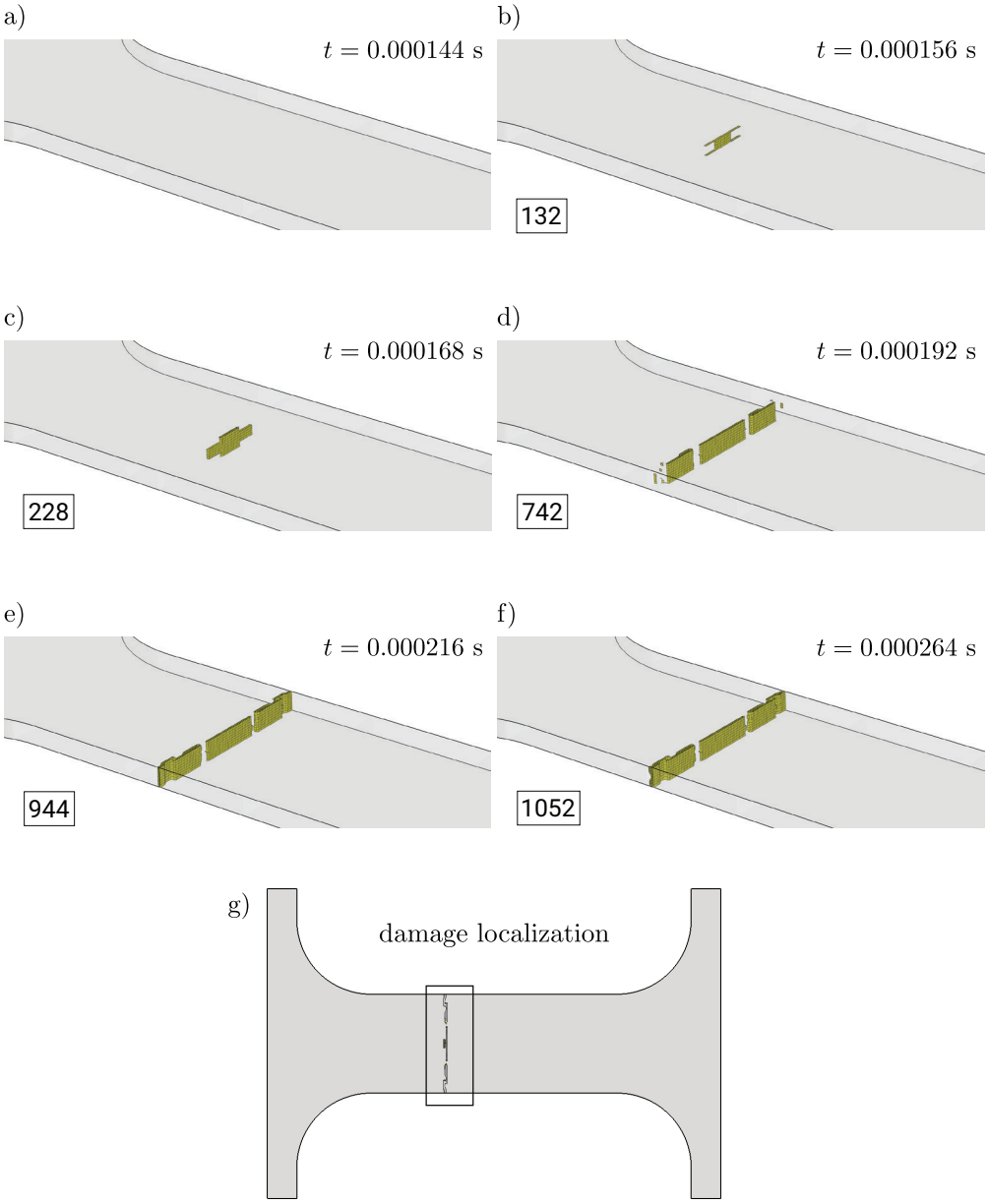

Figure 4.14. Fracture localization on the undeformed dog-bone numerical model

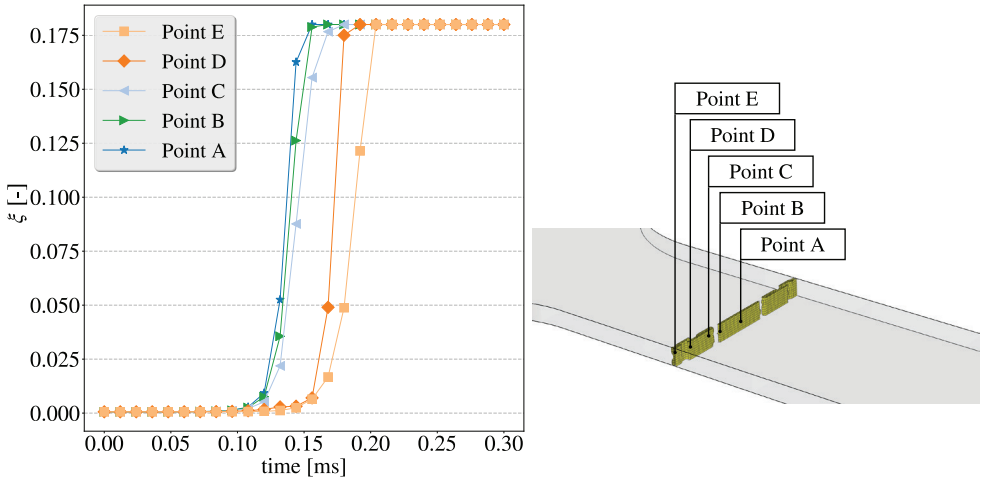

Figure 4.15. Microdamage evolution inside the specimen for the five points denoted as A–E

pattern. Moreover, dimensions do not differ significantly from those for an undeformed specimen, i.e. $w_t = 8$ mm and $h_t = 0.8$ mm. For $\alpha = 1$ the strain-rate hardening is visible since the shear bands are forming for $v \in \{10, 25\}$ m/s, but disperse when the velocity increases. The same behaviour is observed in Fig. 4.19 where the pattern becomes blurry as the velocity grows.

The most intense size change occurs along the axis (2) for $\Delta_{22} = 3.0$, cf. Fig. 4.17. Thus, w_t is the smallest of all four sets of parameters in this particular case. Identical relation can be identified when $\Delta_{33} = 3.0$ and the lowest value of h_t is recorded. In other words, the dimensions change the most in the direction of anisotropy induced by parameter $\boldsymbol{\Delta}$. Bear in mind that results in one column depict the same moment in time but for different values of α and $\boldsymbol{\Delta}$. Therefore, a conclusion can be drawn that these parameters also affect the intensity and extent of viscoplastic deformation, indicated by the size and spatial distribution of the red zones.

Finally, in Figs. 4.20 and 4.21, the distributions of temperature and the current yield shear strength were presented. It can be observed that the fractional parameters have a significant impact on these state variables as well. Also, these results provide another evidence for the thermo-mechanical coupling in the fractional viscoplastic model.

4.6. Conclusions

In this section, the fractional viscoplastic model, which takes into account thermal and microdamage effects, was explored. This constitutive formulation considers thermal

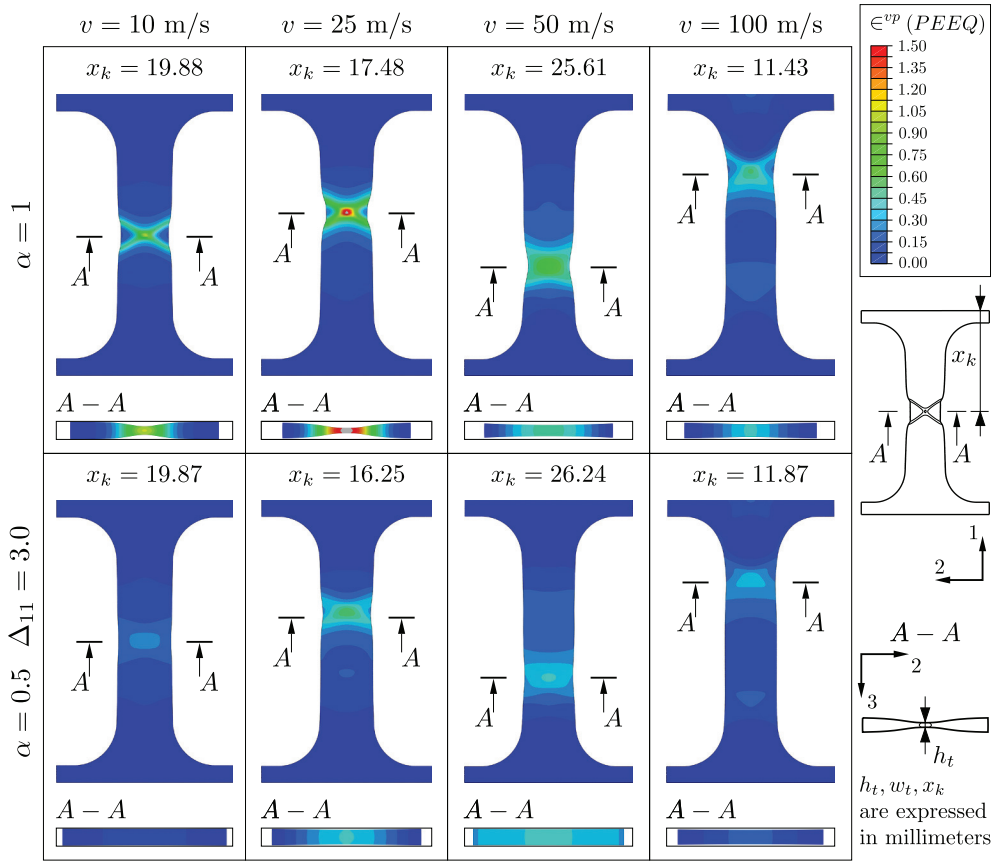

Figure 4.16. Deformation of the dog-bone specimen under various loading conditions for: classical viscoplasticity ($\alpha = 1$) and induced viscoplastic flow in the direction (1) [201]

softening, strain-rate hardening, work-induced hardening/softening and porosity-based failure criterion. Next, the implementation and numerical algorithm for fractional viscoplasticity were thoroughly discussed. The dynamic response of this new material model was examined for a dog-bone specimen in a series of numerical tensile tests. In the first part, the coupling between mechanical and thermal fields was studied. This was conducted for a specimen before and after the critical damage in the material occurred. Next, the evolution of state variables in 20 different points was examined. Finally, the localization of damaged elements and development of microdamage parameter was investigated. In the second part, the results for various velocities and four sets of fractional parameters were combined in order to examine deformation anisotropy, formation of necking and shear bands, as well as the localization of damaged region.

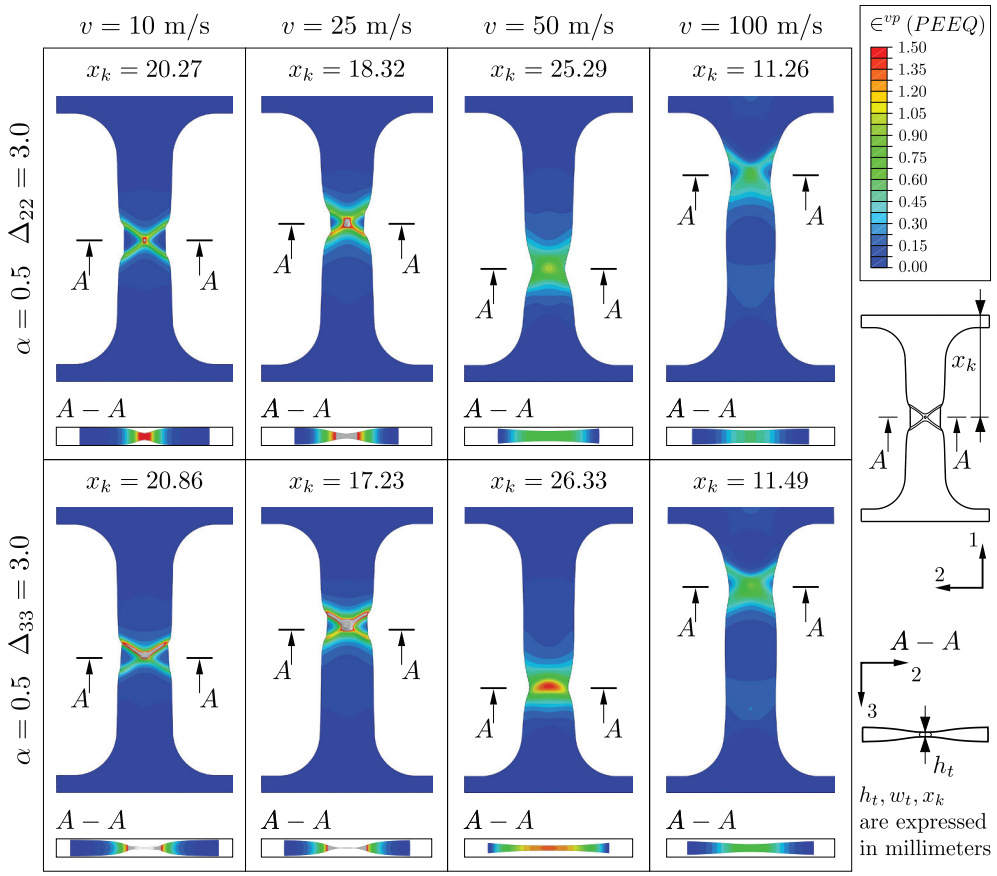

Figure 4.17. Deformation of the dog-bone specimen under various loading conditions for: induced viscoplastic flow in the direction (2) and (3) [201]

The main conclusions from the studies are:

- In fractional viscoplasticity, the thermo-mechanical coupling can be observed among ϑ, $\in^{vp}$ and ξ.
- Non-uniform distribution of the current yield shear strength, denoted by κ, results from a combination of work hardening with thermal and microdamage softening.
- For some material points, there is no evolution of the microdamage parameter ξ. In such cases, degradation of the material strength is solely caused by thermal softening.
- Strain-rate hardening is responsible for the decrease in the level of viscoplastic strain and diminished evolution of shear bands.

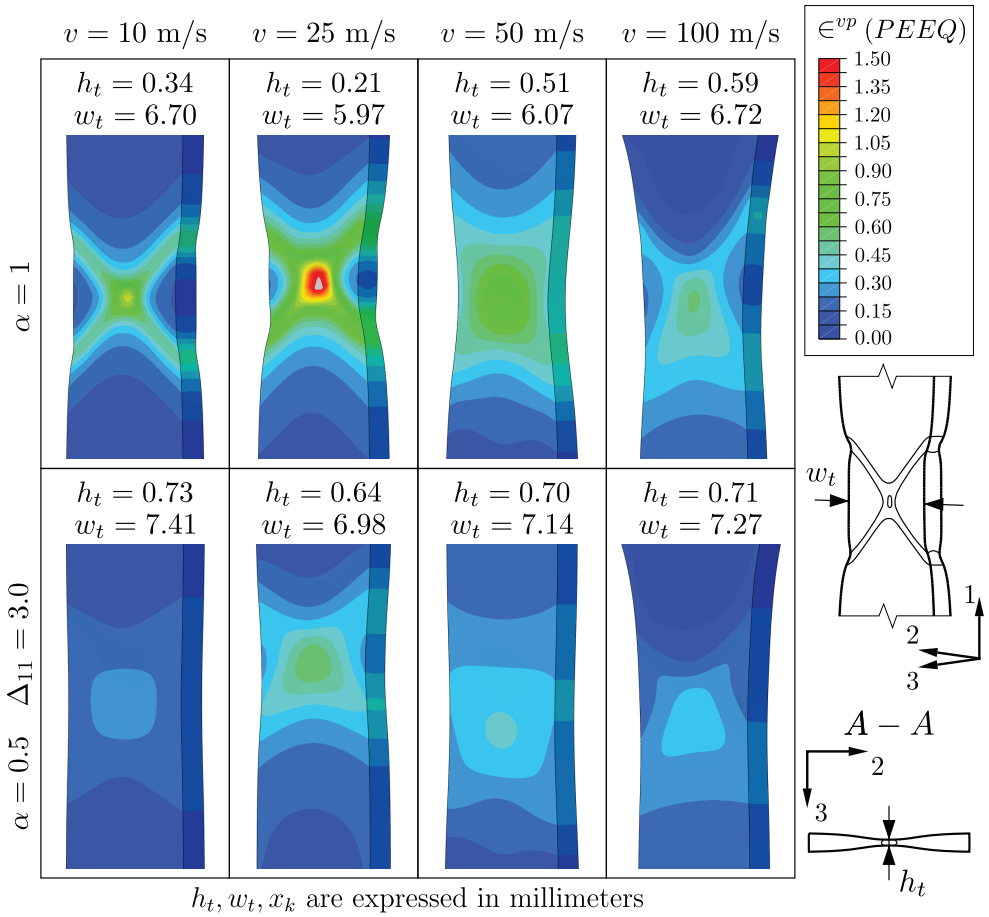

Figure 4.18. Detailed view of the viscoplastic strain localization (focus from Fig. 4.16) along with the dimensions of the deformation zone [201]

- Fractional parameters, α and $\boldsymbol{\Delta}$, are responsible for inducing anisotropy in the deformation process.
- Directional dependence, controlled by the α and $\boldsymbol{\Delta}$, affects the level of viscoplastic strain ($\in^{vp}$) as well as dimensions and shape of the deformed zone.
- The evolution and form of X-shaped shear bands strongly depend on the direction of the $\boldsymbol{\Delta}$ parameter.
- The development of shear bands in the framework of fractional viscoplasticity is a result of dispersive and dissipative qualities of the material model, which leads to spontaneous strain localization. Conversely, in the rate-independent plasticity

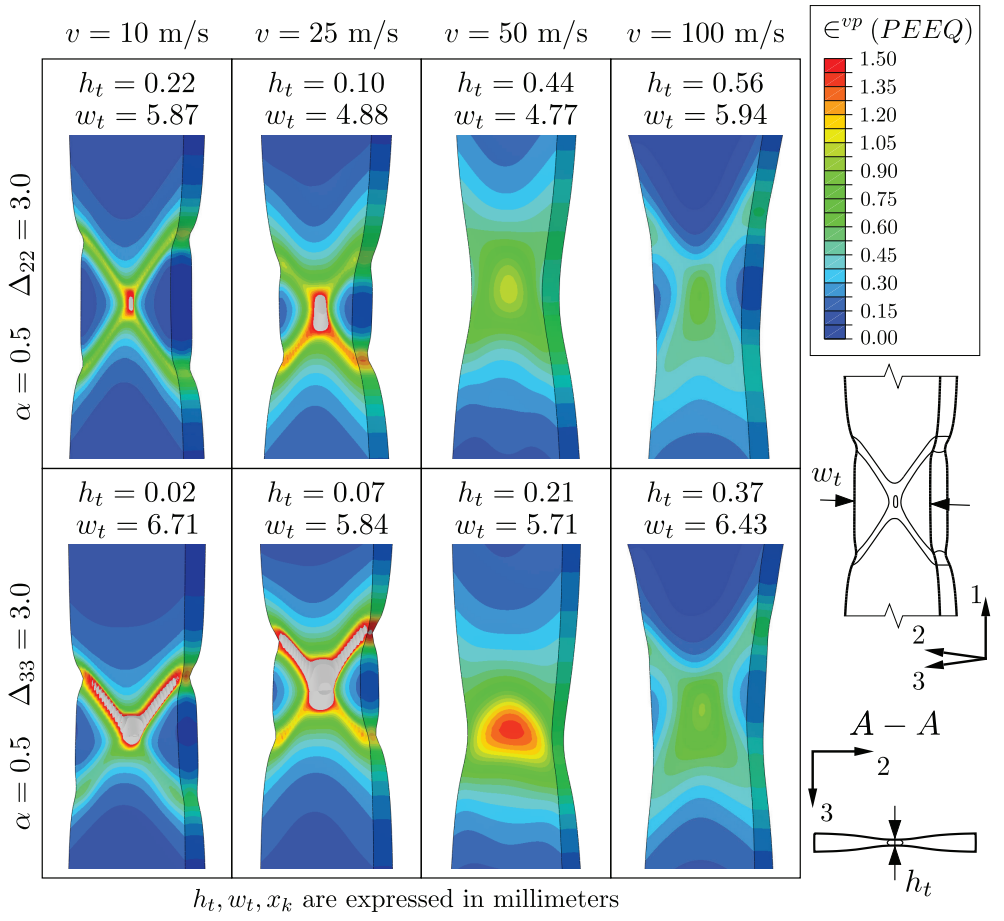

Figure 4.19. Detailed view of the viscoplastic strain localization (focus from Fig. 4.17) along with the dimensions of the deformation zone [201]

geometrical imperfections have to be introduced to the numerical model otherwise, the homogeneous deformation would advance without the formation of shear bands [154].

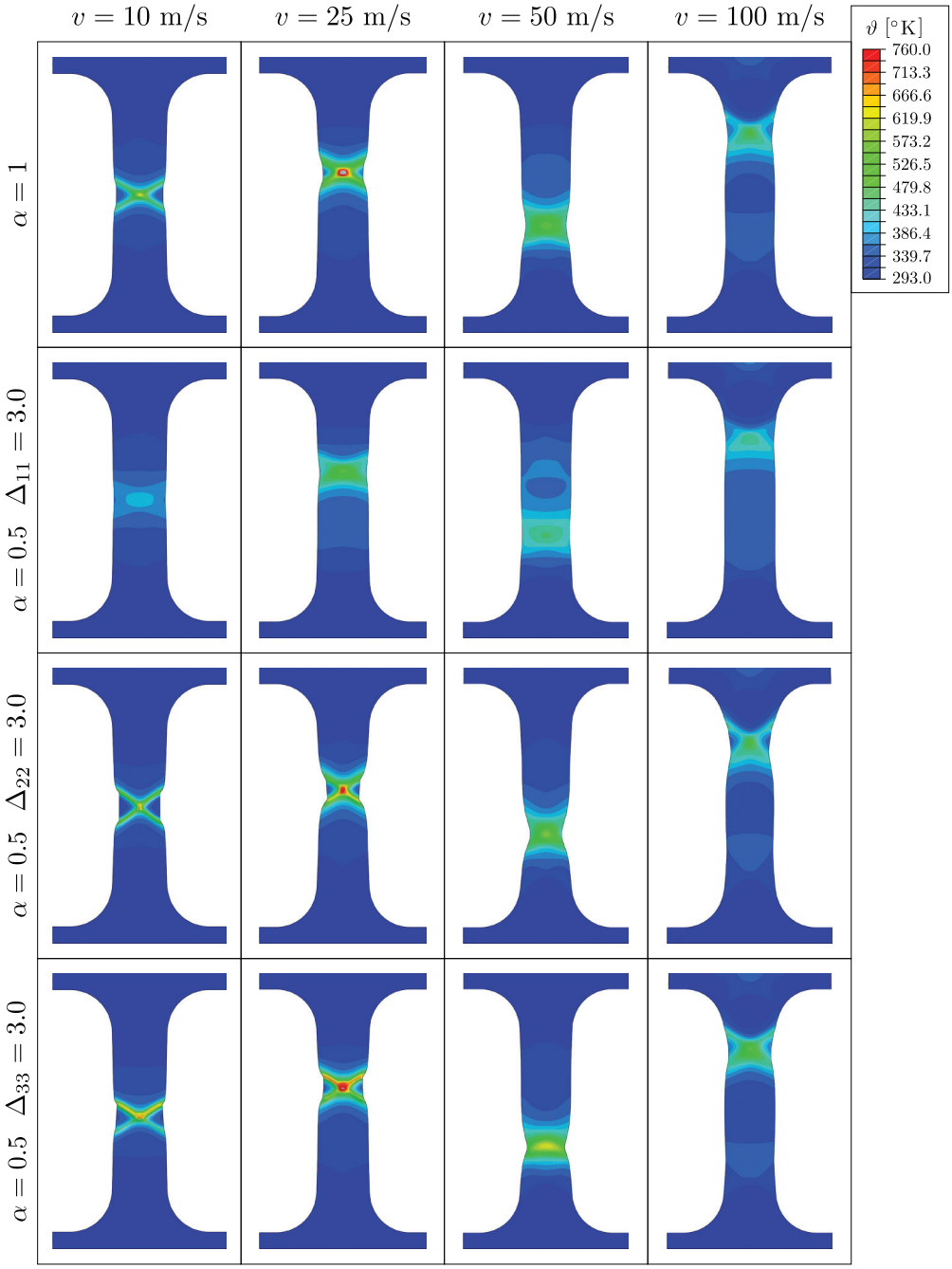

Figure 4.20. Temperature distribution as a function of the fractional parameters and the tension velocity

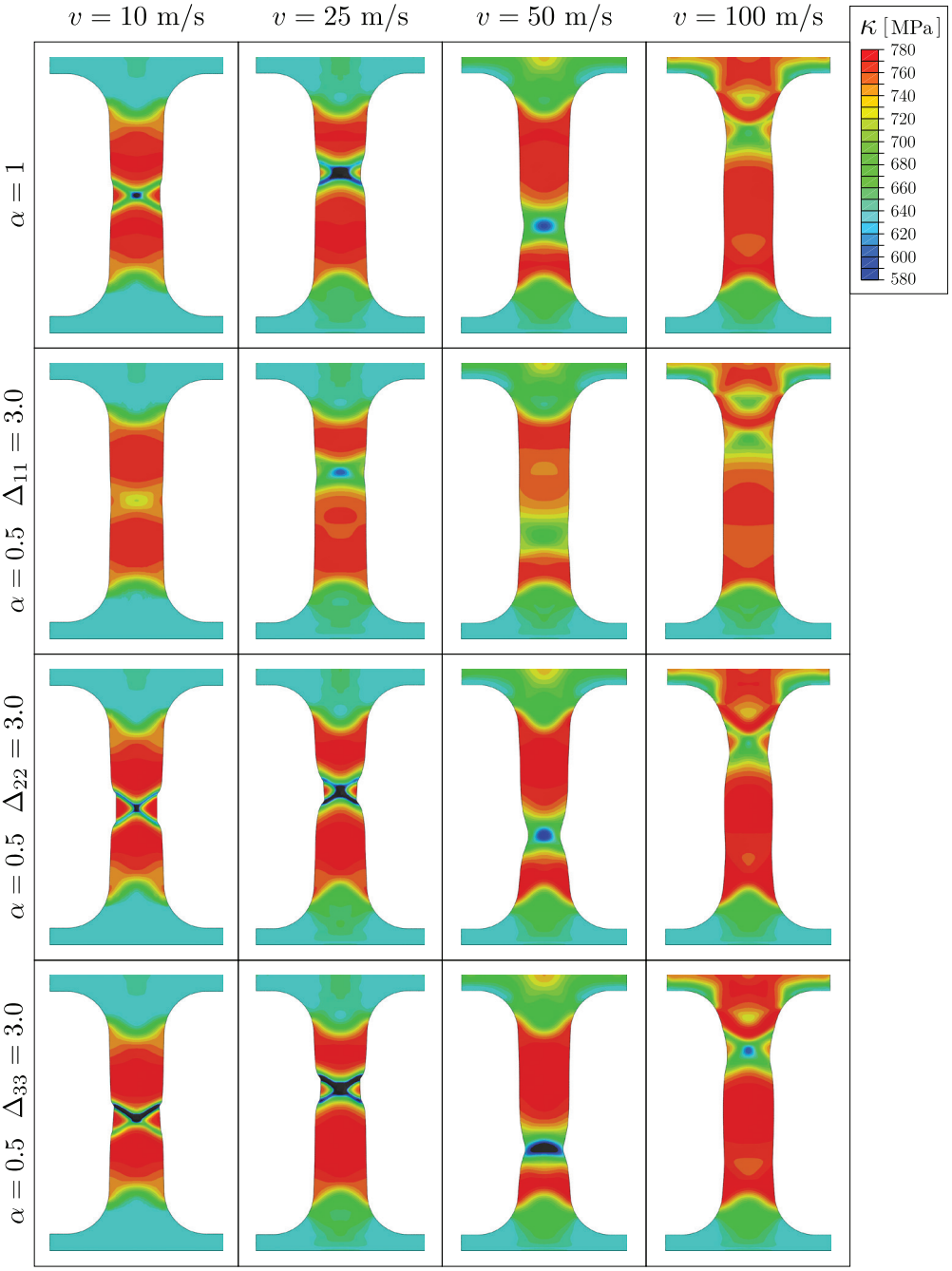

Figure 4.21. Current yield shear strength as a function of the fractional parameters and the tension velocity

Chapter 5

Conclusion and future work

5.1. Introduction

In this final chapter conclusions along with recommendations for possible directions for future work are provided. These conclusions are based upon the numerical simulations conducted in chapters 3 and 4 of this treatise.

5.2. General conclusions

The main objective of the research presented in this treatise was to study how the application of fractional derivative affects the dynamic behavior of elastic-viscoplastic material model. Given that the fractional viscoplasticity is a relatively new concept, this was the first such extensive research on this subject. Numerous authors have demonstrated in the literature that fractional generalization gives rise to non-local properties in the material. Regarding viscoplasticity, it manifested itself in the non-normality of viscoplastic flow and induced anisotropy. The proposed model has the potential to be a reliable and flexible tool to analyse dynamic material behaviour in the field of civil engineering. Specifically, when the dynamic response of construction to blast loading is being considered. Also, the abrupt loss of load-bearing capacity due to the structural failure could be analysed using fractional viscoplasticity.

Chapter 3 began with a terse introduction to the fractional calculus with a particular focus on Riesz-Caputo fractional derivative. Next, the basic equations of elastic-viscoplastic formulation were given. To this point, classical Perzyna-type viscoplasticity was being considered, which postulated the associated flow rule. Next, the application of the fractional operator to viscoplasticity was presented. It was followed by a demonstration of the numerical implementation and the numerical procedure for obtaining an approximate solution.

Original results presented in this chapter were divided into two groups to clearly separate the impact of the rate-dependent (viscous) and non-local (fractional) parameters. The dynamic response of the material was studied for an elementary cube under uniaxial loading. The first part of the investigation was focused on the impact of the derivative order α and the $\boldsymbol{\Delta}$ parameter. Both parameters allow to controlling the level of stress wave oscillations. Moreover, when the $\boldsymbol{\Delta}$ is modified in the direction perpendicular to the applied load, an induced anisotropy is observed, for different values of α. The directional properties also affect the strain-rate hardening, which was observed for different values of the order of the fractional differentiation operator.

The second group of analysis concerned the relaxation time T_m and the rate-sensitivity parameter m. Their influence was studied for fixed values of fractional parameters and three different velocities of the applied displacement fields. It was observed that both T_m and m control the dynamic response of the material. In particular, they impact the amplitude of the oscillations and the level of anisotropy, as well as the degree of the strain-rate hardening. Another important finding was that the level of stress, in relation to the classical viscoplastic formulation, depended on the direction of $\boldsymbol{\Delta}$. This relation hinted that anisotropy can be also manifested in the inelastic dissipation of mechanical wave energy.

The last series of analysis was directed towards examining the foregoing phenomena. The frequency of the mechanical wave was the basis for this investigation. It was found that the anisotropy is observed for various $\boldsymbol{\Delta}$ parameters. Therefore, the direction of energy dissipation can be also controlled in the new fractional model.

In chapter 4, the fractional viscoplastic model was extended with temperature ϑ, intrinsic volume porosity ξ and work-hardening/softening strength parameter κ. Additionally, a fracture criterion was introduced based on the evolution of the internal state variable ξ, which takes into account the microdamage effects. For clarity's sake, the full set of equations has been presented with the implementation details. The numerical investigations, presented in this chapter, used a finite element model of a dog-bone specimen dynamically loaded in the uniaxial tensile tests. Much attention was paid to FEM mesh generation and its density. To capture any effects that may appear in the cross-section of the material, 8 solid elements were used through the specimen thickness.

The first part of the study was conducted in order to analyze the relationship between different thermo-mechanical fields. Areas, where the inelastic strain and temperature peaked, were localized within the necking of the specimen. The maximum value of the damage parameter ξ also was concentrated in this same place. Interestingly, the value of κ presented great variability over the entire length of the dog-bone sample. As expected the damage occurred in the place where the rapid evolution of porosity was previously observed.

An in-depth examination of the state variables during deformation was conducted for 20 selected points, placed both on the surface and inside the specimen. It was found

that the evolution of internal fields strongly depends on its location in relation to the necking zone. The increase of temperature initiates material softening, but the rapid degradation in material strength occurs when the value of the microdamage parameter starts to grow. In was also shown that fracture in material starts in the area where the strain is concentrated and then progress from the specimen center to its edges.

Next, the parametric study focused on the influence of the fractional parameter ($\mathbf{\Delta}$) on the deformation mechanism for various velocities of displacement fields was conducted. It can be observed that deformation is intensified in the direction that corresponds to the direction of $\mathbf{\Delta}$. Also, the strain-rate hardening can be recognized since the level of $\in^{vp}$ decreases as the velocity of the load grows. Conversely, the maximum value and spatial distribution of $\in^{vp}$ is strongly affected by the value of $\mathbf{\Delta}$. This induced anisotropy, resulting from the fractional approach, is also visible in the cross-sectional views of the specimen. Moreover, the intensity of viscoplastic deformation is indicated by the size and spatial distribution of the shear bands.

This study set out to determine various effects that result from the fractional derivative application to the elastic-viscoplastic material model. It was shown that this approach induces anisotropy in material inelastic deformation and energy dissipation. New parameters, α and $\mathbf{\Delta}$, control the dynamic response of the material by affecting the strain-rate hardening, viscoplastic strain and material degradation upon the moment of failure. This is all done with only two new material parameters without the need to identify material constants again. Fractional viscoplasticity has the potential to aid in solving problems in civil engineering that require the knowledge of the dynamic behaviour of metal structures. The successful implementation of this model provides access to a flexible tool for designing and analyzing structures.

The fulfilment of the objectives stated in the chapter 1 is summarized in the following points:

1. Numerical procedure accounting for the thermal and mechanical effects of deformation was created and used in chapter 4 to study induced anisotropy resulting from the fractional framework. Also, this code was use to analyse thermal and mechanical fields in the dynamical tests. The implemented fracture criterion, based on the growth of porosity, was instrumental in showing the relation between the inelastic strain localization and material damage evolution.

2. A finite element model was developed for investigations at the material point level. The dynamic response of this cube element was governed by the viscoplastic strain rate generalized in the framework of fractional calculus. No thermal nor micromechanical effects were implemented here, cf. [200].

3. A full 3-D finite model of a dog-bone specimen was devised to give further insight into the generalized elastic-viscoplastic formulation. The finite mesh was partitioned to ensure a smooth transition between straight and curved parts of the dog-bone specimen, which in turn resulted in a better quality mesh. Eight solid elements

through the specimen thickness, were used to study the effects of anisotropy that originate from the fractional solution.

4. The relation between material parameters and dispersion of mechanical waves was studied in section 3.3.3. Results obtained at the material point level show that fractional parameters, i.e. α and $\mathbf{\Delta}$, have an impact on energy dissipation observed as a change of the wave frequency. Therefore, the induced anisotropy exhibits itself in viscoplastic deformation as well as the wave propagation. The further numerical analysis revealed the relationship between relaxation time T_m and wave frequency in the loading direction.

5. Research into the impact of fractional and viscous parameters was conducted and discussed in chapter 3. It was found that fractional parameters affect the rate-dependent hardening and the characteristics of the mechanical wave, as well as the induced viscoplastic anisotropy, which was also observed. Anisotropy results in a direction-dependent change of dimensions and trajectory of the stress-strain curve. The relaxation time (T_m) and strain-rate sensitivity (m) have impact on stress wave propagation and material hardening.

6. An investigation of the deformation and the state variables in the full 3-D model was presented in chapter 4. As anticipated, the strain localization was observed in various modes which were strongly dependent on the order of the fractional derivative (α) and the fractional direction ($\mathbf{\Delta}$). The evolution and the dimensions of X-shaped bands, as well as the level of viscoplastic strain $\in^{vp}$, were strongly affected by the foregoing parameters. It was also observed that strain-rate hardening was a significant factor in the inhibition of shear band formation.

7. Thermo-mechanical coupling among ϑ, ξ and $\in^{vp}$ was observed in the obtained results. The intense evolution of these state variables was to concentrated in the necking zone. The distribution of κ was not uniform on the specimen surface, displaying regions of increased and decreased strength. This can be attributed to the combination of work hardening and softening, which stems from thermal and microdamage effects. Detailed investigation of state variables during deformation revealed that in regions where there is no evolution of microdamage parameter ξ, only thermal softening occurs.

8. In conclusion, the results reflect the one obtained in the available experimental studies.

Taking into account the achieved objectives, it can be asserted that the thesis of this dissertation (section 1.3), which stated that *the fractional formulation of the viscoplastic model improves the description of metals behaviour under dynamic loading*, is correct.

5.3. Future work

The work presented in this treatise can be extended in the following ways.

1. Extend the definition of the fractional viscoplasticity to the large strain theory. Further study should answer the question if this path is possible and what sort of results it could yield.

2. Confirm the applicability of fractional approach by comparing numerical results with experimental data. A detailed research report where the measurement points were unequivocally marked is a logical candidate for studying this type of correlation. Moreover, the data would have to come from a dynamic test where high strain rates could be achieved.

3. Use fractional viscoplasticity in the modelling large scale structural elements common in civil engineering. While this application does not pose significant challenges in the field of computational mechanics, it could be a helpful tool in designing structures that have to withstand a dynamic loading.

4. Develop a numerical procedure to identify material parameters associated with the fractional formulation, i.e. α and $\mathbf{\Delta}$. This would require a mixed approach where the identification procedure is combined with the processing images from multiple cameras. The properly built system could capture, analyze and transform data about deformation anisotropy into material parameters.

Bibliography

[1] R. K. Abu Al-Rub and G. Z. Voyiadjis. Gradient-enhanced coupled plasticity-anisotropic damage model for concrete fracture: Computational aspects and applications. *International Journal of Damage Mechanics*, 18(2):115–154, 2009. [cited at p. 4]

[2] O. P. Agrawal. Generalized variational problems and Euler-Lagrange equations. *Computers and Mathematics with Applications*, 59(5):1852–1864, 2010. Fractional Differentiation and Its Applications. [cited at p. 35]

[3] E. C. Aifantis. On the role of gradients in the localization of deformation and fracture. *International Journal of Engineering Science*, 30(10):1279–1299, 1992. [cited at p. 4]

[4] V. Alastrue, M. A. Martínez, M. Doblare, and A. Menzel. Anisotropic micro-sphere-based finite elasticity applied to blood vessel modelling. *Journal of the Mechanics and Physics of Solids*, 57(1):178–203, 2009. [cited at p. 4]

[5] L. Anand and W. A. Spitzig. Initiation of localized shear bands in plane strain. *Journal of the Mechanics and Physics of Solids*, 28(2):113–128, 1980. [cited at p. 5]

[6] A. Anandarajah and Y. F. Dafalias. Bounding surface plasticity. III: Application to anisotropic cohesive soils. *Journal of Engineering Mechanics – ASCE*, 112(12):1292–1318, 1986. [cited at p. 3]

[7] K. Assaleh and W. M. Ahmad. Modeling of speech signals using fractional calculus. In *2007 9th International Symposium on Signal Processing and Its Applications*, pages 1–4. IEEE, 2007. [cited at p. 7]

[8] R. L. Bagley and J. Torvik. Fractional calculus-a different approach to the analysis of viscoelastically damped structures. *AIAA Journal*, 21(5):741–748, 1983. [cited at p. 7]

[9] R. L. Bagley and P. J. Torvik. A theoretical basis for the application of fractional calculus to viscoelasticity. *Journal of Rheology*, 27:201–210, 1983. [cited at p. 7]

[10] F. Barlat, D. J. Lege, and J. C. Brem. A six-component yield function for anisotropic materials. *International Journal of Plasticity*, 7:693–712, 1991. [cited at p. 3]

[11] K. J. Bathe. *Finite element procedures*. Klaus-Jurgen Bathe, 2006. [cited at p. 28]

[12] Z. P. Bazant and S. S. Kim. Plastic-fracturing theory for concrete. *Journal of the Engineering Mechanics Division*, 105(3):407–428, 1979. [cited at p. 4]

[13] D. Bigoni and T. Hueckel. A note on strain localization for a class of non-associative plasticity rules. *Ingenieur-Archiv*, 60:491–499, 1990. [cited at p. 4]

[14] T. Błaszczyk and M. Ciesielski. Fractional Euler-Lagrange equations-numerical solutions and applications of reflection operator. *Scientific Research of the Institute of Mathematics and Computer Science*, 9(2):17–24, 2010. [cited at p. 7]

[15] J. Bobiński and J. Tejchman. Numerical simulations of localization of deformation in quasi-brittle materials within non-local softening plasticity. *Computers and Concrete*, 1(4):433–455, 11 2004. [cited at p. 4]

[16] T. Błaszczyk. Analytical and numerical solution of the fractional Euler–Bernoulli beam equation. *Journal of Mechanics of Materials and Structures*, 12(1):23–34, 2016. [cited at p. 7]

[17] T. Błaszczyk and M. Ciesielski. Numerical solution of Euler-Lagrange equation with caputo derivatives. *Advances in Applied Mathematics and Mechanics*, 9(1):173–185, 2017. [cited at p. 7]

[18] A. K. Chakrabarti and J. W. Spretnak. Instability of plastic flow in the directions of pure shear: I. theory. *Metallurgical Transactions A*, 6(4):733, Apr 1975. [cited at p. 60, 63, 65, 66]

[19] Y. W. Chang and R. J. Asaro. An experimental study of shear localization in aluminum-copper single crystals. *Acta Metallurgica*, 29(1):241–257, 1981. [cited at p. 5]

[20] E. P Chen. Non-local effects on dynamic damage accumulation in brittle solids. *International journal for numerical and analytical methods in geomechanics*, 23(1):1–21, 1999. [cited at p. 4]

[21] I. W. Chen and P. E. Reyes-Morel. Implications of transformation plasticity in ZrO_2 -containing ceramics: I, shear and dilatation effects. *Journal of the American Ceramic Society*, 69(3):181–189, 1986. [cited at p. 3]

[22] J. Clausen, L. Damkilde, and L. Andersen. An efficient return algorithm for non-associated plasticity with linear yield criteria in principal stress space. *Computers & Structures*, 85(23-24):1795–1807, 2007. [cited at p. 4]

[23] R. J. Clifton, J. Duffy, K. A. Hartley, and T. G. Shawki. On critical conditions for shear band formation at high strain rates. *Scripta Metallurgica*, 18(5):443–448, 1984. [cited at p. 5]

[24] B. D. Coleman and M. L. Hodgdon. On shear bands in ductile materials. In *Analysis and Thermomechanics*, pages 227–255. Springer, 1987. [cited at p. 5]

[25] J. W. Craggs. The propagation of infinitesimal plane waves in elastic-plastic materials. *Journal of the Mechanics and Physics of Solids*, 5(2):115–124, 1957. [cited at p. 5]

[26] S. Cuenot, S. Demoustier-Champagne, and B. Nysten. Elastic modulus of polypyrrole nanotubes. *Physical Review Letters*, 85(8):1690–1693, 2000. [cited at p. 4]

[27] R. S. Culver. Thermal instability strain in dynamic plastic deformation. In *Metallurgical effects at high strain rates*, pages 519–530. Springer, 1973. [cited at p. 5]

[28] V. Cvitanić, F. Vlak, and Ž. Lozina. A finite element formulation based on non-associated plasticity for sheet metal forming. *International Journal of Plasticity*, 24(4):646–687, 2008. [cited at p. 4]

[29] Y. F. Dafalias. Elasto-plastic coupling within a thermodynamic strain space formulation of plasticity. *International Journal of Non-Linear Mechanics*, 12(5):327–337, 1977. [cited at p. 4]

[30] M. Dao and R. J. Asaro. Non-schmid effects and localized plastic flow in intermetallic alloys. *Materials Science and Engineering: A*, 170(1-2):143–160, 1993. [cited at p. 3, 4, 42]

[31] R. De Borst. Integration of plasticity equations for singular yield functions. *Computers & structures*, 26(5):823–829, 1987. [cited at p. 4]

[32] R. De Borst, M. A. Crisfield, J. J. C. Remmers, and C. V. Verhoosel. *Nonlinear finite element analysis of solids and structures*. John Wiley & Sons, 2012. [cited at p. 28]

[33] E. A. de Souza Neto, D. Peric, and D. R. J. Owen. *Computational Methods for Plasticity: Theory and Applications*. Wiley, 2011. [cited at p. 7, 27, 47]

[34] W. Derski, R. Izbicki, I. Kisiel, and Z. Mróz. *Rock and Soil Mechanics*. PWN-Polish Scientific Publishers, Warszawa, 1988. [cited at p. 3]

[35] O. W. Dillon and J. Kratochvil. A strain gradient theory of plasticity. *International Journal of Solids and Structures*, 6(12):1513–1533, 1970. [cited at p. 4]

[36] B. Dodd and Y. Bai. *Adiabatic shear localization: frontiers and advances*. Elsevier, 2012. [cited at p. 6]

[37] R. Dormeval. Adiabatic shear phenomena. *DGM Informationsgesellschaft mbH, Impact Loading and Dynamic Behavior of Materials.*, 1:43–56, 1988. [cited at p. 5]

[38] W. Dornowski. *Numeryczna symulacja procesów plastycznego płynięcia przy dynamicznych obciążeniach cyklicznych*. Military University of Technology, 1999. (D. Sc. Thesis – in Polish). [cited at p. 60]

[39] W. Dornowski and P. Perzyna. Analysis of various effects in dynamic cyclic fatigue damage. *Archive of Applied Mechanics*, 72:418–438, 01 2002. [cited at p. 6, 60]

[40] W. Dornowski and P. Perzyna. Localized fracture phenomena in thermo-viscoplastic flow process under cyclic dynamic loadings. *Acta Mechanica*, 155:233–255, 2002. [cited at p. 6, 60]

[41] W. Dornowski and P. Perzyna. Numerical analysis of macrocrack propagation along a bimaterial interface under dynamic loading processes. *International Journal of Solids and Structures*, 39:4949–4977, 2002. [cited at p. 6, 60]

[42] W. Dornowski and P. Perzyna. Investigation of macrocrack propagation along a bimaterial interface in adiabatic dynamic processes as a problem of mesomechanics. *Engineering Transactions*, 54(4), 2006. [cited at p. 61, 66, 67]

[43] W. Dornowski and P. Perzyna. Numerical investigation of localized fracture phenomena in inelastic solids. *Foundations of Civil and Environmental Engineering*, 7:79–116, 2006. [cited at p. 6, 40]

[44] A. Drescher and E. Detournay. Limit load in translational failure mechanisms for associative and non-associative materials. *Géotechnique*, 43(3):443–456, 1993. [cited at p. 3]

[45] B. Dumitru, D. Kai, and S. Enrico. *Fractional Calculus: Models and Numerical Methods*. Series on Complexity, Nonlinearity and Chaos. World Scientific Publishing Company, 2012. [cited at p. 7]

[46] M. K. Duszek–Perzyna and P. Perzyna. Analysis of the influence of different effects on criteria for adiabatic shear band localization in inelastic solids. *Archive of Applied Mechanics*, 50, 1994. [cited at p. 60]

[47] A. C. Eringen. Linear theory of micropolar elasticity. *Journal of Mathematics and Mechanics*, pages 909–923, 1966. [cited at p. 4]

[48] A. C. Eringen. *Mechanics of Continua*. J. Wiley & Sons, New York, 1967. [cited at p. 4]

[49] A. C. Eringen. *Nonlocal continuum field theories*. Springer Science & Business Media, 2002. [cited at p. 4]

[50] D. C. Erlich, L. Seaman, D. A. Shockey, and D. R. Curran. Development and application of a computational shear band model. Technical report, SRI International, Menlo Park, CA, 1980. [cited at p. 5]

[51] Z. E. A. Fellah, J. Y. Chapelon, S. Berger, W. Lauriks, and C. Depollier. Ultrasonic wave propagation in human cancellous bone: Application of biot theory. *The Journal of the Acoustical Society of America*, 116(1):61–73, 2004. [cited at p. 7]

[52] Z. E. A. Fellah, C. Depollier, and M. Fellah. Application of fractional calculus to the sound waves propagation in rigid porous materials: Validation via ultrasonic measurements. *Acta Acustica United with Acustica*, 88(1):34–39, 2002. [cited at p. 7]

[53] Y. Ferdi. Computation of fractional order derivative and integral via power series expansion and signal modelling. *Nonlinear Dynamics*, 46(1-2):1–15, 2006. [cited at p. 7]

[54] N. A. Fleck and J. W. Hutchinson. Strain gradient plasticity. *Advances in Applied Mechanics*, 33:295–361, 1997. [cited at p. 4]

[55] G. S. F. Frederico and D. F. M. Torres. Fractional Noether's theorem in the Riesz – Caputo sense. *Applied Mathematics and Computation*, 217:1023–1033, 2010. [cited at p. 37]

[56] A. Gajo, D. Bigoni, and D. M. Wood. Multiple shear band development and related instabilities in granular materials. *Journal of the Mechanics and Physics of Solids*, 52:2683–2724, 2004. [cited at p. 3]

[57] B. G. Galerkin. Series solution of some problems of elastic equilibrium of rods and plates. *Vestnik Inzhenerov i Tekhnikov*, 19:897–908, 1915. [cited at p. 30]

[58] X. Gao, T. Zhang, J. Zhou, S. M. Graham, M. Hayden, and C. Roe. On stress-state dependent plasticity modeling: significance of the hydrostatic stress, the third invariant of stress deviator and the non-associated flow rule. *International Journal of Plasticity*, 27(2):217–231, 2011. [cited at p. 4]

[59] M. G. D. Geers. *Experimental analysis and computational modelling of damage and fracture*. Eindhoven University of Technology, Eindhoven, 1997. [cited at p. 4]

[60] N. Germain, J. Besson, and F. Feyel. Composite layered materials: Anisotropic nonlocal damage models. *Computer Methods in Applied Mechanics and Engineering*, 196(41-44):4272–4282, 2007. [cited at p. 4]

[61] A. Glema. *Analiza natury falowej zjawiska lokalizacji*. Rozprawy nr 379. Wydawnictwo Politechniki Poznańskiej, Poznań, 2004. [cited at p. 6]

[62] A. Glema, W. Kąkol, and T. Łodygowski. Numerical modelling of adiabatic shear band formation in a twisting test. *Engineering Transactions*, 45(3-4):419–431, 1997. [cited at p. 6]

[63] A. Glema and T. Łodygowski. On importance of imperfections in plastic strain localization problems in materials under impact loading. *Archives of Mechanics*, 54(5-6):411–423, 2002. [cited at p. 6]

[64] A. Glema, T. Łodygowski, and P. Perzyna. Interaction of deformation waves and localization phenomena in inelastic solids. *Computer Methods in Applied Mechanics and Engineering*, 183:123–140, 2000. [cited at p. 6]

[65] A. Glema, T. Łodygowski, and P. Perzyna. Localization of plastic deformations as a result of wave interaction. *Computer Assisted Mechanics and Engineering Sciences*, 10(1):81–91, 2003. [cited at p. 6]

[66] A. Glema, T. Łodygowski, and W. Sumelka. Nowacki's double shear test in the framework of the anisotropic thermo-elasto-vicsoplastic material model. *Journal of Theoretical and Applied Mechanics*, 48(4):973–1001, 2010. [cited at p. 4]

[67] A. Glema, T. Łodygowski, W. Sumelka, and P. Perzyna. The numerical analysis of the intrinsic anisotropic microdamage evolution in elasto-viscoplastic solids. *International Journal of Damage Mechanics*, 18(3):205–231, 2009. [cited at p. 6, 7]

[68] R. Gorenflo and F. Mainardi. Fractional calculus. In *Fractals and fractional calculus in continuum mechanics*, pages 223–276. Springer, 1997. [cited at p. 7]

[69] D. E. Grady. Dissipation in adiabatic shear bands. *Mechanics of Materials*, 17(2-3):289–293, 1994. [cited at p. 6]

[70] R. J. Green. A plasticity theory for porous solids. *International Journal of Mechanical Sciences*, 14(4):215–224, 1972. [cited at p. 61]

[71] M. E. Gurtin and A. I. Murdoch. A continuum theory of elastic material surfaces. *Archive for Rational Mechanics and Analysis*, 57(4):291–323, 1975. [cited at p. 4]

[72] K. A. Hartley, J. Duffy, and R. H. Hawley. Measurement of the temperature profile during shear band formation in steels deforming at high strain rates. *Journal of the Mechanics and Physics of Solids*, 35(3):283–301, 1987. [cited at p. 5]

[73] H. Hencky. Zur Theorie plastischer Deformationen und der Hierdurch im Material hervorgerufenen Nachspannungen. *ZAMM – Journal of Applied Mathematics and Mechanics / Zeitschrift für Angewandte Mathematik und Mechanik*, 4(4):323–334, 1924. [cited at p. 39]

[74] R. Hilfer. *Applications of fractional calculus in physics*. World scientific, 2000. [cited at p. 7]

[75] R. Hill. A theory of the yielding and plastic fow of anisotropic metals. *Proceedings of the Royal Society A*, 193:281–297, 1948. [cited at p. 3]

[76] R. Hill. Acceleration waves in solids. *Journal of the Mechanics and Physics of Solids*, 10(1):1–16, 1962. [cited at p. 5]

[77] R. Hill. *The Mathematical Theory of Plasticity*, volume 11. Oxford university press, 1998. [cited at p. 39]

[78] K. Hohenemser and W. Prager. Fundamental equations and definitions concerning the mechanics of isotropic continua. *Journal of Rheology*, 3(16), 1932. [cited at p. 38]

[79] G. A. Holzapfel. *Nonlinear Solid Mechanics – A Continuum Approach for Engineering*. Wiley, 2000. [cited at p. 13]

[80] H. T. Hu and W. C. Schnobrich. Constitutive modeling of concrete by using nonassociated plasticity. *Journal of Materials in Civil Engineering – ASCE*, 1(4):199–216, 1989. [cited at p. 3]

[81] M. T. Huber. Właściwa praca odkształcenia jako miara wytężenia materyału. *Czasopismo Techniczne, Lwów*, 15, 1904. [cited at p. 39]

[82] D. A. Hughes, Q. Liu, D. C. Chrzan, and N. Hansen. Scaling of microstructural parameters: Misorientations of deformation induced boundaries. *Acta Materialia*, **45**(1):105–112, 1997. [cited at p. 3, 42]

[83] T. J. R. Hughes. *The finite element method: linear static and dynamic finite element analysis*. Courier Corporation, 2012. [cited at p. 30]

[84] J. W. Hutchinson and K. W. Neale. Influence of strain-rate sensitivity on necking under uniaxial tension. *Acta Metallurgica*, 25(8):839–846, 1977. [cited at p. 5]

[85] T. Iwakuma and S. Nemat-Nasser. An analytical estimate of shear band initiation in a necked bar. *International Journal of Solids and Structures*, 18(1):69–83, 1982. [cited at p. 5]

[86] S. Jemioło and M. Kwieciński. A new concept of the non-associative plastic flow. In J. P. Boehler and A. S. Khan, editors, *Anisotropy and Localization of Plastic Deformation*, chapter A New Concept of the Non-Associative Plastic Flow. Springer, 1991. pages 217–220. [cited at p. 3]

[87] B. Ji and W. Chen. A new analytical solution of pure bending beam in couple stress elastoplasticity: Theory and applications. *International Journal of Solids and Structures*, 47:779–785, 2010. [cited at p. 4]

[88] D. Jia, Y. M. Wang, K. T. Ramesh, E. Ma, Y. T. Zhu, and R. Z. Valiev. Deformation behavior and plastic instabilities of ultrafine-grain titanium. *Applied Physics Letters*, 79:611–613, 2001. [cited at p. 63, 65]

[89] J. Jiang, H. I. Ling, and V. N. Kaliakin. An associative and non-associative anisotropic bounding surface model for clay. *Journal of Applied Mechanics ASME*, 79:031010, 2012. [cited at p. 3]

[90] J. N. Johnson. Dynamic fracture and spallation in ductile solids. *Journal of Applied Physics*, 52(4):2812–2825, 1981. [cited at p. 60]

[91] W. Johnson. Henri Tresca as the originator of adiabatic heat lines. *International Journal of Mechanical Sciences*, 29(5):301–310, 1987. [cited at p. 5]

[92] A. A. Kilbas, H. M. Srivastava, and J. J. Trujillo. *Theory and Applications of Fractional Differential Equations*. Elsevier, Amsterdam, 2006. [cited at p. 36]

[93] P. Kłosowski and A. Mleczek. Parameters' identification of Perzyna and Chaboche viscoplastic models for aluminum alloy at temperature of 120°C. *Engineering Transactions*, 62(3):291–305, 2015. [cited at p. 6]

[94] R. C. Koeller. Applications of fractional calculus to the theory of viscoelasticity. *ASME, Transactions, Journal of Applied Mechanics*, 51:299–307, 1984. [cited at p. 7]

[95] J. Korelc and P. Wriggers. *The finite element method for solid and structural mechanics*. Springer International Publishing, 2016. [cited at p. 28]

[96] P. Kowalczyk and M. Kleiber. *Wprowadzenie do nieliniowej termomechaniki ciał odkształcalnych*. IPPT PAN, first edition, 2011. [cited at p. 13, 28]

[97] E. Kuhl, E. Ramm, and R. de Borst. An anisotropic gradient damage model for quasi-brittle materials. *Computer Methods in Applied Mechanics and Engineering*, 183(1–2):87–103, 2000. [cited at p. 4]

[98] V. V. Kulish and J. L. Lage. Application of fractional calculus to fluid mechanics. *Journal of Fluids Engineering*, 124(3):803–806, 2002. [cited at p. 7]

[99] D. C. C. Lam, F. Yang, A. C. M. Chong, J. Wang, and P. Tong. Experiments and theory in strain gradient elasticity. *Journal of the Mechanics and Physics of Solids*, 51(8):1477–1508, 2003. [cited at p. 4]

[100] T. Leffers. Lattice rotations during plastic deformation with grain subdivision. *Materials Science Forum*, 157–162:1815–1820, 1994. [cited at p. 3, 42]

[101] X. Lei and C. J. Lissenden. Pressure sensitive nonassociative plasticity model for DRA composites. *Journal of Engineering Materials and Technology ASME*, 129(2):255–264, 2007. [cited at p. 3]

[102] J. Lemonds and A. Needleman. Finite element analyses of shear localization in rate and temperature dependent solids. *Mechanics of Materials*, 5(4):339–361, 1986. [cited at p. 5]

[103] J. S. Leszczyński. Using the fractional interaction law to model the impact dynamics of multiparticle collisions in arbitrary form. *Physical Review E*, 70(5):051315, 2004. [cited at p. 7]

[104] J. S. Leszczyński. *An introduction to fractional mechanics*. Monographs No 198. The Publishing Office of Czestochowa University of Technology, 2011. [cited at p. 7, 35]

[105] J. S. Leszczyński and T. Błaszczyk. Modeling the transition between stable and unstable operation while emptying a silo. *Granular Matter*, 13(4):429–438, 2011. [cited at p. 7]

[106] C. Liebold and W. H. Müller. *Measuring material coefficients of higher gradient elasticity by using AFM techniques and Raman-spectroscopy*, volume 22, pages 255–271. Springer, 2013. [cited at p. 4]

[107] H. Ling, D. Yue, V. Kaliakin, and N. Themelis. Anisotropic elastoplastic bounding surface model for cohesive soils. *Journal of Engineering Mechanics ASCE*, 128(7):748–758, 2002. [cited at p. 3]

[108] J. Litoński. Plastic flow of a tube under adiabatic torsion. *Academie Polonaise des Sciences, Bulletin, Serie des Sciences Techniques*, 25(1):1, 1977. [cited at p. 5]

[109] T. Łodygowski and W. Sumelka. *Anisotropic damage for extreme dynamics*. Springer-Verlag, New York, 2015. [cited at p. 7]

[110] V. A. Lubarda, S. Mastilovic, and J. Knap. Some comments on plasticity postulates and non-associative flow rules. *International Journal of Mechanical Sciences*, 38(3):247–258, 1996. [cited at p. 3]

[111] J. Lubliner. *Plasticity Theory*. Macmillan Publishing, New York, 1990. [cited at p. 38]

[112] R. L. Magin. *Fractional Calculus in Bioengineering*. Begell House Inc., Redding, 2006. [cited at p. 7]

[113] R. L. Magin and M. Ovadia. Modeling the cardiac tissue electrode interface using fractional calculus. *Journal of Vibration and Control*, 14(9–10):1431–1442, 2008. [cited at p. 7]

[114] G. Maier and T. Hueckel. Nonassociated and coupled flow rules of elastoplasticity for rock-like materials. *International Journal of Rock Mechanics and Mining Sciences & Geomechanics Abstracts*, 16(2):77–92, 1979. [cited at p. 3]

[115] F. Mainardi. *Fractional calculus and waves in linear viscoelasticity: An introduction to mathematical models*. World Scientific, 2010. [cited at p. 7]

[116] F. Mainardi, M. Raberto, R. Gorenflo, and E. Scalas. Fractional calculus and continuous-time finance II: The waiting-time distribution. *Physica A: Statistical Mechanics and its Applications*, 287(3–4):468–481, 2000. [cited at p. 7]

[117] A. B. Malinowska, T. Odzijewicz, and D. F. M. Torres. *Advanced Methods in the Fractional Calculus of Variations*. Springer Briefs in Applied Sciences and Technology. Springer, 2015. [cited at p. 36]

[118] M. T. Manzari and K. Yonten. On implementation and performance of an anisotropic constitutive model for clays. *International Journal of Computational Methods*, 11(2):1342009, 2014. [cited at p. 3]

[119] A. Marchand and J. Duffy. An experimental study of the formation process of adiabatic shear bands in a structural steel. *Journal of the Mechanics and Physics of Solids*, 36(3):251–283, 1988. [cited at p. 5]

[120] T. Margulies. Wave propagation in viscoelastic horns using a fractional calculus rheology model. *The Journal of the Acoustical Society of America*, 114(4):2442–2442, 2003. [cited at p. 7]

[121] E. B. Marin and D. L. McDowell. Models for compressible elasto-plasticity based on internal state variables. *International Journal of Damage Mechanics*, 7(1):47–83, 1998. [cited at p. 42]

[122] B. Mathieu, P. Melchior, A. Oustaloup, and C. Ceyral. Fractional differentiation for edge detection. *Signal Processing*, 83(11):2421–2432, 2003. [cited at p. 7]

[123] G. A. Maugin. Nonlocal theories or gradient-type theories – a matter of convenience? *Archives of Mechanics*, 31(1):15–26, 1979. [cited at p. 4]

[124] D. L. McDowell. Viscoplasticity of heterogeneous metallic materials. *Materials Science and Engineering R*, 62:67–123, 2008. [cited at p. 3, 42]

[125] M. A. Meyers, Y. B. Xu, Q. Xue, M. T. Perez-Prado, and T. R. McNelley. Microstructural evolution in adiabatic shear localization in stainless steel. *Acta Materialia*, 51(5):1307–1325, 2003. [cited at p. 6]

[126] R. L. Michałowski and A. Zhao. Continnum versus structural approach to stability of reinforced soils. *Journal of Geotechnical Engineering*, 121(2):152–162, 1995. [cited at p. 3]

[127] R. D. Mindlin. Second gradient of strain and surface-tension in linear elasticity. *International Journal of Solids and Structures*, 1(4):417–438, 1965. [cited at p. 4]

[128] R. D. Mindlin and N. Eshel. On first strain-gradient theories in linear elasticity. *International Journal of Solids and Structures*, 4(1):109–124, 1968. [cited at p. 4]

[129] R. v. Mises. Mechanik der festen Körper im plastisch-deformablen Zustand. *Nachrichten von der Gesellschaft der Wissenschaften zu Göttingen, Mathematisch-Physikalische Klasse*, 1913:582–592, 1913. [cited at p. 39]

[130] A. Molinari and R. J. Clifton. Localisation de la deformation viscoplastique en cisaillement simple, resultats exacts en theorie non-lineaire. *Comptes Rendus Academie des Sciences, II*, 296:1–4, 1983. [cited at p. 6]

[131] A. Molinari and R. J. Clifton. Analytical characterization of shear localization in thermoviscoplastic materials. *Journal of Applied Mechanics*, 54(4):806–812, 1987. [cited at p. 6]

[132] G. L. Moss. Shear strains, strain rates and temperature changes in adiabatic shear bands. In *Shock Waves and High-Strain-Rate Phenomena in Metals*, pages 299–312. Springer, 1981. [cited at p. 5]

[133] Z. Mróz. Non-associated flow laws in plasticity. *Journal de Mécanique*, 2(1):21–42, 1963. [cited at p. 3]

[134] P. M. Naghdi and S. A. Murch. On the Mechanical Behavior of Viscoelastic/Plastic Solids. *Journal of Applied Mechanics*, 30:321, 1963. [cited at p. 40]

[135] J. A. Nemes and J. Eftis. Constitutive modelling of the dynamic fracture of smooth tensile bars. *International Journal of Plasticity*, 9(2):243–270, 1993. [cited at p. 60]

[136] N. M. Newmark. A method of computation for structural dynamics. In *Journal of the Engineering Mechanics Division*. American Society of Civil Engineers, 1959. [cited at p. 33]

[137] W. Nowacki. *Theory of micropolar elasticity*. Number 25 in International Centre for Mechanical Sciences. Springer, 1972. [cited at p. 4]

[138] Z. Odibat. Approximations of fractional integrals and Caputo fractional derivatives. *Applied Mathematics and Computation*, 178:527–533, 2006. [cited at p. 37]

[139] T. Odzijewicz, A. B. Malinowska, and D. F. M. Torres. Green's theorem for generalized fractional derivatives. *Fractional Calculus and Applied Analysis*, 16(1):64–75, 2013. [cited at p. 35]

[140] K. Oldham and J. Spanier. *The Fractional Calculus*. Academic Press, New York, 1974. [cited at p. 7]

[141] G. B. Olson, J. F. Mescall, and M. Azrin. Adiabatic deformation and strain localization. In *Shock waves and high-strain-rate phenomena in metals*, pages 221–247. Springer, 1981. [cited at p. 5]

[142] Orange County Register. Orange county register; photo of a car that crashed into a post office building, 2015. [online; accessed September 30, 2019]. [cited at p. 3]

[143] J. Ostrowska-Maciejewska. *Mechanika ciał odkształcalnych*. PWN, Warszawa, 1994. [cited at p. 13]

[144] J. Pan, M. Saje, and A. Needleman. Localization of deformation in rate-sensitive porous plastic solids. *International Journal of Fracture*, 21(4):261–278, 1983. [cited at p. 5]

[145] D. Peirce. Shear band bifurcations in ductile single crystals. *Journal of the Mechanics and Physics of Solids*, 31(2):133–153, 1983. [cited at p. 5]

[146] Q. Peng and M. X. Chen. An efficient return mapping algorithm for general isotropic elastoplasticity in principal space. *Computers & Structures*, 92:173–184, 2012. [cited at p. 4]

[147] L. F. Pereira, J. Weerheijm, and L. J. Sluys. A new rate-dependent stress-based nonlocal damage model to simulate dynamic tensile failure of quasi-brittle materials. *International Journal of Impact Engineering*, 94:83–95, 2016. [cited at p. 4]

[148] P. Perzyna. The constitutive equations for rate sensitive plastic materials. *Quarterly of Applied Mathematics*, 20:321–332, 1963. [cited at p. 6, 38, 39, 40]

[149] P. Perzyna. Fundamental problems in viscoplasticity. *Advances in Applied Mechanics*, **9**:243–377, 1966. [cited at p. 38, 39]

[150] P. Perzyna. Thermodynamic theory of viscoplasticity. *Advances in Applied Mechanics*, 11:313–354, 1971. [cited at p. 38]

[151] P. Perzyna. Constitutive modeling of dissipative solids for postcritical behavior and fracture. *Journal of Engineering Materials and Technology*, 106(4):410–419, 1984. [cited at p. 61]

[152] P. Perzyna. Constitutive modelling for brittle dynamic fracture in dissipative solids. *Archives of Mechanics*, 38:725–738, 1986. [cited at p. 60]

[153] P. Perzyna. Internal state variable description of dynamic fracture of ductile solids. *International Journal of Solids and Structures*, 22:797–818, 1986. [cited at p. 60]

[154] P. Perzyna. The thermodynamical theory of elasto-viscoplasticity. *Engineering Transactions*, 53:235–316, 2005. [cited at p. 6, 83]

[155] P. Perzyna. The thermodynamical theory of elasto-viscoplasticity accounting for microshear banding and induced anisotropy effects. *Mechanics*, 27(1):25–42, 2008. [cited at p. 4, 6, 38, 73]

[156] P. Perzyna. The thermodynamical theory of elasto-viscoplasticity for description of nanocrystalline metals. *Engineering Transactions*, 58(1-2):15–74, 2010. [cited at p. 60]

[157] P. Perzyna. Micromechanics of localized fracture phenomena in inelastic solids generated by impact-loaded adiabatic processes. *Engineering Transactions*, 59(4), 2011. [cited at p. 40, 60]

[158] P. Perzyna. Multiscale constitutive modelling of the influence of anisotropy effects on fracture phenomena in inelastic solids. *Engineering Transactions*, 60(3):225–284, 2011. [cited at p. 40]

[159] P. Perzyna and W. Dornowski. Constitutive modeling of inelastic solids for plastic flow processes under cyclic dynamic loadings. *Journal of Engineering Materials and Technology*, 121(12), 1999. [cited at p. 60]

[160] I. Podlubny. *Fractional Differential Equations*, volume 198 of *Mathematics in Science and Engineering*. Academic Press, 1999. [cited at p. 7, 35, 37]

[161] V. Racherla and J. L. Bassani. Strain burst phenomena in the necking of a sheet that deforms by non-associated plastic flow. *Modelling and Simulation in Materials Science and Engineering*, 15(1):S297–S311, 2007. [cited at p. 3, 42]

[162] E. Radi and D. Bigoni. Asymptotic fields of mode I steady-state crack propagation in non-associative elastoplastic solids. *Mechanics of Materials*, 14(3):239–251, 1993. [cited at p. 3]

[163] P. E. Reyes-Morel and I. W. Chen. Transformation plasticity of CeO_2-stabilized tetragonal zirconia polycrystals: I stress assistance and autocatalysis. *Journal of the American Ceramic Society*, 71(5):343–353, 1988. [cited at p. 3]

[164] J. R. Rice. Localization of plastic deformation. Technical report, Brown University, Providence, RI (USA). Division of Engineering, 1976. [cited at p. 5]

[165] J. M. Ricles, D. G. Lignos, and J. Love. Performance of engineered structures in the Mw 9.0 Tohoku, Japan, Earthquake of March 11, 2011. Technical Report EERI Special Earthquake Report, Earthquake Engineering Research Institute, January 2012. [cited at p. 2]

[166] H. C. Rogers. *Adiabatic Shearing – A Review.* Drexel University Report, 1974. [cited at p. 5]

[167] H. C. Rogers. Adiabatic plastic deformation. *Annual Review of Materials Science*, 9(1):283–311, 1979. [cited at p. 5]

[168] H. C. Rogers. *Adiabatic Shearing – General Nature and Material Aspects*, pages 101–118. Springer US, Boston, MA, 1983. [cited at p. 5]

[169] H. C. Rogers and C. V. Shastry. Shock waves and high-strain-rate phenomena in metals. *Archive of Applied Mechanics*, 50, 1981. [cited at p. 5]

[170] J. W. Rudnicki and J. R. Rice. Conditions for the localization of deformation in pressure-sensitive dilatant materials. *Journal of the Mechanics and Physics of Solids*, 23(6):371–394, 1975. [cited at p. 5]

[171] A. Rusinek, R. Zaera, and J. R. Klepaczko. Constitutive relations in 3-D for a wide range of strain rates and temperatures : Application to mild steels. *International Journal of Solids and Structures*, 44(17):5611–5634, 2007. [cited at p. 63]

[172] M. Safaei, M.-G. Lee, S.-L. Zang, and W. De Waele. An evolutionary anisotropic model for sheet metals based on non-associated flow rule approach. *Computational Materials Science*, 81:15–29, 2014. [cited at p. 4]

[173] M. Safaei, S.-L. Zang, M.-G. Lee, and W. De Waele. Evaluation of anisotropic constitutive models: Mixed anisotropic hardening and non-associated flow rule approach. *International Journal of Mechanical Sciences*, 73:53–68, 2013. [cited at p. 4]

[174] E. Scalas, R. Gorenflo, and F. Mainardi. Fractional calculus and continuous-time finance. *Physica A: Statistical Mechanics and its Applications*, 284(1–4):376–384, 2000. [cited at p. 7]

[175] T. G. Shawki and R. J. Clifton. Shear band formation in thermal viscoplastic materials. *Mechanics of Materials*, 8(1):13–43, 1989. [cited at p. 6]

[176] S. Shima and M. Oyane. Plasticity for porous solids. *International Journal of Mechanical Sciences*, 18:285–291, 1976. [cited at p. 61]

[177] J. C. Simo and T. J. R. Hughes. *Computational inelasticity.* Interdisciplinary Applied Mathematics. Springer, 1997. [cited at p. 7, 45]

[178] V. P. Smyshlyaev and N. A. Fleck. The role of strain gradients in the grain size effect for polycrystals. *Journal of the Mechanics and Physics of Solids*, 44(4):465–495, 1996. [cited at p. 4]

[179] A. J. M. Spencer. *Continuum Mechanics.* Dover books on physics. Dover Publications, 2004. [cited at p. 14]

[180] M. R. Staker. The relation between adiabatic shear instability strain and material properties. *Acta Metallurgica*, 29(4):683–689, 1981. [cited at p. 5]

[181] P. Steinmann, E. Kuhl, and E. Stein. Aspects of non-associated single crystal plasticity: Influence of non-schmid effects and localization analysis. *International Journal of Solids and Structures*, 35(33):4437–4456, 1998. [cited at p. 3, 42]

[182] H. Stumpf and J. Saczuk. On a general concept for the analysis of crack growth and material damage. *International Journal of Plasticity*, 17(7):991–1028, 2001. [cited at p. 4]

[183] J. I. Suárez, B. M. Vinagre, A. J. Calderón, C. A. Monje, and Y. Q. Chen. Using fractional calculus for lateral and longitudinal control of autonomous vehicles. In *International Conference on Computer Aided Systems Theory*, pages 337–348. Springer, 2003. [cited at p. 7]

[184] W. Sumelka. *The Constitutive Model of the Anisotropy Evolution for Metals with Microstructural Defects*. Publishing House of Poznan University of Technology, Poznań, 2009. [cited at p. 6, 48]

[185] W. Sumelka. Role of covariance in continuum damage mechanics. *ASCE Journal of Engineering Mechanics*, 139(11):1610–1620, 2013. [cited at p. 7]

[186] W. Sumelka. Fractional viscoplasticity. *Mechanics Research Communications*, 56:31–36, 2014. [cited at p. 7, 40, 41]

[187] W. Sumelka. Thermoelasticity in the framework of the fractional continuum mechanics. *Journal of Thermal Stresses*, 37(6):678–706, 2014. [cited at p. 7]

[188] W. Sumelka and T. Błaszczyk. Fractional continua for linear elasticity. *Archives of Mechanics*, 66(3):147–172, 2014. [cited at p. 7]

[189] W. Sumelka, T. Błaszczyk, and C. Liebold. Fractional Euler-Bernoulli beams: Theory, numerical study and experimental validation. *European Journal of Mechanics-A/Solids*, 54:243–251, 2015. [cited at p. 7]

[190] W. Sumelka and M. Nowak. Non-normality and induced plastic anisotropy under fractional plastic flow rule: A numerical study. *International Journal for Numerical and Analytical Methods in Geomechanics*, 40:651–675, 2016. [cited at p. 7, 42, 48]

[191] W. Sumelka and M. Nowak. On a general numerical scheme for the fractional plastic flow rule. *Mechanics of Materials*, DOI: 10.1016/j.mechmat.2017.02.005, 2017. [cited at p. 8, 9, 37, 43, 45]

[192] W. Sumelka, R. Zaera, and J. Fernández-Sáez. One-dimensional dispersion phenomena in terms of fractional media. *The European Physical Journal – Plus*, 131:320, 2016. [cited at p. 41]

[193] W. Sumelka and T. Łodygowski. The influence of the initial microdamage anisotropy on macrodamage mode during extremely fast thermomechanical processes. *Archive of Applied Mechanics*, 81(12):1973–1992, 2011. [cited at p. 63]

[194] W. Sumelka and T. Łodygowski. Reduction of the number of material parameters by ANN approximation. *Computational Mechanics*, 52:287–300, 2013. [cited at p. 4]

[195] W. Sumelka and T. Łodygowski. Implicit nonlocality in the framework of the viscoplasticity. In G. Z. Voyiadjis, editor, *Handbook of Nonlocal Continuum Mechanics for Materials and Structures*. Springer International Publishing, 2017. [cited at p. 6, 7]

[196] Y. Sun, Y. Gao, and Q. Zhu. Fractional order plasticity modelling of state-dependent behaviour of granular soils without using plastic potential. *International Journal of Plasticity*, 102:53–69, 2018. [cited at p. 8]

[197] Y. Sun and Y. Shen. Constitutive model of granular soils using fractional-order plastic-flow rule. *International Journal of Geomechanics*, 17(8), 2017. [cited at p. 8]

[198] Y. Sun and Y. Xiao. Fractional order plasticity model for granular soils subjected to monotonic triaxial compression. *International Journal of Solids and Structures*, 118:224–234, 2017. [cited at p. 8]

[199] W. Szczepiński. *Limit States and Kinematics of Granular Media*. Państwowe Wydawnictwo Naukowe, Warszawa, Poland, 1974. [cited at p. 3]

[200] M. Szymczyk, M. Nowak, and W. Sumelka. Numerical study of dynamic properties of fractional viscoplasticity model. *Symmetry*, 10(7), 2018. [cited at p. 7, 9, 41, 42, 47, 48, 49, 50, 51, 52, 53, 54, 55, 56, 57, 89]

[201] M. Szymczyk, M. Nowak, and W. Sumelka. Plastic strain localization in an extreme dynamic tension test of steel sheet in the framework of fractional viscoplasticity. *Thin-Walled Structures*, 2019. [cited at p. 66, 69, 70, 71, 72, 74, 80, 81, 82, 83]

[202] A. Taherizadeh, D. E. Green, and J. W. Yoon. Evaluation of advanced anisotropic models with mixed hardening for general associated and non-associated flow metal plasticity. *International Journal of Plasticity*, 27(11):1781–1802, 2011. [cited at p. 3, 4]

[203] J. Tejchman. *Confined Granular Flow in Silos. Experimental and Numerical Investigations*. Springer, 2013. [cited at p. 3]

[204] J. Tejchman and J. Bobiński. *Continuous and discontinuous modelling of fracture in concrete using FEM*. Springer Science & Business Media, 2012. [cited at p. 4]

[205] T. Y. Thomas. *Plastic Flow and Fracture in Solids*, volume 2. Elsevier, 1961. [cited at p. 5]

[206] R. A. Toupin. Elastic materials with couple-stresses. *Archive for Rational Mechanics and Analysis*, 11(5):385–414, 1963. [cited at p. 4]

[207] M. H. Tresca. On further applications of the flow of solids. *Proceedings of the Institution of Mechanical Engineers*, 29(1):301–345, 1878. [cited at p. 4]

[208] C. Truesdell. *Rational thermodynamics*. Springer-Verlag, 1984. [cited at p. 27]

[209] C. Truesdell and W. Noll. *The non-linear field theories of mechanics*. In: Handbuch der Physik, volume III/3. Springer-Verlag, Berlin, S. Flügge Ed, 1965. [cited at p. 13, 27]

[210] C. Truesdell and R. Toupin. *The Classical Field Theories*, volume 2. Springer Berlin Heidelberg, 1960. [cited at p. 27]

[211] K. C. Valanis and J. F. Peters. Ill-posedness of the initial and boundary value problems in non-associative plasticity. *Acta Mechanica*, 114:1–25, 1996. [cited at p. 4]

[212] P. A. Vermeer and R. de Borst. Non-associated plasticity for soils, concrete and rock. *Heron*, 29(3):163–196, 1984. [cited at p. 3]

[213] Y.-J. Wang, J. H. Yin, and C. F. Lee. The influence of a non-associated flow rule on the calculation of the factor of safety of soil slopes. *International Journal for Numerical and Analytical Methods in Geomechanics*, 25(13):1351–1359, 2001. [cited at p. 3]

[214] A. J. Whittle. Evaluation of a constitutive model for overconsolidated clays. *Géotechnique*, 43(2):289–313, 1993. [cited at p. 3]

[215] T. W. Wright and J. W. Walter. On stress collapse in adiabatic shear bands. *Journal of the Mechanics and Physics of Solids*, 35(6):701–720, 1987. [cited at p. 6]

[216] T. W. Wright and T. W. Wright. *The physics and mathematics of adiabatic shear bands*. Cambridge University Press, 2002. [cited at p. 6]

[217] F. H. Wu and L. B. Freund. Deformation trapping due to thermoplastic instability in one-dimensional wave propagation. *Journal of the Mechanics and Physics of Solids*, 32(2):119–132, 1984. [cited at p. 5]

[218] F. H. Wu, M. Toulios, and L. B. Freund. Initiation and propagation of shear band in antiplane shear deformation. In *Proceedings of the Considere Memorial Symposium*, pages 125–134, 1985. [cited at p. 5]

[219] F. Yang, A. C. M. Chong, D. C. C. Lam, and P. Tong. Couple stress based strain gradient theory for elasticity. *International Journal of Solids and Structures*, 39(10):2731–2743, 2002. [cited at p. 4]

[220] G. M. Zaslavsky and G. M. Zaslavskij. *Hamiltonian chaos and fractional dynamics*. Oxford University Press on Demand, 2005. [cited at p. 7]

[221] C. Zener and J. H. Hollomon. Effect of Strain Rate Upon Plastic Flow of Steel. *Journal of Applied Physics*, 15:22–32, January 1944. [cited at p. 5]

[222] H. Ziegler. *An introduction to thermomechanics*. North Holland Series in Applied Mathematics and Mechanics. North Holland, 1983. [cited at p. 3, 42]

[223] O. C. Zienkiewicz and R. L. Taylor. *The finite element method for solid and structural mechanics*. Elsevier, 2005. [cited at p. 28, 29, 31]

[224] O. C. Zienkiewicz, R. L. Taylor, and J. Z. Zhu. *The finite element method: Its basis and fundamentals*. Elsevier, 2005. [cited at p. 30, 32]

[225] A. K. Zurek and M. A. Meyers. *Microstructural Aspects of Dynamic Failure*, pages 25–70. Springer New York, New York, NY, 1996. [cited at p. 5]

[226] T. Łodygowski. *Theoretical and numerical aspects of plastic strain localization*, volume 312 of *D. Sc. Thesis*. Publishing House of Poznan University of Technology, 1996. [cited at p. 6]

[227] T. Łodygowski, P. Perzyna, M. Lengnick, and Stein E. Viscoplastic numerical analysis of dynamic plastic shear localization for a ductile material. *Archives of Mechanics*, 46(4):541–557, 1994. [cited at p. 6]